

# Strategies for optimizing dynamic MRI



Dissertation zur Erlangung des  
naturwissenschaftlichen Doktorgrades  
der Julius-Maximilians-Universität Würzburg

vorgelegt von  
Irene Paola Ponce Garcia  
aus Mexiko Stadt

Würzburg, 2018

---

Eingereicht am: 29.04.2014

Bei der Fakultät für Physik und Astronomie

1. Gutachter: Prof. Dr. Peter M. Jakob
  2. Gutachter: Prof. Dr. Randolph Hanke
  3. Gutachter: Prof. Dr. Björn Trauzettel
- der Dissertation

Vorsitzende(r): Prof. Dr. Jens Pflaum

1. Prüfer: Prof. Dr. Peter M. Jakob
  2. Prüfer: Prof. Dr. Randolph Hanke
  3. Prüfer: Prof. Dr. Björn Trauzettel
- im Promotionskolloquium

Tag des Promotionskolloquiums: 05.03.2018

Doktorurkunde ausgehändigt am:

# Contents

<b>1. Introduction</b>	<b>5</b>
1.1. Motivation . . . . .	5
1.2. Goal of the Work . . . . .	6
<b>2. MR Basics</b>	<b>8</b>
2.1. Magnetic Properties of Protons . . . . .	8
2.2. Decay and Recovery . . . . .	10
2.3. Spatial Encoding and Imaging . . . . .	11
2.3.1. MRI Signal and k-space . . . . .	12
2.3.2. Slice Selection . . . . .	13
2.4. Discrete Sampling of k-space . . . . .	14
2.5. k-space Coverage . . . . .	16
2.5.1. Cartesian Sampling . . . . .	16
2.5.2. Radial Sampling . . . . .	17
2.6. Acquisition Time and Signal to Noise Ratio . . . . .	18
<b>3. Basics of Parallel Imaging</b>	<b>21</b>
3.1. Historical Overview . . . . .	21
3.2. Basic Concepts . . . . .	22
3.2.1. Aliasing . . . . .	22
3.3. Reconstruction Methods . . . . .	24
3.3.1. Sensitivity Encoding (SENSE) . . . . .	24
3.3.2. Simultaneous Acquisition of Spatial Harmonics (SMASH) . . . . .	26
3.3.3. AUTO-SMASH and VD-AUTO-SMASH . . . . .	28
3.3.4. Generalized Auto-calibrating Partially Parallel Imaging (GRAPPA) . . . . .	30
3.4. Limitations . . . . .	33
3.5. Regularization . . . . .	33
3.6. Summary . . . . .	35
<b>4. Basics of Dynamic Parallel Imaging</b>	<b>36</b>
4.1. Sampling Patterns for Dynamic Imaging . . . . .	37
4.2. Temporal SENSE (TSENSE) . . . . .	38
4.3. Temporal GRAPPA (TGRAPPA) . . . . .	41
4.4. kt-SENSE . . . . .	42
4.5. Summary . . . . .	44
<b>5. Temporal Filtering Effects in Dynamic Parallel MRI</b>	<b>45</b>
5.1. Theory . . . . .	46
5.1.1. Temporal Filtering Effect . . . . .	46
5.1.2. Reducing Temporal Filtering Effect . . . . .	47
5.1.3. kt-SENSE for non-Cartesian Data . . . . .	49
5.2. Methods . . . . .	50
5.2.1. Simulations . . . . .	50
5.2.2. In-vivo Measurements . . . . .	51
5.3. Results . . . . .	52
5.3.1. Simulations . . . . .	52

5.3.2. In-vivo Measurements . . . . .	53
5.3.2.1. Full Resolution Cartesian In-vivo data . . . . .	53
5.3.2.2. Effect of Spatial Filter . . . . .	54
5.3.2.3. Radial In-vivo data . . . . .	56
5.4. Discussion and Conclusion . . . . .	58
<b>6. Auto-calibrating kt-SENSE</b>	<b>61</b>
6.1. Theory . . . . .	62
6.1.1. Auto-calibrating kt-SENSE . . . . .	62
6.2. Methods . . . . .	63
6.2.1. Evaluation: Modulation Transfer Function (MTF) and Noise Amplification . . . . .	63
6.2.2. Simulations . . . . .	65
6.2.3. In-vivo Measurements . . . . .	66
6.3. Results . . . . .	66
6.3.1. Simulations . . . . .	66
6.3.2. In-vivo Measurements . . . . .	69
6.4. Discussion and Conclusions . . . . .	73
<b>7. Optimizing MR Relaxometry using kt-PCA</b>	<b>75</b>
7.1. Theory . . . . .	76
7.1.1. MR Relaxometry . . . . .	76
7.1.1.1. Segmented IR-Snapshot FLASH . . . . .	76
7.1.1.2. Segmented IR TrueFISP . . . . .	78
7.1.2. Data Reconstruction with kt-PCA . . . . .	79
7.2. Methods . . . . .	81
7.2.1. Simulations . . . . .	82
7.2.2. In-vivo Measurements . . . . .	84
7.3. Results . . . . .	85
7.3.1. Simulations . . . . .	85
7.3.2. In-vivo Experiments . . . . .	90
7.4. Discussion and Conclusions . . . . .	95
<b>8. Summary and Outlook</b>	<b>97</b>
<b>A. Principal Component Analysis (PCA)</b>	<b>101</b>
A.0.1. PCA using Singular Value Decomposition (SVD) . . . . .	103
<b>Bibliography</b>	<b>104</b>
<b>List of Publications</b>	<b>112</b>
<b>Acknowledgment</b>	<b>115</b>
<b>Abstract</b>	<b>118</b>
<b>Zusammenfassung</b>	<b>120</b>



# Introduction

## 1.1. Motivation

Medical imaging has been a useful tool of growing importance over the last decades. Advances in software and hardware together with the exploration of different physical principles has led to the development of a variety of imaging methods. Important examples are: Computer Tomography (CT), Positron Emission Tomography (PET) and Single Photon Emission Computed Tomography (SPECT) which involve ionizing radiation; Ultrasound Imaging, which is based on the mechanical properties of sound waves and Magnetic Resonance Imaging (MRI), this technology uses magnetization of the protons in the human body within an external magnetic field. Thanks to the lack of ionizing radiation, MRI and Ultrasound are considered very safe [1] and have become popular in clinical practice [1].

Although MRI provides an excellent soft-tissue contrast in comparison to CT, one of the major drawbacks of MRI is the long acquisition times needed. In addition to patient discomfort, especially if the patient has any impediment to stay immobile or is claustrophobic to any degree, it leads to a low cost-effectiveness of MRI devices. Furthermore, long MRI acquisition times may cause artifacts related to involuntary patient's motion. Respiration, cardiac motion, blood flow, eye movements and swallowing are some examples of involuntary physiological motion. If the object to be measured is in constant motion during the acquisition time, inconsistencies in the phase and amplitude of the signal will occur. As consequence, images may exhibit ghosting artifacts as well as spatial and/or temporal blurring. Many strategies have been proposed in order to reduce these artifacts. Artifacts can be minimized by applying breath holding techniques [2], cardiac triggering or retrospective triggering, respiratory gating (prospective or retrospective) [3] or flow compensation techniques, depending on the physiological movement affecting the image [4]. Multiple averages can also reduce periodic physiological motion artifacts (cardiac motion and respiration) while at the same time increasing the signal to noise ratio. The major disadvantage for all strategies mentioned is an increased acquisition time.

The quality of MRI depends on the resolution, contrast, signal to noise ratio (SNR) and a low artifact-level. These parameters are affected by the field homogeneity, the field strength, the receiver and the pulse sequence type. The main goal of a large percentage of MRI research and past and recent technical developments was and still is reduced acquisition time and improved image quality. Among the past developments are stronger magnets, faster software, advanced sequences and imaging reconstruction techniques such as parallel MRI (pMRI). The later one, allows to shorten acquisition times by only partially acquiring the usually required data using arrays of multiple receiver coils. This leads to errors in the imaging called aliasing. pMRI requires the signal to be detected simultaneously and independently by several receiver coils with different spatial sensitivity profiles. This additional spatial information is exploited to calculate missing data points and obtain aliasing-free images. Hence, the gradient encoding in the acquisition process is partially replaced by coil encoding. pMRI experienced its breakthrough in 1997 with the introduction of SMASH [5], which was shown to generate artifact-free in vivo images. In the following years, many different reconstruction techniques such as AUTO-SMASH [6], SENSE [7], SPACE RIP [8], PILS [9], VD-AUTO-SMASH [10] and GRAPPA [11] emerged. Nowadays, pMRI is an integral part of clinical routines.

Further reconstruction and acquisition strategies have been developed to measure dynamic changes of the objects. The difficulty of measuring the signal from dynamic objects increases with the speed of the motion because the temporal window for the acquisition of a single frame decreases. pMRI techniques allow an acceleration of the acquisition by partially measuring the object over the time. Dynamic pMRI reconstruction methods such as UNFOLD [12], TSENSE [13] and TGRAPPA [14] suppress aliasing artifacts at moderate acceleration factors. Recently, kt-BLAST/kt-SENSE [15] and kt-PCA [16] have provided good quality reconstructions for highly accelerated acquisitions. Additional to spatial sensitivity encoding, these reconstruction techniques use spatio-temporal correlation between data. Prior information about these correlations is obtained from a training data set, which consists of low resolution images. The training data set represents extra lines to be acquired and therefore extra scanning time. Additionally, the trade-off between spatial and temporal resolution to be considered in the acquisition of training data may cause undesired spatio-temporal filtering in the reconstructed data.

## 1.2. Goal of the Work

The main aim of dynamic MRI is to not only accurately capture fast movements of the organs (e.g. in cardiac imaging) but also to obtain tissue relaxation variables. Also known as relaxometry, this allows a proper assessment of several diseases and lesions. In this thesis, applications to both cardiac imaging and relaxometry studies are presented.

In this work, we propose several strategies in order to alleviate the trade-off problem for training data to be used in reconstructions of accelerated dynamic MRI acquisitions as described in the last section. One of the goals of this project is to characterize different dynamic parallel imaging approaches and to address possible drawbacks. Funda-

mentally, dynamic MRI techniques are developed which improve spatial and temporal resolution of reconstructed images.

Using methods such as feedback regularization [17], non-Cartesian sampling strategies and efficient reconstruction methods as kt-SENSE and kt-PCA, high-quality images with a high temporal resolution can be obtained without increasing acquisition time.

The outline of this thesis is described as follows: in Chapter 2 the basic concepts of MRI are introduced. Chapter 3 and 4 addresses topics related to parallel imaging and dynamic parallel imaging respectively. In Chapter 5, non-Cartesian strategies for dynamic cardiac images are developed that reduce the temporal filtering showing in the auto-calibration of some dedicated reconstruction methods using accelerated Cartesian data. In Chapter 6, the auto-calibration for kt-SENSE is presented in order to eliminate the need for training data and therefore increasing the efficiency of the acquisition.

The concept of kt-PCA, proposed first for cardiac imaging, is presented in Chapter 7 for reconstructing MR relaxometry studies. Finally a discussion of this work is given in Chapter 8.

# 2

## Chapter 2.

# MR Basics

## 2.1. Magnetic Properties of Protons

Elementary particles have inherent properties such as mass, charge and spin, which is an intrinsic quantum mechanical angular momentum [18]. Magnetic Resonance makes use of the magnetic properties connected with the spins of nuclei to obtain information about their spatial distribution. Due to its abundance in the human body, hydrogen ( $^1H$ ) is the most commonly used nucleus in clinical applications and will therefore be discussed exclusively in this chapter. However, MR Images have also been based on other nuclei such as carbon, phosphorus, sodium and fluorine.

In quantum mechanics the spin is characterized by its quantum numbers ( $s, m_s$ ), which correspond to the magnitude and the orientation of the spin respectively. Its angular momentum ( $S$ ) is given by:

$$S = [s(s+1)]^{\frac{1}{2}} \hbar \quad (2.1.1)$$

where  $\hbar$  is the Planck constant ( $1.054 \times 10^{-34} J \cdot s$ ) over  $2\pi$ . The quantization of the spin direction is given by the second quantum number  $m_s$  (also known as the azimuthal quantum number). In an external magnetic field  $\vec{B} = B_0 \vec{e}_z$ , the energy of a single spin is given by:

$$E = -\vec{\mu} \cdot \vec{B} = -\gamma \vec{S} \cdot \vec{B} \quad (2.1.2)$$

Hereby,  $\vec{\mu}$  is the magnetic moment connected with the spin  $\vec{S}$  and  $\gamma$  the gyromagnetic ratio (for hydrogen  $2.68 \times 10^8$  rad/s/Tesla). This leads to  $2s + 1$  different eigenstates associated with the values of the azimuthal quantum number ( $m_s = -s, -s + 1, \dots, s$ ). The hydrogen nucleus has the spin quantum number  $s = \frac{1}{2}$ . In this case, there are two eigenstates with the eigenvalues ( $m_s = \pm \frac{1}{2}$ ). The state  $m_s = \frac{1}{2}$  (pointing in the positive  $z$ -direction) contains lower energy than  $m_s = -\frac{1}{2}$  (pointing in the negative  $z$ -direction).

In MRI, only the signal from an ensemble of spins is measured rather than the signal coming from individual spins. In thermal equilibrium and in the absence of an external magnetic field, the tips of all spins are isotropically distributed on the surface of a sphere, leading to zero net magnetization. An external magnetic field introduces a



preferred direction with a lower energy level according to equation 2.1.2. Therefore, the spatial distribution of the orientation of all of spins now changes slightly, resulting in a macroscopic magnetization ( $\vec{M}$ ) directed along the external magnetic field as depicted in Figure 2.1.1. In thermal equilibrium, the magnetization vector is static and cannot be measured by MR.

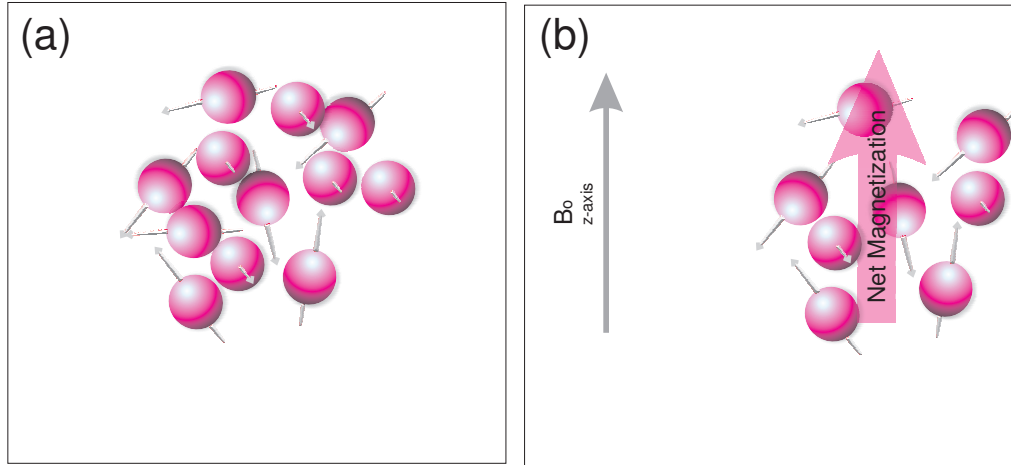


Figure 2.1.1.: The spins in thermal equilibrium lead to no net magnetization (a). However a polarization/magnetization vector appears if the sample is immersed in an external magnetic field  $B_0$  (b).[19]

However if  $\vec{M}$  is tipped away from the  $z$ -axis, the net magnetization vector precesses in the  $xy$ -plane and the MR signal can be acquired through electromagnetic induction using radiofrequency coils. The magnetization vector, as well as the individual spins, precess with an angular frequency given by:

$$\omega_0 = \gamma B_0 \quad (2.1.3)$$

This equation is known as the Larmor equation [20]. The evolution of the net magnetization vector is usually considered in a rotating reference frame (at the Larmor frequency) to significantly simplify description. In this reference frame, the magnetization does not experience the Larmor precession due to  $B_0$ . To rotate the magnetization vector from its equilibrium on the  $z$ -axis into the transversal plane, an extra constant magnetic field  $\vec{B}_1 = B_1 \vec{e}_x$  is applied, located in the transversal plane of the rotating reference frame (Figure 2.1.2). In order to maintain a constant direction in the rotating reference frame,  $B_1$  has to rotate around the  $z$ -axis of the laboratory frame at the Larmor frequency ( $\omega_0 = \gamma B_0$ ). This leads to a precession of the magnetization around  $B_1$  with the frequency  $\omega = \gamma B_1$ . For typical field strengths  $B_0$  used in MR,  $\omega_0$  lies in the range of radio frequencies (*rf*).

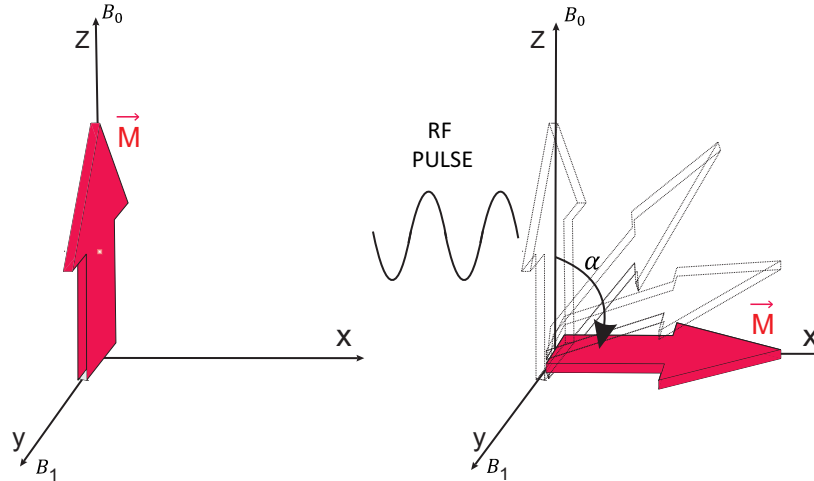


Figure 2.1.2.: During the application of a *rf*-pulse with the  $B_1$  field aligned along the  $y$ -axis in the rotating frame, the magnetization vector  $\vec{M}$  rotates in the  $xz$ -plane.

For *rf* pulses of finite duration with a varying field strength  $B_1(t)$ , the total rotation angle ( $\alpha$ ) of the magnetization vector due to Larmor precession is given by:

$$\alpha = \int_0^{\tau} \omega(t) dt = \gamma \int_0^{\tau} |B_1(t)| dt \quad (2.1.4)$$

The angle  $\alpha$  is often referred to as flip angle. Some important examples are the  $90^\circ$  excitation and the  $180^\circ$  inversion angles.

## 2.2. Decay and Recovery

After excitation, the net magnetization vector ( $\vec{M}$ ) precesses around the external magnetic field and a MR signal can be measured, which decays overtime. Two different relaxation processes dominate the evolution of the magnetization vector back to its thermal equilibrium.

The recovery of longitudinal magnetization is known as spin-lattice relaxation and is caused by the interaction of the spins with the surrounding matter by exchange of energy. The magnetization hereby recovers exponentially with the time constant  $T_1$ .

Additionally, the spins experience a spin-spin interaction due to the local magnetic field caused by the surrounding spins, resulting in spatially slightly varying Larmor frequencies. As a consequence of spin-spin interactions, the magnetization decreases in amplitude along the transverse plane. This exponential temporal decay of the magnetization vector is known as  $T_2$  relaxation. Further dephasing of the magnetization is caused by the inhomogeneity of  $B_0$ . Both effects combined lead to an accelerated exponential decay according to the smaller time constant  $T_2^*$ . The relaxation parameters of each tissue are characteristic and can be exploited to obtain different image contrasts that highlight or suppress signal corresponding to specific tissues.

The temporal evolution of the transversal and longitudinal components of the vector  $\vec{M}$  is mathematically represented by:

$$M_z(t) = M_0(1 - (M_0 - M_z(0)) \cdot e^{-t/T_1}) \quad (2.2.1)$$

$$M_{xy}(t) = M_{xy}(0) \cdot e^{-t/T_2} \quad (2.2.2)$$

As depicted in Figure 2.2.1  $M_{xy}$  decreases to zero along the time axis and  $M_z$  recovers asymptotically from  $M_z(0)$  towards  $M_0$ .

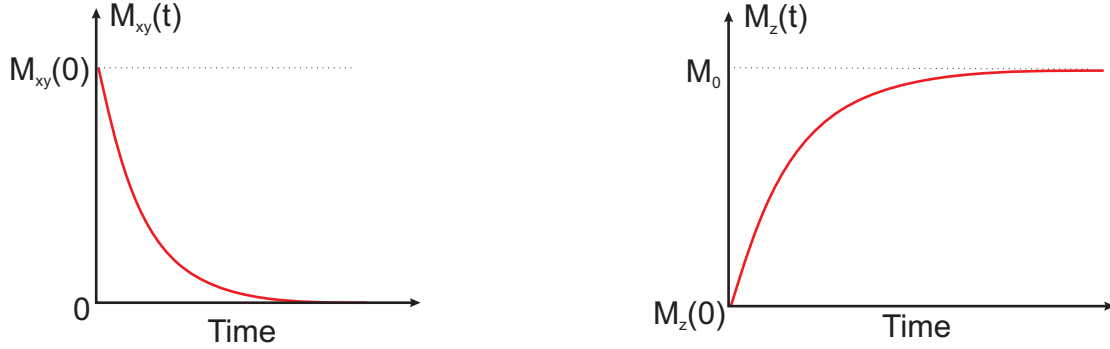


Figure 2.2.1.: Relaxation and recovery graphics of magnetization vector in transversal (on the left) and longitudinal (on the right) axis.

### 2.3. Spatial Encoding and Imaging

After a single excitation, the decaying signal received by  $rf$  coils is coming from all the excited protons in the sample without any information about their location. In MRI, spatial encoding is introduced by magnetic field gradients in three directions across the volume of the sample, as depicted in Figure 2.3.1. The nuclei experience different magnetic fields according to their position  $\vec{r}$  and the corresponding magnetization vectors precess at different Larmor frequencies  $\omega$ :

$$\omega(\vec{r}, t) = \gamma \cdot B(\vec{r}, t) = \gamma(B_0 + \vec{G}(t) \cdot \vec{r}) \quad (2.3.1)$$

where  $\vec{G} = \vec{\nabla} B_z$ . Here the time dependency of the gradient denotes its variation during the sample acquisition process.

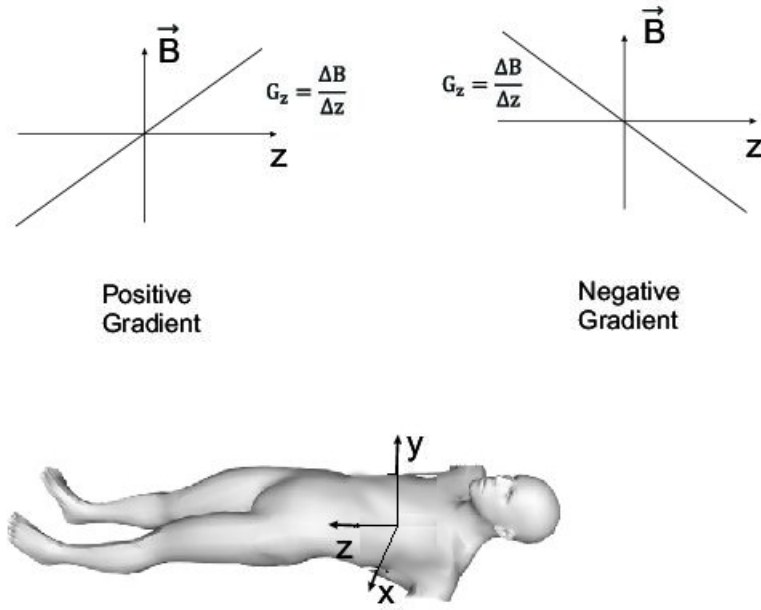


Figure 2.3.1.: Gradients in  $x$ ,  $y$  and  $z$  axis are applied to the sample immersed in the main magnetic field ( $\vec{B}$ ) in order to acquire an image. Here an example of gradients applied in  $z$  direction.

In the following subsections, the encoding in the  $x$  and  $y$  direction for 2-D imaging, also known as frequency and phase encoding respectively, is described in detail. It can be easily extended to 3-D imaging, adding another encoding gradient in the  $z$ -direction. For more details reference [21] is suggested.

### 2.3.1. MRI Signal and k-space

The application of gradients leads to a signal  $S(t)$ , which consists of the superposition of all contributions at different frequencies:

$$S(t) \propto \int \rho(\vec{r}) e^{i \int_0^t \omega(\vec{r}, t') dt'} d^3 r, \quad (2.3.2)$$

where  $\rho(\vec{r})$  is the spin density at the location  $\vec{r}$ . Relaxation effects are omitted for simplification. Inserting equation 2.3.1 results in:

$$S(t) \propto e^{i\omega_0 t} \int \rho(\vec{r}) e^{i \int_0^t \gamma \vec{G}(t') \cdot \vec{r} dt'} d^3 r. \quad (2.3.3)$$

In the rotating frame, the term  $\omega_0$  vanishes. Introducing  $\vec{k} = \gamma \int_0^t \vec{G}(t') dt'$  proportional to the gradient moment, we obtain:

$$S(\vec{k}) \propto \int \rho(\vec{r}) e^{i \vec{k} \cdot \vec{r}} d^3 r \quad (2.3.4)$$

From this equation can be seen that  $S(\vec{k})$  is represented by the Fourier transform of

the spin density. The vector  $\vec{k}$  is element of a typically two- or three- dimensional space depending on the acquisition type, known in MRI as k-space. The image of the object is proportional to its spin density in each location  $\vec{r}$ , can be obtained by applying the inverse Fourier transform of  $S(\vec{k})$ :

$$\rho(\vec{r}) \propto \int S(\vec{k}) e^{-i\vec{k}\cdot\vec{r}} d^3k. \quad (2.3.5)$$

The substitution of  $\vec{k}$  in equation 2.3.4 simplifies the idea of spatial encoding. To be able to perform this inverse operation, data at all points  $\vec{k}$  have to be acquired. In practice, data are taken at discrete locations for  $k = (N_x \Delta k_x, N_y \Delta k_y)$ . Data in one direction are acquired by applying a constant linear magnetic field gradient during acquisition. The gradient in  $x$ -direction is known as the read out gradient. Encoding in the other direction is achieved by applying gradients at varying moments before each read out. This is called phase encoding. Hence, to sample a whole image of size  $N_x \times N_y$ , a total number of  $N_y$  read outs have to be performed.

### 2.3.2. Slice Selection

The first step in a 2-D MRI acquisition is a selective excitation of the desired slice in an arbitrary orientation. To follow conventions in MR, the reference system is chosen so that the slice direction is aligned to the  $z$ -axis. The selection of a slice means the excitation of just the desired volume along the  $z$ -axis, with a thickness of  $\Delta z$ . This can be performed with the help of a gradient in  $z$  direction given by:

$$G_z = \frac{\partial B_z}{\partial z} \quad (2.3.6)$$

Similar to the last subsection, the gradient introduces a spatial dependency of the Larmor frequency of all spins. Now, using a  $rf$  excitation pulse with a well-defined frequency range leads to a selective excitation of only the spins at the corresponding resonance frequencies. This process is depicted in Figure 2.3.2<sup>1</sup>. To achieve a homogeneous excitation across the desired slice, ideally the  $rf$  pulse should exhibit a box-car profile in the frequency domain. This corresponds via Fourier transform to a *sinc* function for the temporal envelope of the  $rf$  pulse. For a limited bandwidth of  $\Delta\nu$ , the slice thickness can be described by:

$$\Delta z = \frac{2\pi}{\gamma G_z \Delta\nu} \quad (2.3.7)$$

The slice is centered at the position  $z_0$  set by the carrier frequency of the  $rf$  pulse.

<sup>1</sup>This graphic was modified from the original Figure 1.3 in Haacke 1999

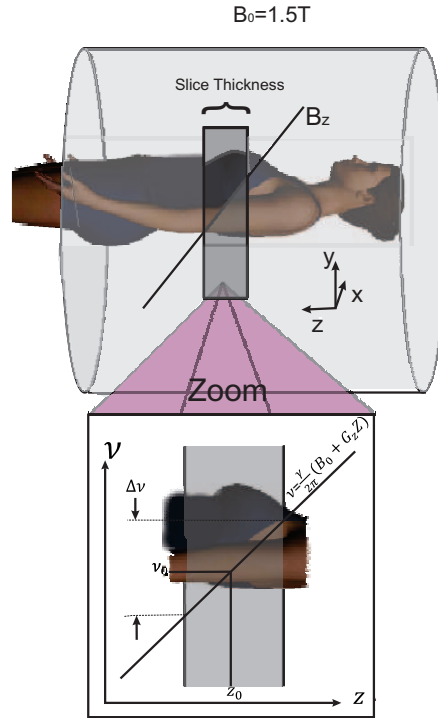


Figure 2.3.2.: The precession frequency  $\nu = \frac{\omega}{2\pi}$  of the spins is a function of their position along the  $z$ -axis. The center frequency of the  $rf$  pulse must be offset from the Larmor frequency by  $\gamma G_z \cdot z_0$ .

## 2.4. Discrete Sampling of k-space

Consider the continuous sampling of a signal  $S(k)$  described by equation 2.3.4. The received signal  $S(k)$  can be discretized by the multiplication of the signal with an infinite train of delta functions in a rectangular window  $w(k)$ , which delimits the number of samples ( $N$ ):

$$d_\infty(k) = \Delta k \sum_{j=-\infty}^{\infty} \delta(k - j\Delta k) \quad (2.4.1)$$

$$s(k) = S(k) \cdot d_\infty(k) \cdot w(k) = \Delta k \sum_{j=-n}^{n-1} S(j\Delta k) \delta(k - j\Delta k) \quad (2.4.2)$$

As expression 2.3.5 suggests, the Fourier transform of the k-space yields the image or spin density of the truth object. In the present discrete case, the Fast Fourier Transform (FFT) is applied leading to:

$$\hat{\rho}(x) = \Delta k \sum_{j=-n}^{n-1} S(j\Delta k) e^{i j \Delta k x} \quad (2.4.3)$$

A multiplication of two functions in k-space represents their convolution in image domain and vice versa. Consider for instance the example shown in Figure 2.4.1. The

discrete sampling of the Gaussian curve (object) is generated by the multiplication of a train of delta functions and the continuous signal. In frequency domain, this represents the convolution of the Fourier transformation of the object with the transform of the windowed train of delta functions, which consists in a periodic *sinc* function. Wider windows produce very narrow *sinc* peaks modeled as delta functions. The periodicity of the density spin function satisfies  $x = x - l \frac{2\pi}{\Delta k}$  for any positive and negative integer  $l$ . The distance between each sample in  $k$ -space is inversely related to the so called Field of View (*FOV*) of the experiment:

$$FOV = \frac{2\pi}{\Delta k} \tag{2.4.4}$$

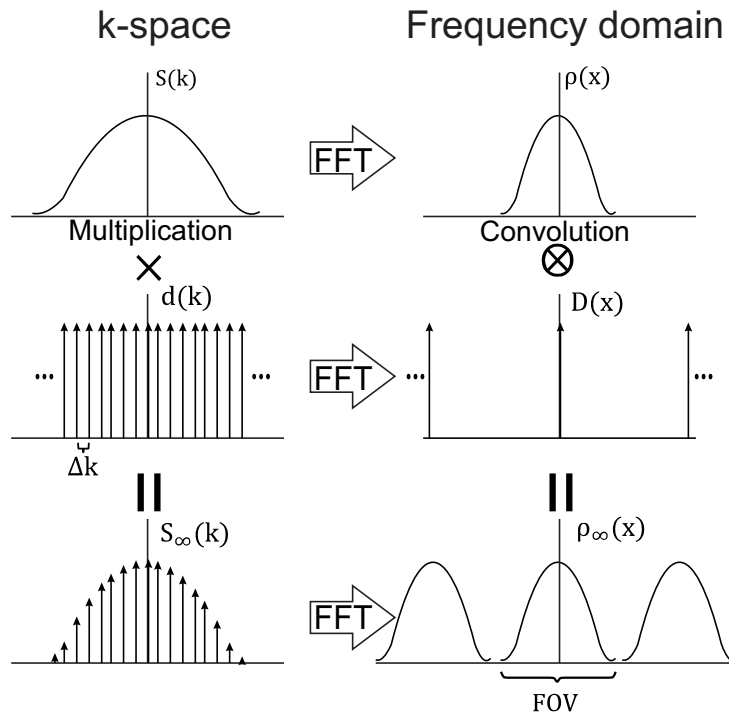


Figure 2.4.1.: Fourier Transform pairs of the sampling process of a Gaussian signal.

If the Nyquist sampling criterion is not satisfied, the adjacent copies overlap, this is also known as aliasing. The Nyquist sampling criterion establishes that the *FOV* should be at least or larger than the size of the object ( $A$ ),  $FOV > A$ , in order to avoid the influence of aliasing.

In the real life, as infinite sampling is not possible, a truncated version of a train of delta functions is applied. To avoid blurring or Gibbs ringing artifacts in the image domain, the temporal window where this train is applied should be wide enough.

Those concepts can be straight forward extended to the  $n$ -dimensional data  $s(\vec{k})$  (see Figure 2.4.2 for the 2-D case).

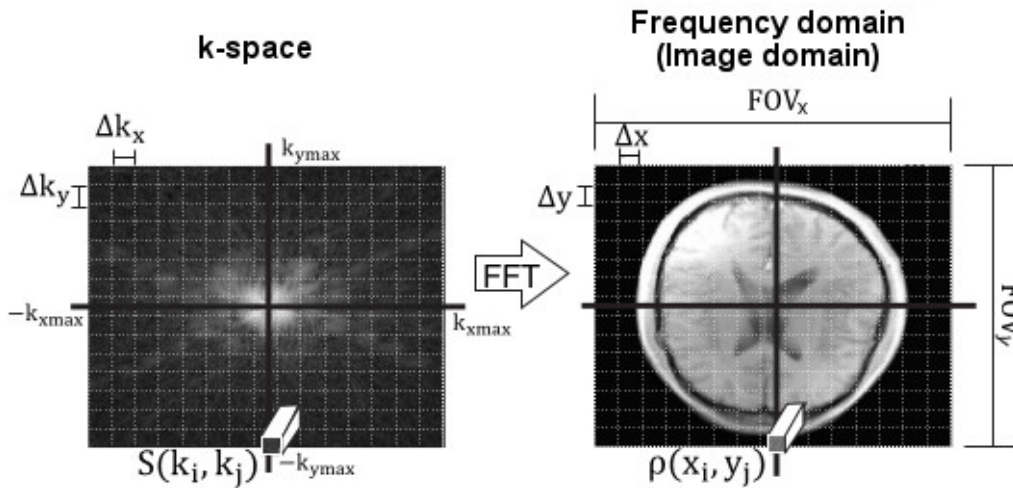


Figure 2.4.2.: Fourier Transformation of the 2D MR signal. K-space samples are separated with distance  $\Delta k_x$  in the horizontal direction and  $\Delta k_y$  along vertical direction. In frequency domain the adjacent copies of the image are separated by the  $FOV = \frac{2\pi}{\Delta k}$  in both directions.

## 2.5. k-space Coverage

In the last section it was demonstrated that the finite sampling of the received  $rf$  signal in combination with the discrete Fourier transform results in the image of the true object. The way data  $s(k_x, k_y)$  is collected, is not mentioned yet. There are many different ways to obtain a signal for each location  $(k_x, k_y)$  and fully cover k-space. Here, the encoding and collection of Cartesian and radial data are presented. More details about many other type of sampling patterns can be found for example in references [22, 21].

### 2.5.1. Cartesian Sampling

To perform the 2-D spatial encoding and to collect the data, gradients in the both principal directions are turned on at different time points. The k-space is divided in  $N_y$  phase encoding lines and  $N_x$  frequency encoding steps.

After the slice selection gradient in  $z$ -direction, a short gradient pulse in the  $y$ -direction determines the phase encoding line to be acquired. Afterwards, a frequency encoding gradient of constant amplitude is active during a time interval of  $N_x \Delta t$ , during which the acquisition of the signal is carried out. Both gradients are applied  $N_y$  times, until the signal from the whole k-space is collected. Finally, the image of the object is obtained by the inverse Fourier transform of the k-space signal.

The temporal graphic representation of not only the gradients but also the  $rf$  signals is known as pulse sequence diagram. To illustrate this, a basic gradient echo sequence [23] is presented (Figure 2.5.1a). It starts at  $t_0$  with the selection of the slice in  $z$ -



direction, where the  $rf$  pulse with a flip angle ( $\alpha$ ) and the slice selection gradient in  $z$ -direction are applied as described in the previous section.

In order to ensure a maximal signal, a gradient in  $z$ -direction reverses the dephasing of spins introduced by the slice-selection gradient. The negative gradient in  $x$ -direction and the phase encoding gradient move to the desired starting point in  $k$ -space for the read out procedure as showed by Figure 2.5.1b.

In the center of the read out gradient, the so called gradient echo is generated as here the total gradient moment on this axis is zero. The time between the  $rf$  pulse and the occurrence of this echo is known as echo time (TE). The whole process is repeated  $N_y$  times, for each repetition changing the strength of  $G_y$  gradient to adjust the  $k$ -space position in direction of  $k_y$ . The time between two  $rf$  pulses is known as repetition time (TR) [22].

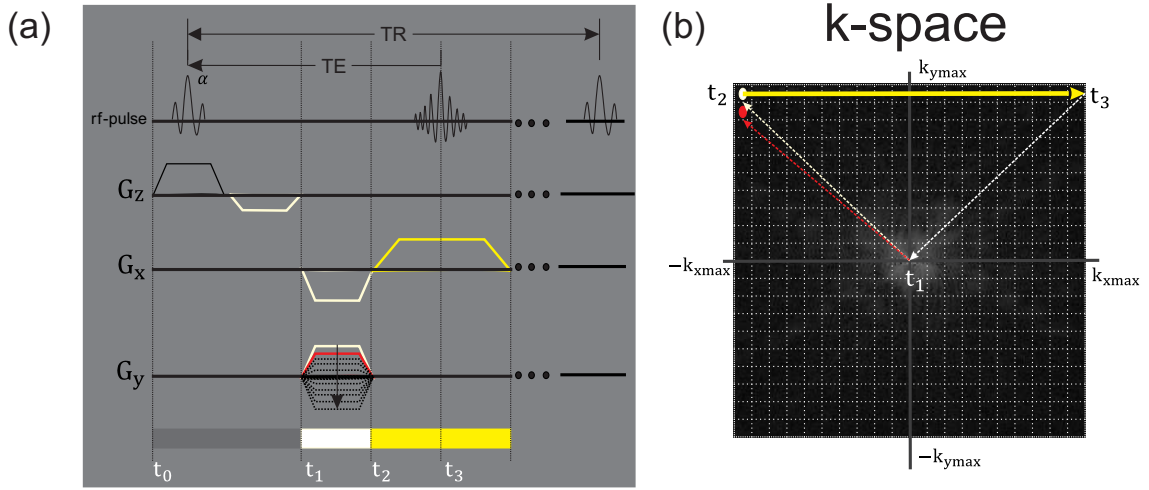


Figure 2.5.1.: Cartesian sampling of the  $k$ -space using a gradient echo sequence: (a) diagram and (b) path performed by the Cartesian FLASH sequence [24].

## 2.5.2. Radial Sampling

In radial coverage of  $k$ -space, first proposed by Lauterbur in 1973 [25], the signal in  $k$ -space is collected along several spokes or projections at different angles  $\theta$ . To generate the radial sampling pattern in  $k$ -space, the gradient in  $x$ -direction ( $G_x$ ) is applied simultaneously with the gradient in  $y$ -direction ( $G_y$ ) with varying amplitudes as can be seen from Figure 2.5.2. To cover the  $k$ -space,  $n_s$  spokes are uniformly distributed along the radial  $k$ -space with:

$$n_s = \frac{\pi}{\Delta\theta} \quad (2.5.1)$$

To avoid aliasing, according to the Nyquist criterion, the largest angular steps ( $\Delta\theta$ ) should be [22] :

$$\Delta\theta = \frac{1}{L \cdot FOV}, \quad (2.5.2)$$

where  $L$  is the diameter of the radial  $k$ -space. This results in a minimum number of

spokes given by:

$$n_s \geq \pi \cdot L \cdot FOV \quad (2.5.3)$$

In a similar way, the minimal number of samples along the spoke is:

$$N_r \geq 2 \cdot L \cdot FOV \quad (2.5.4)$$

The image domain is obtained by applying the non-uniform Fourier transform (NUFFT) [26] or the regridding onto Cartesian grid and then applying the Fast Fourier Transform (FFT).

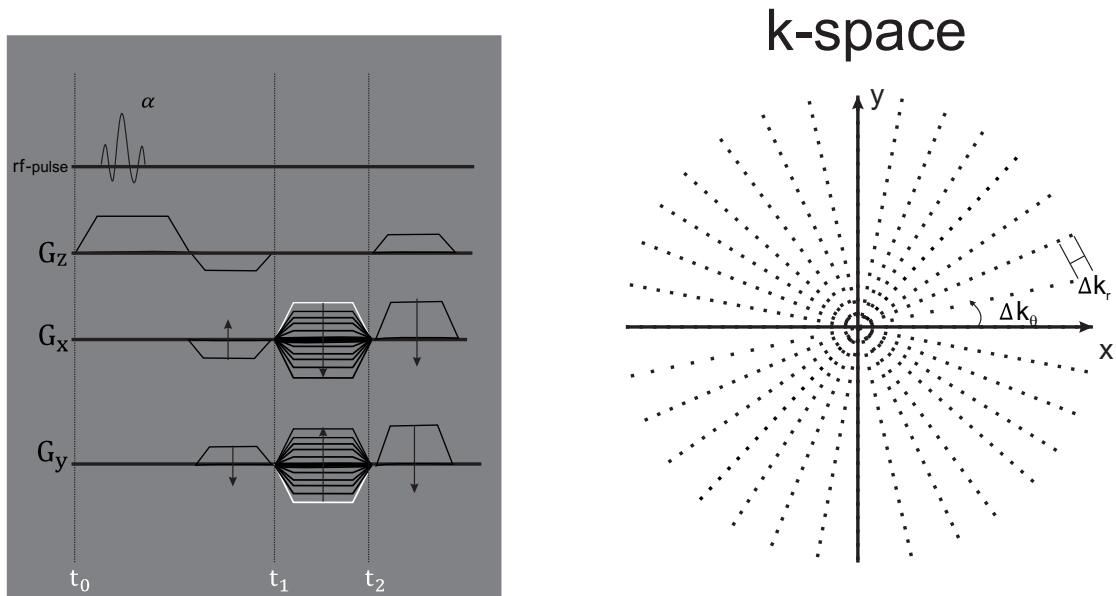


Figure 2.5.2.: Pulse sequence diagram for radial k-space acquisition. Here an example of a radial Steady-state free precession sequence, the gradients on the  $xy$ -axes are modulated according to the orientation of the corresponding spoke (left). Right, the angular acquisition order is schematically depicted.

An important characteristic of radial sampling is that every spoke passes the center of the k-space, which means that each projection samples both low and high frequencies [27] and it has low sensitivity for object motion. By using radial sampling, trading spatial for temporal resolution is easy to achieve, which is not the case for a Cartesian acquisition. However, image reconstruction is more complicated and more time-consuming than for Cartesian sampling and so radial acquisitions are not frequently used in clinical experiments.

## 2.6. Acquisition Time and Signal to Noise Ratio

Important properties of an MR image are determined by the choice of the pulse sequence and its parameters such as repetition time (TR), echo time (TE), flip angle ( $\alpha$ ), matrix size (i.e. number of k-space samples), Field of View (FOV). Therefore, for each application

these parameters have to be carefully considered for the desired effect.

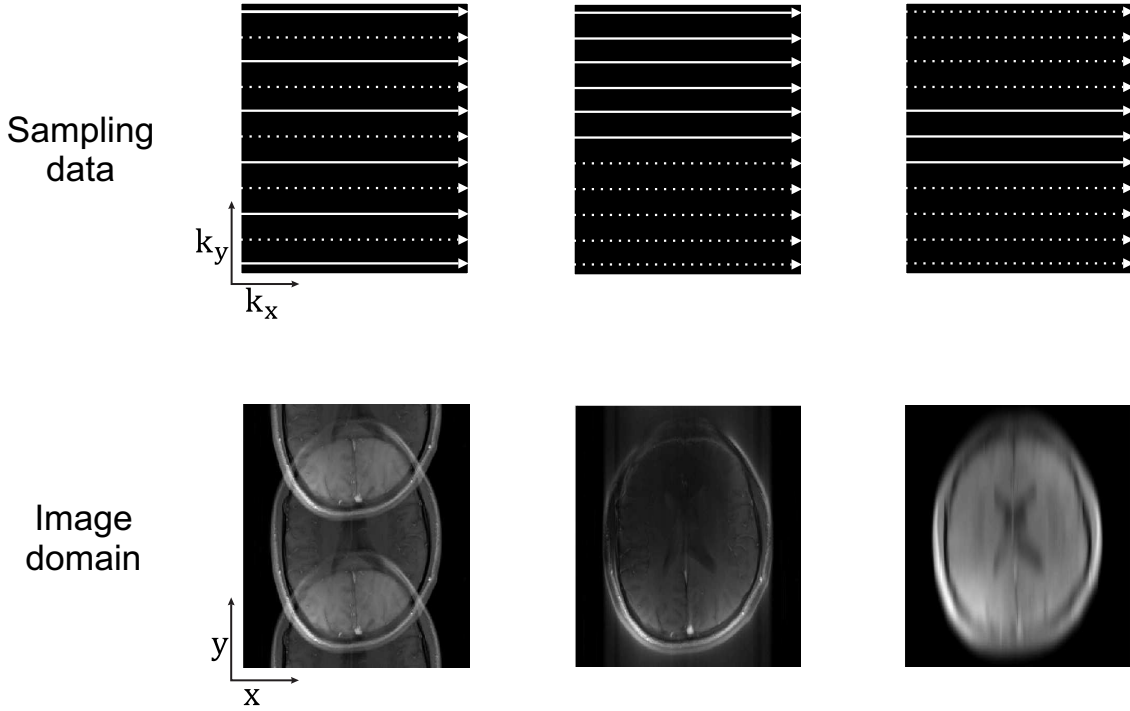


Figure 2.6.1.: The acceleration of the data acquisition can be carried out by skipping some phase encoding lines (a). This idea is used by the Parallel Imaging. The partial Fourier technique is a modification of the Fourier transformation imaging method used in MRI in which the symmetry of the raw data in k-space is used to reduce the data acquisition time by acquiring only a part of k-space data (b). Not acquiring the most peripheral lines in k-space leads to a low-resolution image, where information about much of the fine details is lost (c).

One of the most important measures of image quality is signal-to-noise ratio (SNR), which is defined in the MR community as the ratio of signal amplitude to noise standard deviation. The signal strength depends on the voxel volume ( $\Delta x \cdot \Delta y \cdot \Delta z$ ), since the number of protons scales with the volume. Noise in an image refers to random or systematic undesirable perturbations of signal that arises from the body, electronics and computer calculations. The noise variance is dependent of the receiver bandwidth (BW) of the signal (determined by the gradient field strengths), the size of the image ( $N_x \times N_y$ ) and the number of averaged signals ( $N_{av}$ ). Thus, [21]

$$SNR \propto (\Delta x \cdot \Delta y \cdot \Delta z) \sqrt{\frac{N_{av} N_x N_y}{BW}} \quad (2.6.1)$$

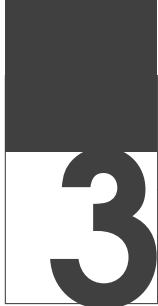
Since the bandwidth  $BW$  is equal to  $\frac{1}{\Delta t}$ , for a 2-D MR experiment we have:

$$SNR \propto (\Delta x \Delta y \Delta z) \sqrt{N_{av} N_x N_y \Delta t} \quad (2.6.2)$$

$$SNR \propto (Voxel Volume) \sqrt{(Acquisition Time)}$$

SNR considerations have implications for the selection of several imaging parameters. In practice, longer acquisition times might be unfeasible. Nowadays in MRI, there is a tendency to reducing acquisition times while having only negligible losses in image quality. To accomplish this goal, reduction in the number of phase encoding steps  $N_y$  and/or shorter TR are required. When reducing  $N_y$ , the location of the omitted lines in k-space has a big influence on the resulting image, as shown in Figure 2.6.1. Omitting phase encoding lines only at the edges of k-space leads to an image of lower resolution, which is undesirable in most cases. Sampling only every n-th line instead results in an image with aliasing artifacts, since this violates the Nyquist criterion. Hence, without further image processing this sampling scheme also cannot be used to obtain diagnostic images. However, the introduction of Parallel Imaging in the 80's made it possible to calculate missing data points through the use of receiver arrays and to remove the aliasing artifacts. This is explained in detail in the next chapter.

The repetition time (TR) can be reduced using different rapid MR sequences, such as FLASH [24], EPI [28], Turbo Spin Echo (TSE) [29]. Additionally the combination of these rapid sequences and Parallel Imaging provide further acceleration in image acquisition techniques.

A large, bold, black number '3' is centered within a white square. The top portion of the square is filled with black, creating a graphic effect where the number '3' appears to be emerging from or attached to the black area.

## Chapter 3.

# Basics of Parallel Imaging

---

## 3.1. Historical Overview

One of the major breakthroughs in fast MRI was the introduction of the concept of multiple receiver coils by Hyde et al. [30] at the end of the 80's and later by Roemer et al. [31]. With this technique, either the SNR can be improved or the image acquisition can be sped up as was proposed by Carlson [32] and by Hutchinson and Raff [33] in their early works of Parallel MRI (pMRI). Using multiple receiver coils, the MR signal is received simultaneously and independently by each element. An example of an array consisting of 8 coils is shown in Figure 3.1.1 an example of an array consisting of 8 coils is shown. Further development has allowed the construction of arrays up to 128 independent coils [34, 35]. In 1988, Hutchinson et al. [33] planted the idea of spatial encoding imaging using only multiple coil arrays without applying magnetic field gradients. One year later, Kelton et al. [36] proposed the use of both multi coil arrays and magnetic field gradients. This technique was based on skipping phase encoding steps and the reconstruction of images without aliasing artifacts using mathematical approaches. However, the reconstruction technique did not provide satisfactory results. This idea was further explored by many other groups [32, 37], with breakthroughs by Sodickson et al. [5], using coil sensitivities to simulate additional phase encoding gradients (Simultaneous Acquisitions of Spatial Harmonics (SMASH)), and Prussman et al. [7], utilizing the coil sensitivities to improve the inversion matrix conditions (Sensitivity Encoding (SENSE)). Following the arrival of these techniques, many reconstruction methods were proposed, which can be classified into two groups: Methods that perform the reconstructions in image domain (SENSE [7], PILS [9]) or in k-space (AUTO-SMASH[6], VD-AUTO-SMASH[10] and GRAPPA [11]). There are also hybrid reconstruction techniques as described in reference [8]. The next section introduces the basic concepts used in parallel imaging.

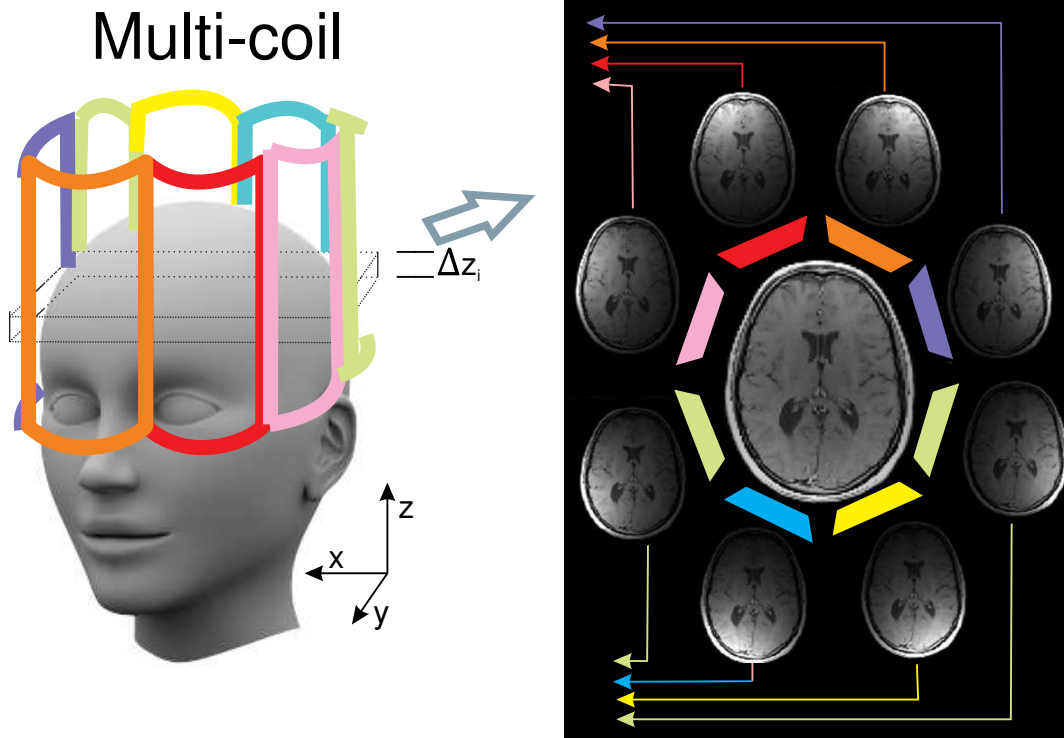


Figure 3.1.1.: Parallel acquisition with multiple coils. Independent coils with individual responses or sensitivities acquire signal from the object simultaneously. This can be seen as an additional “spatial encoding” because each receiver coil has a different “view” of the object.

## 3.2. Basic Concepts

The basic idea of pMRI is to shorten acquisition times by skipping part of the required information and to retrieve it in a post-processing step. In Cartesian k-space sampling, some phase encoding lines are omitted and the final image exhibits aliasing artifacts because the Nyquist criterion is not anymore satisfied. In the following chapter, a detailed description of the aliasing artifacts in the images and some other basic concepts in pMRI are presented.

### 3.2.1. Aliasing

Aliasing artifacts in image domain are the result of undersampling k-space. As described in the previous chapter, skipping phase encoding steps decreases the distance between copies or replicas of the spin density in image domain and due to the violation of the Nyquist criterion, aliasing artifacts emerge in image domain. Figure 3.2.1 illustrates an example of k-space undersampling, where the *FOV* is reduced to half by omitting every other phase encoding step. This therefore results in two overlapping replicas in the image of each individual coil. As a rule, the acceleration of k-space sampling by  $R$  will reduce the *FOV* by the same factor and lead to the overlap of  $R$  replicas in image

domain.

The pMRI techniques take advantage of the fact, that the signal is acquired by different coils with different spatial sensitivities in order to remove the aliasing (see Figure 3.2.1).

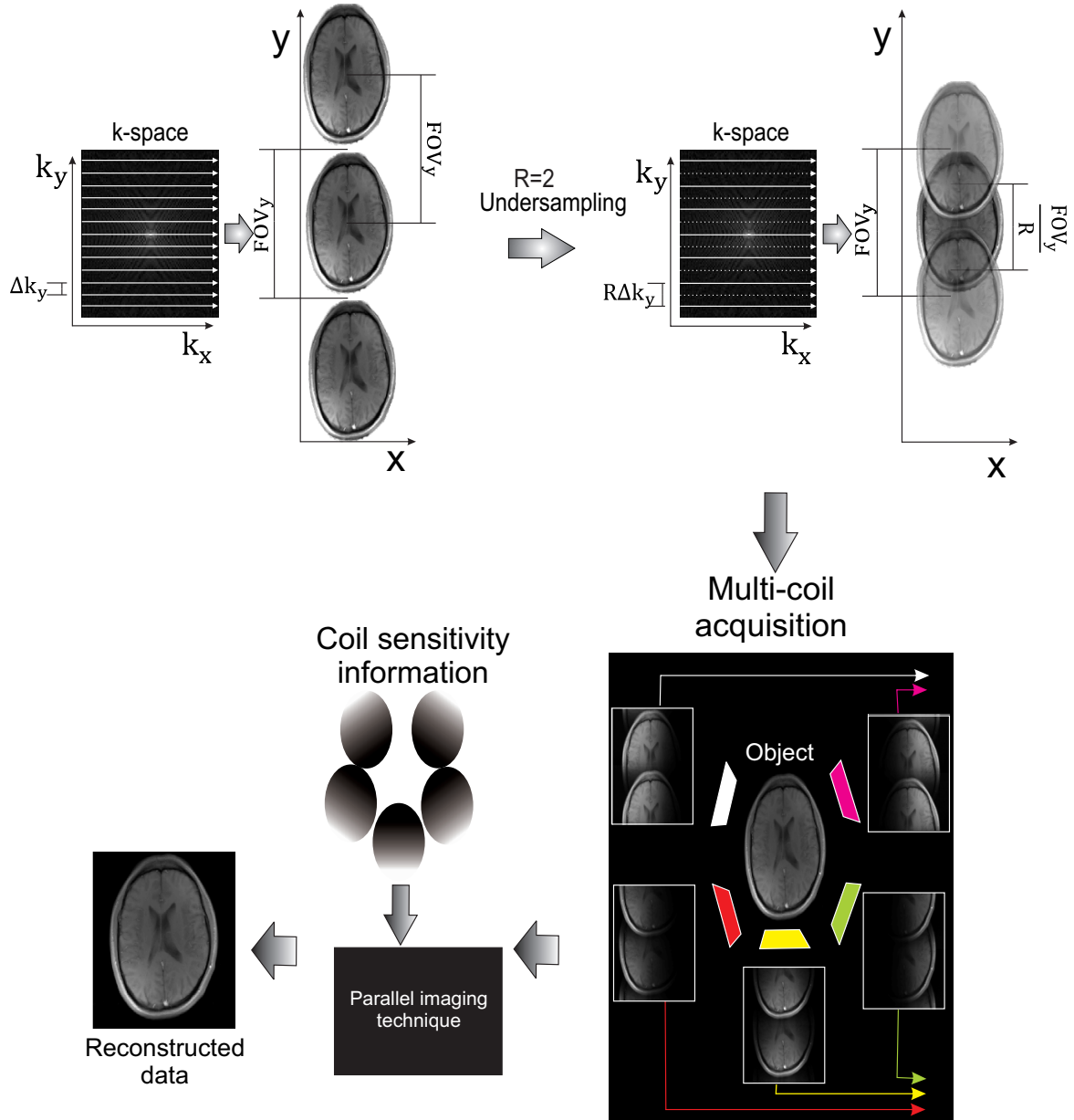


Figure 3.2.1.: Aliasing artifacts in the image domain result from skipping phase encoding steps in k-space (undersampling in  $k_y$  direction).  $R$  represents the acceleration factor, in this example an acceleration factor of  $R = 2$  is shown. Data from multiple coils are used in pMRI to reconstruct the image.

### 3.3. Reconstruction Methods

This section describes basic concepts of the most common parallel imaging techniques. Beginning with a widespread technique, that performs the reconstruction in image domain known as Sensitivity Encoding (SENSE) [7] and followed by a brief description of one of the first reconstruction techniques, Simultaneous Acquisitions of Spatial Harmonics (SMASH) [5] and its successors AUTO-SMASH [6] and VD-AUTO-SMASH [10] which allowed the implementation of a more generalized reconstruction method, Generalized Auto-calibrating Partial Parallel Acquisition (GRAPPA)[11].

Today, there is a big diversity of reconstruction techniques derived from the methods previously mentioned.

#### 3.3.1. Sensitivity Encoding (SENSE)

The reconstruction of aliasing-free images with SENSE [7] is performed in image domain using explicit coil sensitivity profiles, also called coil sensitivity maps. To understand how this reconstruction method works, consider the image with aliasing artifacts shown in Figure 3.3.1 with a reduced  $FOV$ .

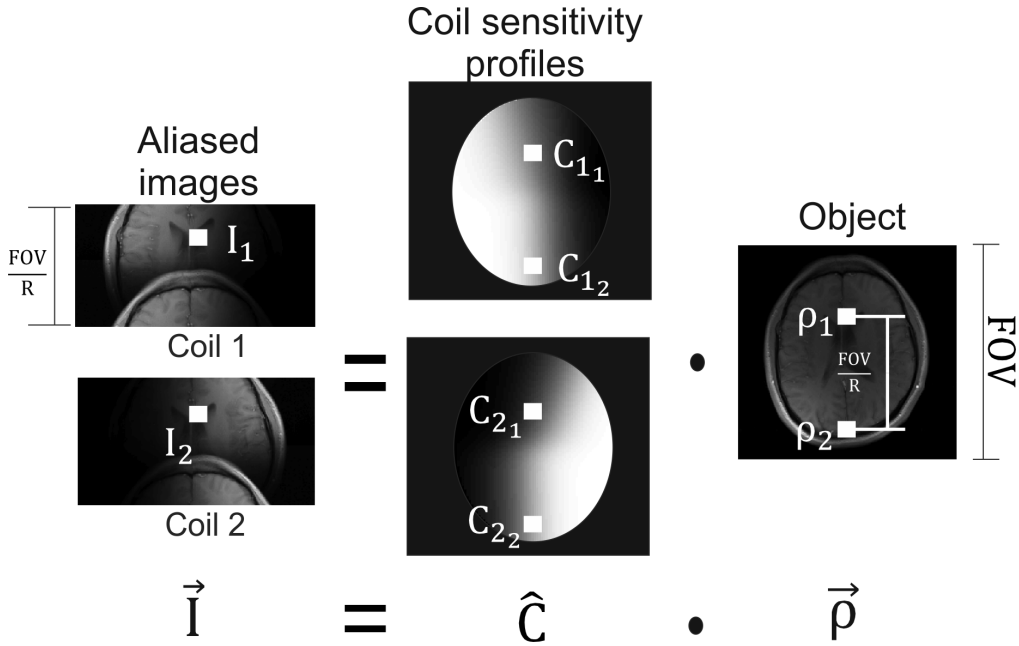


Figure 3.3.1.: Image encoding with multiple coils. In vectorial form,  $\vec{I}$  contains the aliased data from reduced  $FOV$  images. The matrix  $\hat{C}$  is the assembly of the sensitivities of the coils corresponding to the locations of the involved pixels in the full  $FOV$  image  $\vec{\rho}$ .

The undersampling in k-space reduces the  $FOV$  of the image by a factor of  $R$ . That results in the overlapping of  $R$  replicas distributed equidistant with a period of  $\frac{FOV}{R}$  (see Figure 3.2.1). Hence, the intensity of one pixel in the undersampled image is the



superposition of  $R$  pixels with a spacing of  $\frac{FOV}{R}$  of the image with the desirable  $FOV$ , see Figure 3.3.1. Furthermore, the MR signal is collected using multiple coils with different spatial sensitivities, which corresponds to an additional spatial encoding (or weighting) along the  $FOV$ . Therefore, each of the  $R$  pixels overlapped at certain position in the reduced  $FOV$  is weighted by the corresponding spatial sensitivity. We can describe the intensity of a certain pixel acquired by the  $j$ -th coil, as the sum of  $R$  pixels weighted with their coil sensitivities  $C_{j_a}$ :

$$I_j = \sum_{a=1}^R C_{j_a} \rho_a, \quad (3.3.1)$$

where  $I_j$  represents a certain pixel value in the aliased image acquired with the  $j$ -th coil,  $C_{j_a}$  is the coil sensitivity weight corresponding to the pixel at position  $a$  in the image  $FOV$  and  $\rho_a$  corresponds to the unknown spin density value at position  $a$ . In the multi-coil case this can be written in matrix form with  $n_c$  equations:

$$\begin{bmatrix} I_1 \\ I_2 \\ \vdots \\ I_{n_c} \end{bmatrix} = \begin{bmatrix} C_{1_1} & C_{1_2} & \dots & C_{1_R} \\ C_{2_1} & C_{2_2} & \dots & C_{2_R} \\ \vdots & \vdots & \dots & \vdots \\ C_{n_{c1}} & C_{n_{c2}} & \dots & C_{n_{cR}} \end{bmatrix} \cdot \begin{bmatrix} \rho_1 \\ \rho_2 \\ \vdots \\ \rho_R \end{bmatrix}, \quad (3.3.2)$$

or in short form:

$$\vec{I} = \hat{C} \cdot \vec{\rho}. \quad (3.3.3)$$

To obtain the unfolded image, this equation is solved for the spin density vector ( $\vec{\rho}$ ) for every pixel in the reduced  $FOV$ :

$$\vec{\rho} = \hat{C}^{-1} \vec{I} \quad (3.3.4)$$

From this expression it is clear that there are three cases:

- There are fewer equations (or number of coils) than unknowns. In this case the equations system cannot be solved without prior information knowledge about the object.
- There is the same number of equations as unknowns and therefore there are no extra degrees of freedom. It is solved by simply inverting the matrix  $C$ .
- When there are more equations as unknowns, which is the most common case in MRI, the Moore-Penrose pseudo-inverse should be applied to obtain unfolded images:

$$C^{-1} = \text{pinv}(\hat{C}) = (\hat{C}^H \hat{C})^{-1} \hat{C}^H \quad (3.3.5)$$

where  $H$  is the Hermitian transpose of the matrix  $C$ . The noise correlation matrix  $\psi$  describing any correlation (e.g. coupling) between the receiver coils can be incorporated in the inversion in order to improve the SNR.

$$\vec{\rho} = (\hat{C}^H \psi^{-1} \hat{C})^{-1} \hat{C}^H \psi^{-1} \vec{I}, \quad (3.3.6)$$

The encoding efficiency or also called geometry factor [7] indicates how accurate the inversion of the matrix  $\hat{C}$  is performed. In the presence of noise, the geometry factor leads to noise amplification in the final image. The geometry factor can be calculated with:

$$g_i = \sqrt{[(\hat{C}^H \psi^{-1} \hat{C})^{-1}]_{ii} [(\hat{C} \psi^{-1} \hat{C})^{-1}]_{ii}} \quad (3.3.7)$$

where the subscripts  $ii$  indicate the elements of the diagonal matrix. The g-factor value is higher when the sensitivities of the  $R$  pixels are similar because in this case it is more difficult to separate the folded pixels. It has been demonstrated [38], that the SNR of SENSE reconstructions is optimal when the coils sensitivities do not present errors. The encoding efficiency or g-factor can be included in the SNR calculation at every pixel  $i$  by:

$$SNR_i^{SENSE} = \frac{SNR_i^{full}}{g_i \sqrt{R}} \quad (3.3.8)$$

Therefore, the coil sensitivities should present different values between them across the  $FOV$  to ensure a higher SNR (smaller g-factor) in the reconstructed images.

### 3.3.2. Simultaneous Acquisition of Spatial Harmonics (SMASH)

In the SMASH algorithm, coil sensitivity profiles are used in order to estimating the effect of the missing gradient encoding steps. Unlike SENSE reconstructions, the SMASH reconstructions are performed in k-space. To explain the general idea of SMASH, here we will revisit some basic concepts about the acquisition of the MR signal. Every  $k_y$  line or phase encoding step in k-space is obtained by the integration of the *sinc* functions as demonstrated in the last chapter, which consists of spatial harmonic components (i.e. sinusoidal) generated by the gradient  $G_y$  along the  $FOV$ . In Figure 3.3.2, some spatial harmonics are illustrated that carry out this phase encoding process.

A receiver coil array also provides spatial variation. This can be used by linear superposition  $C_{tot}^m$  of the coil sensitivities at a specific location to approximate the missing harmonics, usually generated by the gradient  $G_y$  in  $y$ -direction, as shown in Figure 3.3.3:

$$C_{tot}^{(m)}(x, y) = \sum_{j=1}^{n_c} w_j^{(m)} C_j(x, y) \approx e^{i m \Delta k_y y} \quad (3.3.9)$$

where  $C_j$  is the coil sensitivity of the component coil  $j$  in a  $n_c$  components array,  $w_j^{(m)}$  represents the complex weight factors, which estimate the harmonic of order  $m = 0 \dots R - 1$ ,  $R$  is the acceleration factor and  $\Delta k_y = \frac{2\pi}{FOV}$  the distance between adjacent phase encoding lines in k-space. The weight factors  $w_j$  are calculated from the equation 3.3.9, fitting the coil sensitivity profiles  $C_k(x, y)$  to the spatial harmonics  $e^{i m \Delta k_y y}$ .

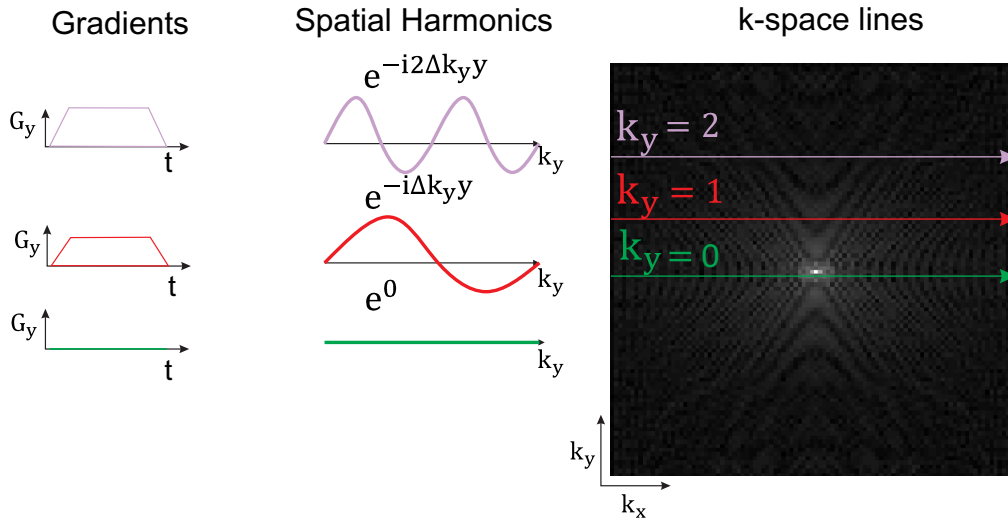


Figure 3.3.2.: Spatial harmonics components generated by the gradient  $G_y$  along the phase encoding direction. SMASH approximates these harmonics from the coil sensitivities directly to reconstruct missing data.

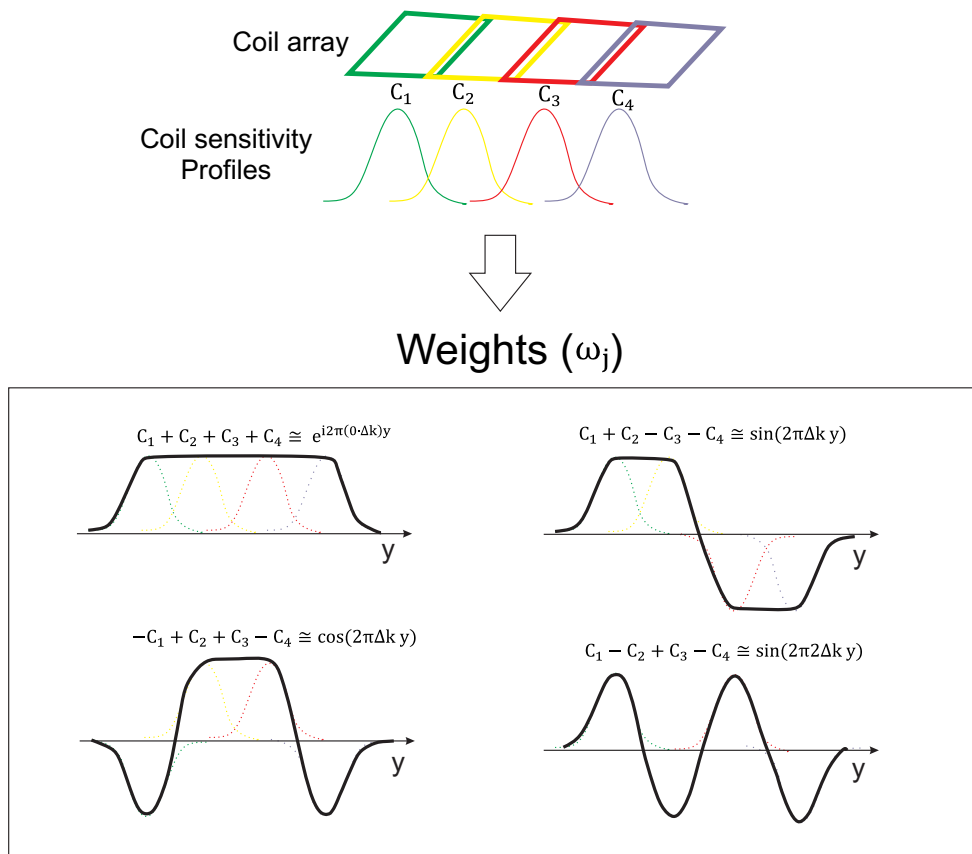


Figure 3.3.3.: Here an example of the generation of composite coil profiles  $C_{tot}^{(m)}$  using weights  $w_j^{(m)}$ .

The missing phase encoding line shifted by  $m \cdot \Delta k_y$  steps is equal to the composite signal ( $S_{tot}^{(m)}$ ) generated by the linear combination of the acquired data of the  $n_c$  single coils ( $S_j$ ) using the weights  $w_j$ . The composite signal is given by:

$$\begin{aligned} S_{tot}^{(m)}(k_x, k_y + m\Delta k_y) &= \sum_{j=1}^{n_c} w_j^{(m)} S_j(k_x, k_y) = \sum_{j=1}^{n_c} w_j^{(m)} \int \int dy dx C_j(x, y) \rho(x, y) e^{-i(k_y y + k_x x)} \\ &= \int \int dy dx \sum_{j=1}^{n_c} w_j^{(m)} C_j(x, y) \rho(x, y) e^{-i(k_y y + k_x x)} \equiv \int \int dy dx \rho(x, y) e^{i m \Delta k_y y} e^{-i(k_y y + k_x x)} \end{aligned} \quad (3.3.10)$$

As with all parallel imaging methods, this method is limited by the spatial variation present across the coils, which are used for the generation of spatial harmonics to estimate missing data.

### 3.3.3. AUTO-SMASH and VD-AUTO-SMASH

Obtaining accurate coil sensitivities may be non-trivial in some regions due to lack of signal (e.g. human lung) or motion between the acquisition of coil sensitivity and accelerated data. Deviations in the coil sensitivity profiles can cause errors in the estimation of spatial harmonics. A further improvement of SMASH was proposed by Jakob et al. [6], in order to avoid these inaccuracies introduced by the coil sensitivity estimation. Instead of using explicit coil sensitivity profiles, AUTO-SMASH, allows the reconstruction of missing data making use of additionally acquired  $R-1$  central k-space lines, called auto calibration signal (ACS).

In this self-calibrating approach the linear weights  $w_j^{(m)}$  are calculated directly from the combination of ACS lines  $S_j^{ACS}$ . In the last section it was demonstrated that the weighted combination of signal across multiple coils ( $S_j$ ) results in the shifting of the signal ( $S_{tot}^{(m)}$ ) by  $m\Delta k_y$ . In AUTO-SMASH, the prior knowledge of the ACS lines allows the derivation of the weight factors in the following way:

$$S_{tot}^{(m)}(k_x, k_y + m\Delta k_y) = \sum_{j=1}^{n_c} w_j^{(m)} S_j(k_x, k_y) \approx \sum_{j=1}^{n_c} S_{ACS_j}^{(m)}(k_x, k_y + m\Delta k_y) \quad (3.3.11)$$

The complex weight factors  $w_j^{(m)}$ , which shift measured lines by  $m \Delta k_y$  in k-space, are determined by fitting the single coil acquired signals  $S_j(k_x, k_y)$  to the composite ACS signal  $S_{ACS_j}^{(m)}(k_x, k_y + m\Delta k_y)$ , as illustrated in Figure 3.3.4. Then the reconstruction process is performed by applying these estimated weights to the undersampled data ( $S_j(k_x, k_y)$ ) in order to calculate the composite  $S_{tot}^{(m)}(k_x, k_y + m\Delta k_y)$  and after the inverse Fourier transform obtaining a full *FOV* image.

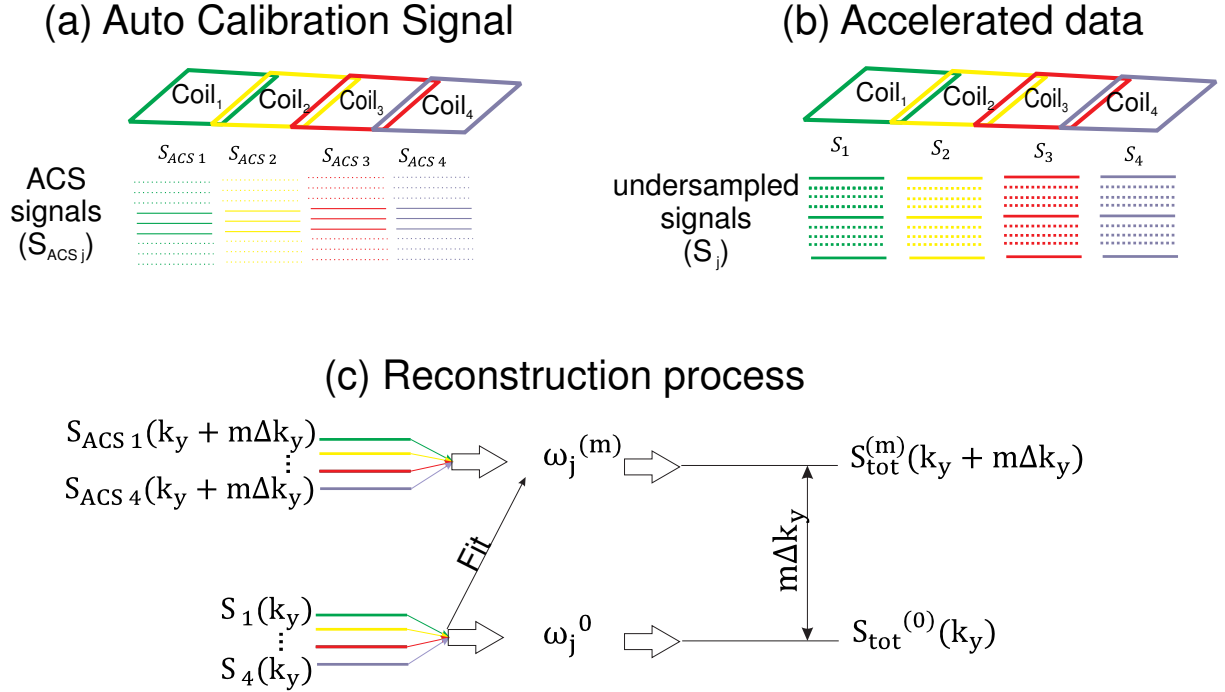


Figure 3.3.4.: Reconstruction process in the AUTO-SMASH algorithm. (a) ACS signals ( $S_{ACS_j}$ ) are used to estimate the weight factors  $w_j^{(m)}$  to (b) reconstruct the undersampled signals ( $S_j$ ). (c) These weight factors are obtained by fitting the single coil acquired signal ( $S_j(k_x, k_y)$ ) to the composite ACS signal  $S_{ACS_j}^{(m)}(k_x, k_y + m\Delta k_y)$ . The missing lines in the composite  $S_{tot}^{(m)}(k_x, k_y + m\Delta k_y)$  are calculated applying the estimated weights to the acquired signals ( $S_j(k_x, k_y)$ ).

The quality of the reconstructed image improves when a larger number of ACS lines is acquired to determine the weights. [10]. To that end, in VD-AUTO-SMASH [10] a higher number of ACS lines is used ( $\sim 16-32$ ) and are sampled in a scheme embedded in the accelerated data shown in Figure 3.3.5. Additionally, the SNR increases when the ACS lines are included in the reconstructed data. By incorporating a k-space based auto-calibrated approach, AUTO-SMASH overcomes the limitation of methods that use the coil sensitivity profiles explicitly.

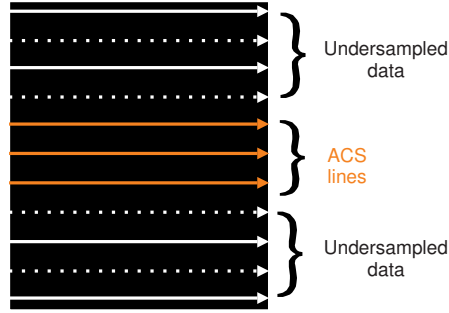


Figure 3.3.5.: VD acquisition scheme used by VD-AUTO-SMASH. 16-32 ACS lines are used to calculate the weight factors  $w_j^{(m)}$ .

### 3.3.4. Generalized Auto-calibrating Partially Parallel Imaging (GRAPPA)

Images reconstructed using AUTO-SMASH and VD-AUTO-SMASH show low SNR due to a non-optimized combination of the signal to form the composite image. They may also exhibit phase cancellation caused by non-aligned phases across coils or slight differences between the residual aliased signal and the unaliased normal data. However, these reconstruction methods paved the way to an approach called Generalized Auto-calibrating Partially Parallel Imaging (GRAPPA)[11]. GRAPPA and VD-AUTO-SMASH both require ACS lines, but differ in the way the reconstruction is carried out. In contrast to VD/AUTO-SMASH, where a single combined image is reconstructed, in GRAPPA unaliased images are reconstructed for each coil. Therefore, a separate set of weights has to be determined for each individual coil:

$$S_k^{acs}(k_x, k_y + m\Delta k_y) = \sum_{j=1}^{n_c} w_{k,j}^{(m)} S_j^{acs}(k_x, k_y), \quad (3.3.12)$$

where  $m = 1 \dots R - 1$ . Similar to AUTO-SMASH, several extra central lines (*ACS data*) are fully acquired and used to calculate the reconstruction weights ( $w_{k,j}$ ). In the GRAPPA algorithm, the shape of a so called kernel (see Figure 3.3.6) can have a large impact on the accuracy of the reconstruction [11]. The smallest reasonable GRAPPA kernel is typically defined by two acquired lines and  $R-1$  missing lines according to the sampling pattern. For the calibration stage, source and target points in the kernel are identified as illustrated in Figure 3.3.6. The kernel is shifted along the *ACS* lines and source and target points for all available kernel repetitions ( $N_{rep}$ ) are collected into the matrices  $S_{scr}$  and  $S_{trg}$  respectively. According to equation 3.3.12, the collected data in  $S_{scr}$  and  $S_{trg}$  are related by:

$$S_{scr}^{(m)} = \hat{w}^{(m)} S_{trg}$$

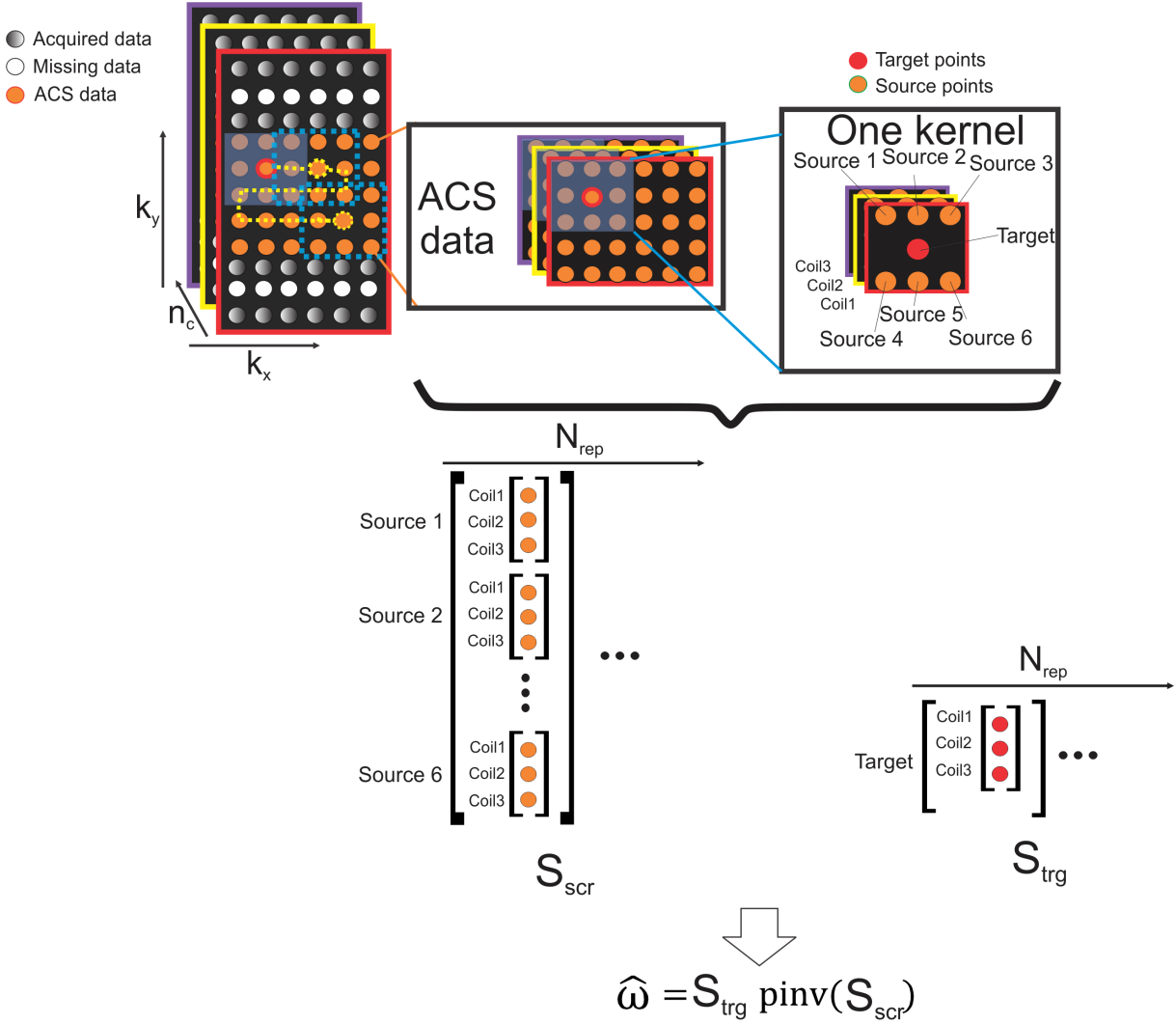


Figure 3.3.6.: Calibration process of the GRAPPA algorithm. In a block wise scheme (kernel), the data along the ACS lines are labeled and collected, according to the sampling pattern, into the  $S_{scr}$  and  $S_{trg}$  matrices. Then the weights  $\hat{w}^{(m)}$  are estimated applying the pseudoinverse (pinv) to the  $S_{scr}$  matrix.

The matrices  $S_{scr}$  and  $S_{trg}$  have the size of  $N_c \cdot N_{bx}^{scr} \cdot N_{by}^{scr} \times N_{rep}$  and  $N_c \cdot (R - 1) \times N_{rep}$  respectively, where  $N_{bx}$  and  $N_{by}$  are the number of source points in the kernel along  $x$ - and  $y$ -directions. The GRAPPA weights ( $\hat{w}$ ) are derived by solving the system of equation 3.3.12, resulting a matrix with size  $N_c \cdot (R - 1) \times N_c \cdot N_{bx}^{scr} \cdot N_{by}^{scr}$ .

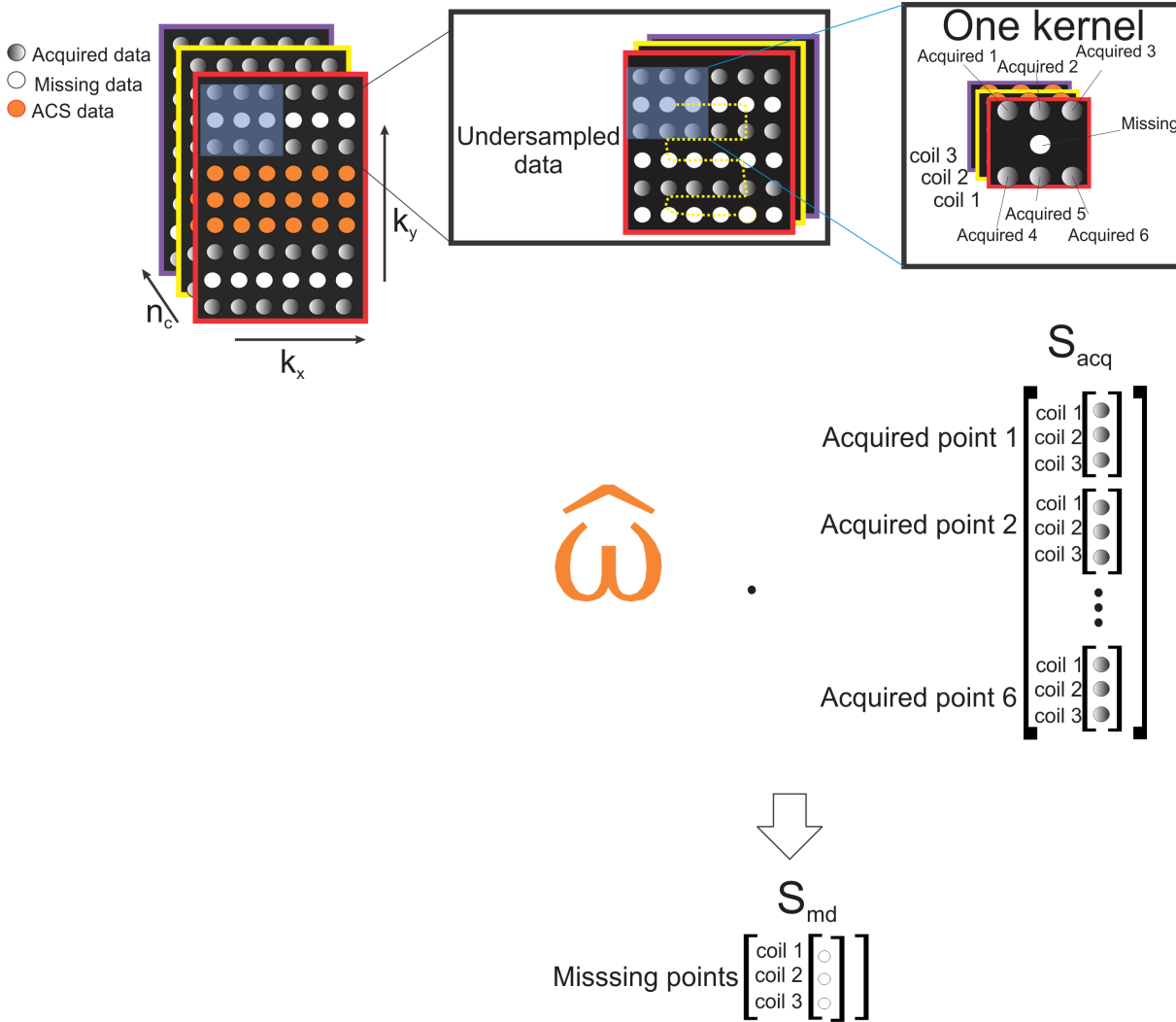


Figure 3.3.7.: The reconstruction step of GRAPPA algorithm. Using the same kernel scheme along the undersampled data, the weights  $\hat{w}^{(m)}$  are applied to the acquired data  $S_{acq}$  to calculate the  $R - 1$  missing data  $S_{md}$  in each coil.

The second stage in the GRAPPA reconstruction process is the application of these weights ( $\hat{w}$ ) along the undersampled data using the same kernel to calculate the  $R - 1$  missing points in each coil as shown in Figure 3.3.7. As a result, A fully sampled  $k - space$  is obtained for each individual coil.

In order to obtain one composite image using the information from all coils, the reconstructed data are typically combined using the sum of squares in each pixel across coils in image domain [31]. Compared to the AUTO-SMASH, this results in a better SNR and additionally avoids phase cancellation. The versatility of this approach has allowed further developments and improvements to this technique. Some examples are the reconstruction in the image domain [39] and the reconstruction of non-Cartesian data sets [40, 41, 42].



### 3.4. Limitations

All pMRI techniques make use of the coil sensitivity information, which can either be obtained by an additional pre-scan or included in the accelerated acquisition. Nevertheless, both of them increase the duration of the acquisition process. Furthermore, high accuracy of the coil sensitivity maps is very important for reconstruction techniques such as SENSE or SMASH, that operate directly in image space, in order to completely remove the aliasing artifacts. Errors in the estimation of coil sensitivity maps may be caused by the voluntary or involuntary motion of the object during the scan, the inhomogeneity of the regions with small signal or in general changes in the object during the in-vivo experiments. Additionally, the physical arrangement of the coils is important in pMRI algorithms for estimating the missing data. However the coil configuration is directly depending on the hardware technology available. Addressing this problem, methods as VD/AUTO-SMASH and GRAPPA do not require explicit coil sensitivities estimations in order to perform the reconstruction. Nevertheless, they still limit the speed of the acquisition due to the acquisition of extra central lines for the *ACS* data. This becomes crucial in cases where the object presents inherent motion or the patients are not able to remain still.

For all parallel imaging methods, decreasing the number of acquired phase encoding lines diminishes the Signal to Noise Ratio (SNR) by a factor of  $\sqrt{R}$  and the g-factor in the reconstructed data. Hence, the quality of the reconstructions will be degraded by the noise enhancement for higher acceleration factors  $R$ . To summarize, there is a tradeoff between the acceleration of data acquisition and the quality of the reconstructed image. The SNR degradation is one of the main reasons, why acceleration factors of merely of 2 or 3 are so far applied in clinical routines, even when many coils are available.

### 3.5. Regularization

In order to obtain unfolded images, in general parallel MRI methods are dealing with inverse problems, which can be ill-conditioned due to noise or coil configurations, in the form:

$$Ax = y \tag{3.5.1}$$

Here  $A$  represents either the coil sensitivity matrix ( $C$ ) in methods such as SENSE and SMASH or the matrix  $S$  in AUTO-SMASH and GRAPPA. The vector  $x$  is the unaliased desired data and  $y$  represents the aliased data. A common approach for finding an approximate solution to this problem is the minimization of the residual  $L_2$ -norm given by:

$$x \min \|Ax - y\|^2 \tag{3.5.2}$$

this approach is known as least-squares solution [43]. However, the presence of small perturbation at the matrix  $A$  produces large perturbation at the output due to the ill-conditioning of the system [44]. Because of this, it is necessary to compute a regularized

solution in which the effect of such noise is filtered out. The classical regularization method developed independently by Phillips [45] and Tikhonov [46] (usually referred as Tikhonov regularization) has the form:

$$\min_x \left\{ \|Ax - y\|^2 + \lambda^2 \|L(x - x_0)\|^2 \right\} \quad (3.5.3)$$

$\lambda$  is a positive constant chosen to control the amount of regularization and it is known as regularization parameter. The matrix  $L(x - x_0)$  is used to constrain the solution with information given by the vector  $x_0$ , which may be an a priori estimation about  $x$ . In many cases when the prior information is not available,  $L$  is chosen as the identity matrix  $I$  in order to give preference to solutions with smaller norms and therefore the reduction of noise in the solution. The regularized solution of the vector  $x$  formally proposed by Phillips [45] is given by the expression:

$$x = (A^H A + \lambda^2 L^H L)^{-1} A^H y \quad (3.5.4)$$

The regularization parameter  $\lambda$  provides a trade-off between the fidelity to the measurements and noise sensitivity. In this formulation, larger values of  $\lambda$  lead to higher weighting of the regularization term and therefore noise suppression in the reconstructed data. Nevertheless, this also results in larger residual norms and aliasing artifacts may appear in the solution [47]. On the other hand, the solution will be dominated by the contributions from the noisy data if too little regularization is imposed. The main idea is that a regularized solution with a small residual norm is not too far from the desired solution. In addition for  $L \neq I$ , Hansen et al. [48] demonstrated that excessive regularization may introduce filtering on the solution. In Figure 3.5.1, with  $L = I$ , three SENSE reconstructions using different amount of regularization, are shown.



Figure 3.5.1.: Three SENSE reconstructions of accelerated data factor 2: with low (left), mild (middle) and with a stronger regularization (right) are shown. Here the noise enhancement effect produce by different regularization parameter values is observed. Higher regularization values may lead to blurring and aliasing artifacts in the reconstructed data, while the noise dominates reconstructions using small amount of regularization.

There are a variety of parameter-choice strategies. For example, the discrepancy principle method [49] chooses the regularization parameter such that the residual norm for the regularized solution satisfies [48]:

$$\|Ax_{reg} - b\| = \|e\|$$

This method is based on a good estimate for the norm of the perturbation of the right-hand side ( $\|e\|$ ). Methods such as the L-curve criterion [50], generalized cross-validation [51], and the quasi-optimality criterion [49] do not require the estimation of  $\|e\|$ , but instead seek to extract the necessary information from the given right-hand side.

All these strategies allow finding the optimal regularization parameter to avoid artifacts in the resulting image.

### 3.6. Summary

Parallel Magnetic Resonance Imaging techniques significantly reduce the acquisition time by undersampling k-space, which leads to aliased images. Dedicated techniques such SENSE and SMASH recover the missing data relying on explicit knowledge of spatial coil sensitivity profiles. Other reconstruction methods as AUTO-SMASH and GRAPPA require a fully sampled part of k-space for calibration.

In clinical routines today, both SENSE and GRAPPA algorithms are used to recover the missing data and to remove the aliasing artifacts from the images. The main drawback of these techniques is the reduction of the SNR caused by the reduction of acquired data and its g-factor, which degrade the reconstructed data [52].

# 4

## Chapter 4.

# Basics of Dynamic Parallel Imaging

Dynamic Magnetic Resonance Imaging (dMRI) refers to the acquisition of a series of images in order to monitor the object's changes over time. The same imaging sequence with same parameters is repeated several times in order to capture the dynamics of the object. To be of diagnostic value, images should have a certain spatial and temporal resolution enough to detect smooth changes in the object. Some acquisition strategies, such as ECG-gated CINE [53] take advantage of the periodicity of cardiac cycle in patients by collecting only a fraction of the data (also called a segment) during one heartbeat. Multiple heartbeats are necessary to obtain the final image. It allows the reduction of motion artifacts with high temporal resolutions. Problems using this technique arise when the periodicity of the cardiac cycles is affected by cardiac diseases or when patients can not hold their breath over multiple heartbeats.

A major challenge for MRI is real time imaging, which requires a frame rate of 25 images/s. Important applications include the monitoring of swallowing process, speech movements, catheter guidance, and cardiac arrhythmias among others. To properly visualize these processes, fast acquisition sequences combined with parallel imaging reconstruction techniques can be used, allowing considerable improvement of temporal resolution. However, there is usually a compromise between temporal and spatial resolutions in real time imaging, and typically spatial resolution is sacrificed to achieve higher temporal resolutions. Moreover, as described earlier, the need of low resolution reference lines to estimate coil sensitivities for pMRI increases slightly the scanning time limiting the spatio-temporal resolution of the images.

For accelerated dynamic data, the reconstructions can be performed frame by frame using any of the pMRI reconstruction methods described in the last chapter. On the other hand there exist reconstruction methods specifically for dynamic data, which use the time domain as an additional dimension where the signal can be separated. In the UNaliasing by Fourier-encoding the Overlaps using the temporaL Dimension (UNFOLD) [12] technique, a temporal interleaved undersampling scheme and filtering processes contribute to separate the temporal spectra generated by the acceleration of the dynamic data. An interleaved undersampling scheme has been exploited also by auto-calibrating methods: TSENSE [13] and TGRAPPA [14]. Additionally, reconstruction methods as

kt-BLAST/kt-SENSE [15], kt-GRAPPA [54], PEAK-GRAPPA [55] and kt-PCA [16] take advantage of spatio-temporal correlations in the dynamic data. For reconstructions, they use prior knowledge of the dynamics of the object obtained by a series of low resolution images also called training data.

## 4.1. Sampling Patterns for Dynamic Imaging

In 2-D dynamic imaging, the representation of the data is extended to a third dimension [56]  $(x, y, t)$  as depicted in Figure 4.1.1a. The raw data are acquired in k-space at different time points  $t$  and their k-t representation describes the arrangement in which the data points are collected at each time frame, as shown by the sampling patterns in Figure 4.1.1b and c. Since the data along the read-out direction ( $k_x$ ) are fully sampled, this dimension is omitted from now on.

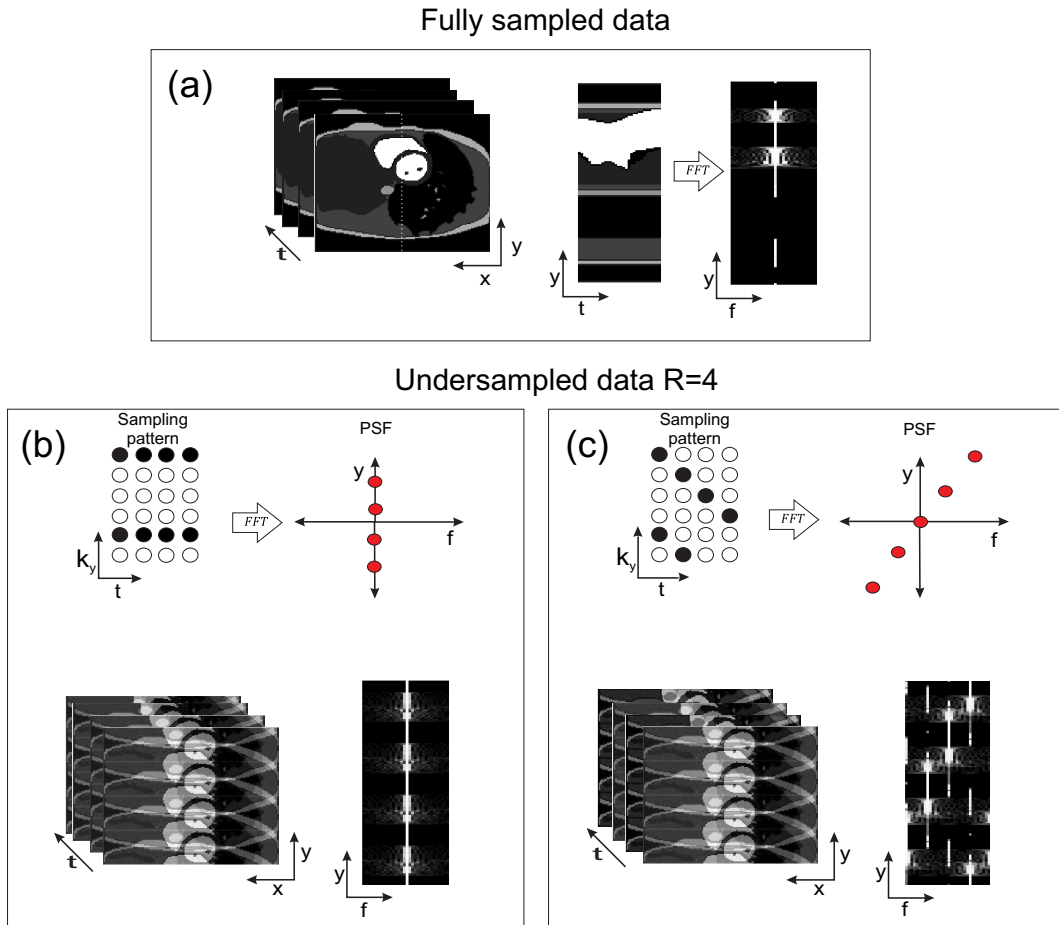


Figure 4.1.1.: Representation of fully sampled data of: (a) temporal images (left), data along the white line (middle), this representation is also called M-mode, and the  $y$ - $f$  representation of the data (right). (b) The representation of the sampling pattern and the Point Spread Function of accelerated data factor 4 without shifting along time and (c) with shifting of one phase encoding line over the time.

According to the properties of the Fourier transform, discrete regular sampling in  $k$   $t$ -space leads to periodic replication in the reciprocal space  $y$ - $f$ . Here,  $f$  is the Fourier-domain of the discrete variable  $t$ , known as temporal frequency. The distribution of these replicas is dictated by the point spread function (PSF), which is the inverse Fourier transform of the sampling pattern, exemplified in the Figure 4.1.1b and c. The spatial acceleration of the  $k$ -space shortens the distance between replicas in  $y$  direction, see Figure 4.1.1b. Additionally, from the Fourier shift theorem, the shift of the sampling pattern in  $k_y$  with time generates alternation of the PSF in  $f$  direction leading to a shift of the replicas (Figure 4.1.1c).

The concept of this interleaved acquisition scheme has been exploited first by UNFOLD [12] and then by other reconstruction methods presented in the following sections.

## 4.2. Temporal SENSE (TSENSE)

The TSENSE reconstruction method proposed by Kellman et.al [13] combines UNFOLD [12] and SENSE concepts in order to either improve the suppression of aliased components, when the data are not static enough to separate their spectra, or to achieve higher acceleration factors. Additionally, the interleaved phase encoded acquisition, first proposed by Koestler et al. [57], allows the estimation of coil sensitivities from the accelerated data without a separate calibration acquisition. Considering the equation 2.4.2, the  $k$ -space sampling and its Fourier transform pair can be represented by:

$$s(k_x, k_y, t) = S(k_x, k_y, t) \times d(k_x, k_y) \xrightarrow{FFT} \hat{\rho}(x, y, t) = C(x, y) \cdot \rho(x, y, t) \otimes D(x, y) \quad (4.2.1)$$

where  $d(k_x, k_y)$  and  $D(x, y)$  are the sampling function in  $k$ -space and image domain respectively. The discretization leads to the periodic  $\hat{\rho}(x, y, t)$  function with a period of  $l \frac{2\pi}{\Delta k}$  as demonstrated previously in Chapter 2. The reduction of phase encoding lines by a factor of  $R$  causes aliased images and a shift in phase encoding direction over the time (interleaved sampling pattern) is exploited by TSENSE as in UNFOLD. This interleaved sampling represents an encoding process in the time domain, separating the temporal spectrum of each aliased pixel in the image domain, as shown in Figure 4.2.1.

In matrix form the aliased time series of images can be represented by:

$$\begin{bmatrix} \tilde{\rho}_1(x, y, t) \\ \vdots \\ \tilde{\rho}_{n_c}(x, y, t) \end{bmatrix} = \begin{bmatrix} C_1(x, y \pm n \frac{FOV}{R}) & \dots & C_1(x, y \pm n \frac{FOV}{R}) \\ \vdots & \ddots & \vdots \\ C_{n_c}(x, y \pm n \frac{FOV}{R}) & \dots & C_{n_c}(x, y \pm n \frac{FOV}{R}) \end{bmatrix} \times \begin{bmatrix} \rho(x, y \pm n \frac{FOV}{R}, t) \\ \vdots \\ \rho(x, y \pm n \frac{FOV}{R}, t)(-1)^t \end{bmatrix} \quad (4.2.2)$$

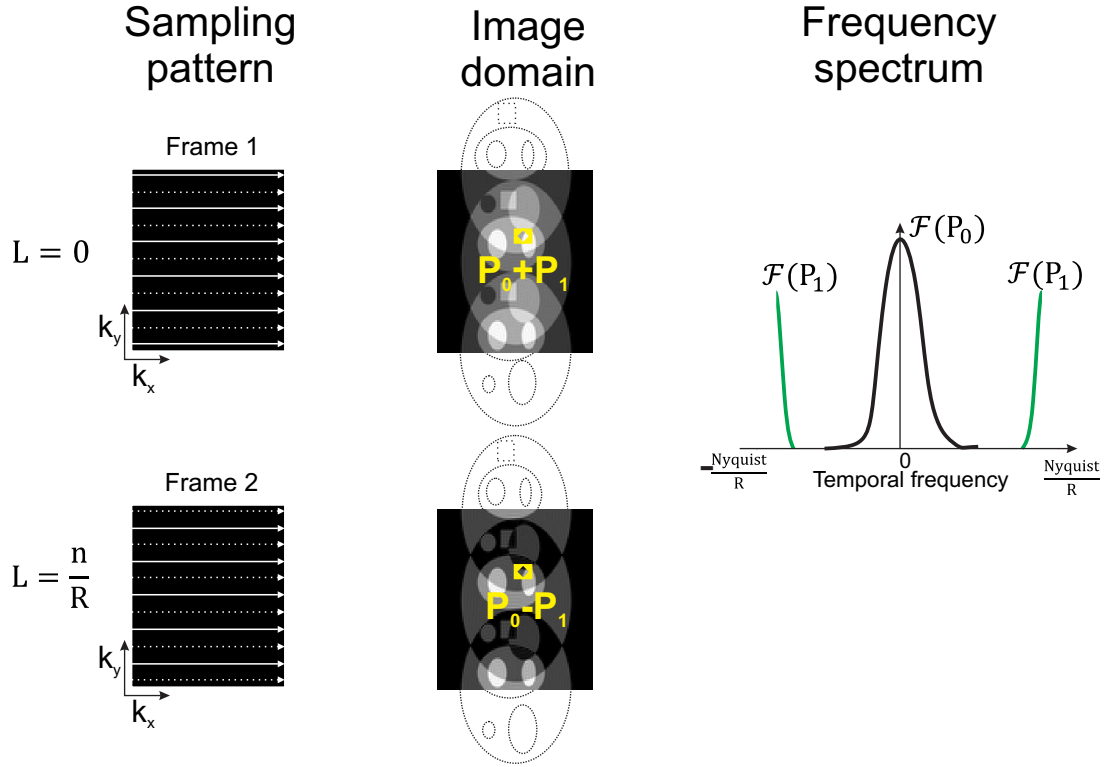


Figure 4.2.1.: Encoding over time of a series of images by a shifting in phase encoding direction (interleaved sampling pattern). The shift ( $L$ ) in the sampling pattern corresponds to a linear phase shift in its Point Spread Function (PSF) according to the Fourier shift theorem. For  $R = 2$ , it results in a change of sign in the aliased components in image domain ( $\mp P_1$ ). The spectrum at each aliased pixel contains information about the dynamics of the desired pixel ( $P_0$ ) around the temporal frequency 0 (or Direct Component, DC) and information of the dynamics of the aliased component ( $P_1$ ) around the Nyquist frequency.

where  $n = 0, 1, \dots, R - 2$ ,  $n_c$  means the number of coils and the term  $(-1)^t$  represents the alternating sign factor due to the interleaved sampling. In this reconstruction method, the desired unaliased images are produced by the SENSE formulation:

$$\vec{\rho}_{SENSE} = (\hat{C}^H \psi^{-1} \hat{C}^H)^{-1} \hat{C}^H \psi^{-1} \vec{\rho} \quad (4.2.3)$$

The original TSENSE uses the results of these reconstructions as a first pass reconstruction taking advantage of the spatial encoding. As a second step, a low-pass temporal filtering (UNFOLD) is performed in order to filter the residual aliased components on the SENSE reconstructions, which might be produced by the imperfections of the coil sensitivities estimation. The TSENSE reconstruction process is shown in Figure 4.2.2.

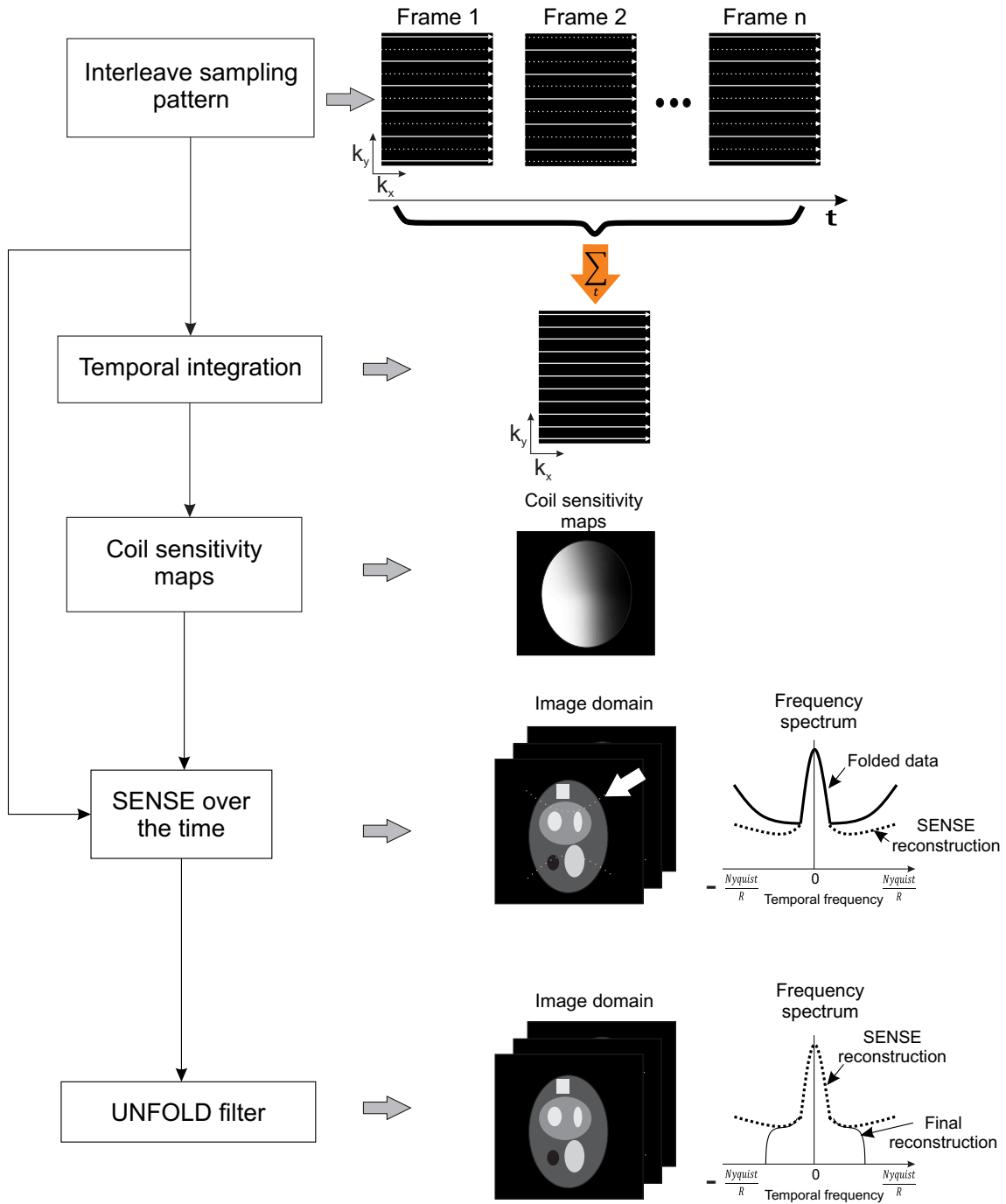


Figure 4.2.2.: Conventional TSENSE. An interleaved acquisition scheme allows the estimation of the coil sensitivities from the temporal integration of the accelerated data without need of additional scanning. These estimated coil sensitivities are used in SENSE reconstructions at each temporal frame. Afterwards the residual aliased components (indicated by the white arrow on the SENSE reconstructed image) that might be present after applying conventional SENSE reconstructions over time are reduced by the application of an UNFOLD filter.



The temporal integration of data will result in full spatial reference images used for the estimation of coil sensitivities performing the auto calibration of the reconstruction method, as illustrated Figure 4.2.2. More recent implementations of TSENSE take advantage of the higher number of coils nowadays available. These results in less residual artifacts after the SENSE reconstruction and therefore the low-pass filtering may not be necessary.

The big advantage of the TSENSE over SENSE is the auto-calibration, which allows to obtain coil maps with a high spatial resolution and avoids residual artifacts due to motion.

### 4.3. Temporal GRAPPA (TGRAPPA)

Analogous to TSENSE, temporal GRAPPA (TGRAPPA) is an auto-calibrating method. Proposed by Breuer et.al [14], TGRAPPA performs the reconstructions using the UNFOLD acquisition scheme. Temporal GRAPPA (TGRAPPA) reconstructs the time series of images frame by frame using sliding block implementation GRAPPA reconstructions. The ACS full resolution reference data are estimated integrating at least  $R$  adjacent time frames in k-space as illustrated in Figure 4.3.1. The ACS lines estimated in this way will contain the information about the changes in coil position over the time due to patient motion. It has been demonstrated that TGRAPPA reconstruction using  $\sim 3 \cdot R$  adjacent frames for calibration is more robust in the presence of undesired motion (e.g. respiratory motion) [14] and further applications for free-breathing imaging.

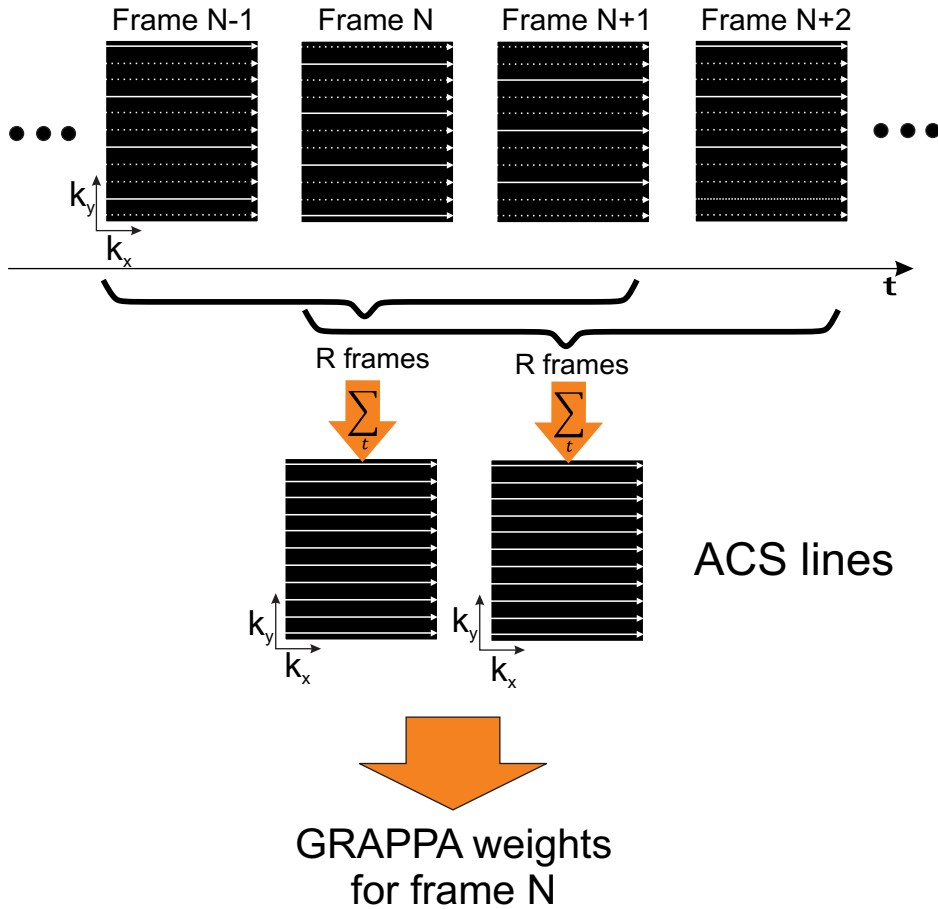


Figure 4.3.1.: TGRAPPA: temporal integration of undersampled data set in interleaved fashion is carried out to estimate the full resolution ACS data. In the presence of motion artifacts, it is recommended to integrate  $3R$  adjacent frames for calibration.

TGRAPPA as well as TSENSE, using the combination of the interleaved acquisition scheme for calibration, avoid the acquisition of extra  $k$ -space central lines and furthermore the limitation in spatial resolution in conventional GRAPPA. Furthermore, no low pass filtering is performed in this reconstruction method.

#### 4.4. kt-SENSE

In dynamic images, there are regions within the  $FOV$  that exhibit motion and regions which remain almost static over the time. As a consequence there is a certain amount of spatial and temporal redundancy in dynamic data. These data correlations are exploited by  $kt$ -BLAST/ $kt$ -SENSE [15] in order to remove the temporal aliasing. Spatio-temporal correlations are learnt using prior information provided by a training data set acquired additionally to the accelerated data, as Figure 4.4.1 depicts.  $kt$ -SENSE utilizes not only spatio-temporal correlations but also spatial coil sensitivity variations in order to separate the aliased signals.  $kt$ -BLAST is the particular case of  $kt$ -SENSE with one

receiver coil.

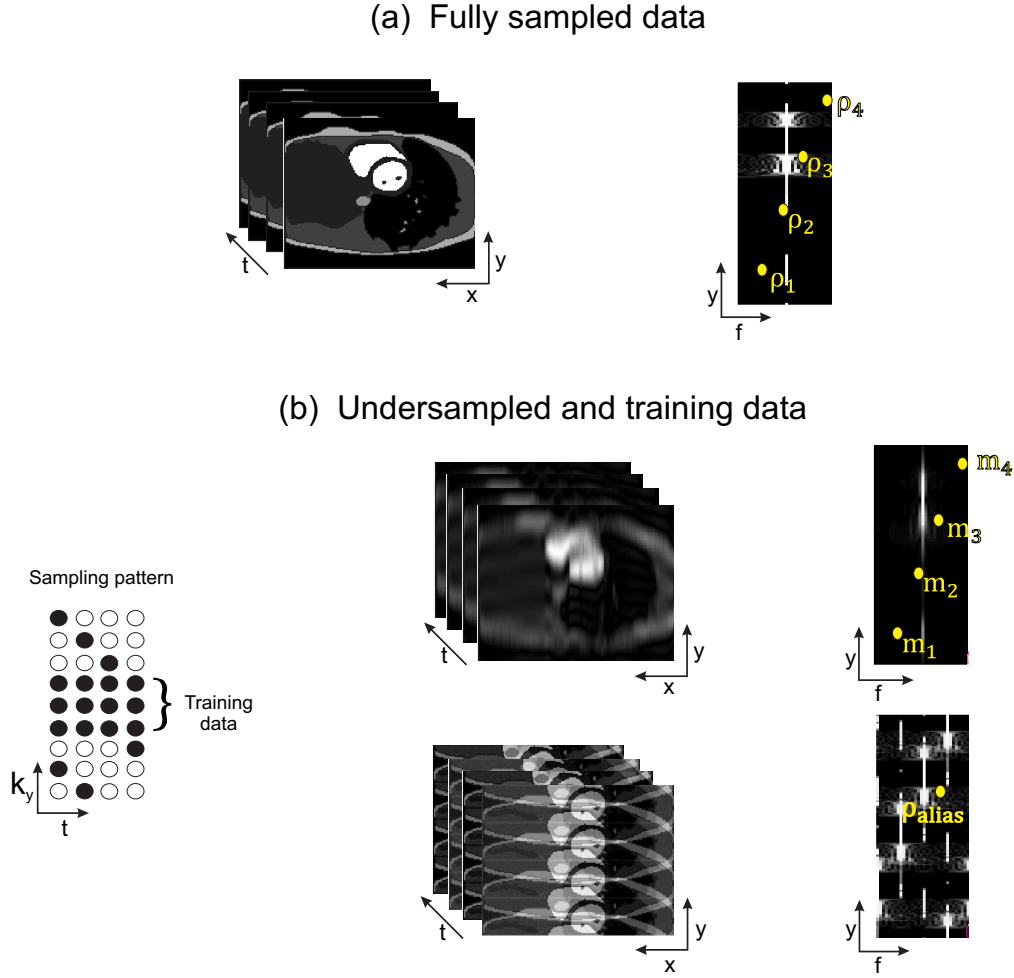


Figure 4.4.1.: In the Figure is illustrated a: (a) fully sampled dynamic data set and (b) a typical sampling scheme based on and suitable for auto-calibration.

Furthermore both kt-BLAST/kt-SENSE control the aliasing artifact in the frequency domain by shifting the sampling pattern along the time in order to minimize the overlapping areas of high intensity as described above.

From now on, we consider the data in the  $(x, y, f)$  domain where  $f$  denotes the temporal frequency.  $R$ -fold subsampling in a temporally shifted fashion results in aliasing in which  $R$  locations of the true object data ( $\rho$ ) in the  $(x, y, f)$  domain are mapped into a single pixel in the aliased data ( $\rho_{alias}$ ) as illustrated by Figure 4.4.1.

The kt-SENSE method calculates the vector ( $\rho$ ) of unaliased signals using a regularized solution:

$$\rho = (C\psi^{-1}C^H + \lambda(M^2)^{-1})^{-1}C^H\psi^{-1}\rho_{alias} \quad (4.4.1)$$

Hereby,  $M^2$  is the covariance matrix of the prior information from the aliased voxels,  $C$  is the sensitivity encoding matrix,  $\psi$  the noise covariance matrix of the receiver coil

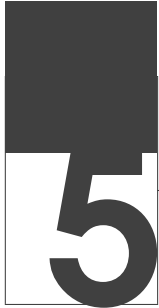
array and  $\lambda$  is the regularization parameter that determines the degree of regularization. Typically  $M^2$  is a diagonal matrix with the diagonal entries  $m_1$  to  $m_R$  along the diagonal, see Figure 4.4.1b.

The information contained in the matrix ( $M^2$ ) should be as close as possible to that of the true object ( $\rho$ ) and an accurate estimation of the coil sensitivities ( $C$ ) will be required in order to obtain reasonable results.

On the one hand, kt-SENSE enables high acceleration rates of the data and its reconstructions exhibit high SNR [58]. On the other hand, the need for the acquisition of extra training lines restricts acceleration of the process. Additionally, the limited resolution of the training data may lead to temporal filtering (i.e. temporal blurring). The amount of temporal filtering can be controlled varying the parameter  $\lambda$  in equation 4.4.1.

## 4.5. Summary

The acquisition and reconstruction of a dynamic image series has been a big challenge for MRI. Dedicated methods like TSENSE, TGRAPPA, kt-SENSE and many more address this problem using sampling methods and numerical techniques that allow higher acceleration factors and good quality data reconstructions. A limitation of some of these methods is the need for extra training information, which also reduces the effective acceleration factor, in order to perform the reconstruction. Additionally, the training information should exhibit high accuracy.



---

## Temporal Filtering Effects in Dynamic Parallel MRI

To overcome some of the limitations of dynamic MR image acquisition mentioned in the introduction, new reconstruction strategies have been proposed in the early 2000's. Among them are auto-calibrating pMRI techniques for dynamic images, which have the principal goal of reducing the scan time without sacrificing spatial resolution. Additionally preserving the temporal resolution of accelerated measurements, auto-calibrating reconstruction techniques employ the undersampled data itself to produce images with full spatial resolution and to avoid extra acquisitions of reference images. The TGRAPPA [14] method, for example, averages at least  $R$  undersampled temporal frames in order to estimate reconstruction weights required for the calculation of missing data. This auto-calibrating method does not introduce temporal filtering during the reconstruction process. However, the SNR of reconstructed images may not be optimal at higher acceleration factors.

Other dedicated methods such as TSENSE [13], kt-SENSE [15] or SENSE-UNFOLD [59], which utilize coil sensitivity maps explicitly for data reconstruction, can potentially also be auto-calibrating techniques. Interleaved acquisition schemes along the temporal axis yield full resolution images when performing a temporal integration of aliased data. These reference images can be used to estimate coil sensitivity maps. The temporal average image (also called direct current (DC)) represents the constant component of dynamic data and it is localized at zero frequency in a  $x - f$  representation (see previous chapter). However, it was demonstrated for Cartesian sampling [60, 61, 62] that the DC calculated in this way may contain additional aliased components. This may lead to signal loss in temporal frequency spectra of reconstructed images [63, 64] and consequently temporal filtering effects in the reconstructed data.

With recent advances in gradient hardware and sequence design, radial sampling for dynamic imaging has become a renewed area of research [65, 22]. Radial sampling fills the k-space with radial spokes as described in Chapter 2. Images obtained from undersampled radial data exhibit streaking artifacts which look like texture patterns and keep the object visible even at high acceleration factors. This is a major difference

to undersampled Cartesian images, where coherent aliasing artifacts appear. Although radial trajectories have many favorable intrinsic properties with respect to the demands of dynamic MRI [66], in this section we focus on the distribution of its aliasing artifacts that will be useful for our purpose.

It is demonstrated that in contrast to Cartesian imaging, temporal filtering effects are not significantly present in auto-calibrated reconstructions of radial undersampled data due to the incoherent nature of aliasing artifacts. The origin of the temporal filtering effect as well as its reduction by applying a GRAPPA filter to DC images are described in the following paragraphs.

## 5.1. Theory

### 5.1.1. Temporal Filtering Effect

The temporal integration of interleaved Cartesian undersampled data generates a fully sampled image as described in the last chapter. In auto-calibrating methods, this averaged image is used to estimate coil sensitivity maps or a regularization parameter map. From here on, the temporal average of the Cartesian undersampled data will be represented by the variable  $DC_{und, cart}$ . In general, the temporal average of a series of images corresponds to the signal at temporal frequency equal to zero ( $f = 0$ ). The temporal average calculated using fully sampled acquisitions ( $DC_{true}$ ) differs from  $DC_{und, cart}$ . This is demonstrated in the following paragraphs.

The interleaved acquisition of a series of images in frequency domain expressed in terms of its point spread function (PSF) can be written as:

$$\rho_{und, cart}(x, y, f) = PSF(x, y, f) \otimes \rho_{true}(x, y, f) \quad (5.1.1)$$

where the PSF is the Fourier transform of the encoding function (PSF)  $E(k_x, k_y, t)$ :

$$PSF(x, y, f) = FFT(E(k_x, k_y, t))$$

Cartesian interleaved undersampling  $\rho_{und}$  is therefore given by:

$$\rho_{und, cart}(x, y, f) = \sum_{n=0}^{R-1} \rho_{true}\left(x, y - n \frac{FOV}{R}, f - n \cdot \frac{f_{max}}{R}\right) \quad (5.1.2)$$

Hereby  $f_{max}$  is the highest temporal frequency sampled. Since the DC term is the component at zero temporal frequency,  $DC_{und, cart}$  can be calculated by:

$$DC_{und, cart}(x, y) = \sum_{n=0}^{R-1} \rho_{true}\left(x, y - n \frac{FOV}{R}, -n \cdot \frac{f_{max}}{R}\right)$$

From this equation, it can be seen that  $DC_{und, cart}$  is the superposition of the temporal average of fully sampled data ( $DC_{true} = \rho_{true}(x, y, 0)$ ) and signals from different spatial and temporal locations.

$$DC_{und, cart}(x, y) = DC_{true} + \sum_{n=1}^{R-1} \rho_{true}\left(x, y - n \frac{FOV}{R}, -n \cdot \frac{f_{max}}{R}\right) \quad (5.1.3)$$

The sum to the right over  $1 \leq n \leq R - 1$  is related to aliasing artifacts. Equation 5.1.3 demonstrates that the temporal average of Cartesian undersampled data contains undesirable components from aliased terms as illustrated in Figure 5.1.1. Hence, the use of  $DC_{und, cart}$  to calculate coil sensitivity maps leads to errors in the auto-calibrating kt-SENSE reconstruction process which may cause temporal filtering in reconstructed images. Since errors are present in the coil sensitivity matrix, the calculation of its pseudo-inverse in the kt-SENSE algorithm misestimates the reconstructed vector at the temporal frequencies  $n \cdot \frac{f_{max}}{R}$  with  $n = 0, 1, \dots, R - 1$ . Therefore the auto-calibrating kt-SENSE algorithm is not able to recover the signal at these temporal frequency points. Figure 5.1.1 shows the signal nulls produced at the aliased components in the spectrum of reconstructed data. The specific form of the aliasing artifacts depends on the sampling scheme.

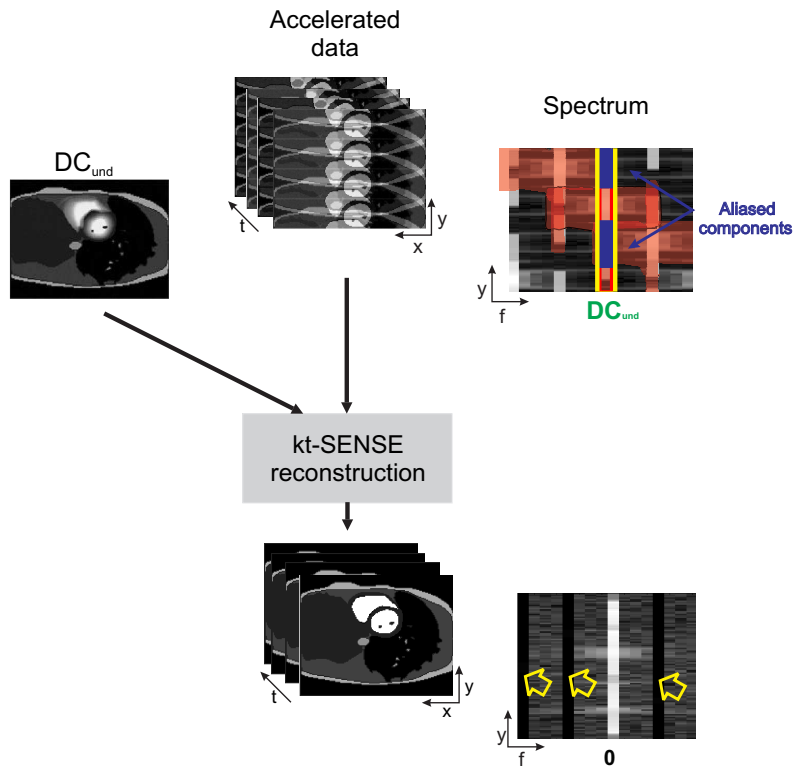


Figure 5.1.1.: The  $DC_{und}$  (highlighted in yellow on the spectrum of the accelerated data) of an interleaved undersampled data set might contain undesirable components caused by the aliased terms (highlighted in blue) from copies of the spectra (highlighted in red). Using the  $DC_{und}$  in the kt-SENSE process might result in inaccuracies in the estimation of coil sensitivities and consequently null-signals in the reconstructions (indicated by the yellow arrows in the spectrum of the reconstructed data).

### 5.1.2. Reducing Temporal Filtering Effect

Temporal filtering effects can be reduced if a more accurate estimation of the temporal

average of the true object ( $DC_{true}$ ) is employed. Since the GRAPPA method can be seen as a spatial convolution filter in image domain [39], performing a GRAPPA reconstruction on the  $DC_{und, cart}$  term may be able to attenuate the inherent aliasing artifacts [60]. In addition, it has been demonstrated that the insignificant temporal filtering introduced by TGRAPPA makes it suitable for the estimation of the  $DC_{true}$  term. The application of GRAPPA weights to the  $DC_{und, cart}$  term is equivalent to performing a TGRAPPA reconstruction and then integrating over the reconstructed frames to estimate  $DC_{true}$  with a lower computational cost. According to Blaimer et al. [60], the use of a GRAPPA filter over the  $DC_{und, cart}$  signal reduces or even eliminates the effects of the right hand sum term in equation 5.1.3, resulting in a better estimation of  $DC_{true}$ . In other words, the signal nulls on the temporal frequency spectra can be avoided using the filtered temporal average ( $DC_{und, cart - filt}$ ) to estimate more accurate coil sensitivity maps.

A different way to avoid temporal filtering effects in the reconstructed images is to use sampling patterns with incoherent undersampling artifacts. While equidistant Cartesian undersampling patterns lead to coherent interference and the probability to superposition is high, some non-Cartesian trajectories provide incoherent aliasing artifacts decreasing this probability. In the next sections, radial trajectories are investigated in order to demonstrate that the incoherence of their aliased components allows the calculation of a more accurate  $DC_{true}$  estimation term by averaging an interleaved radial acquisition ( $DC_{und, rad}$ ).

Analogous to the Cartesian interleaved sampling, to cover the complete k-space when combined into a single image, an interleaved acquisition scheme can be implemented for radial data. Here all projections are rotated by a constant angle for the acquisition of the subsequent frames as illustrated in Figure 5.1.2.

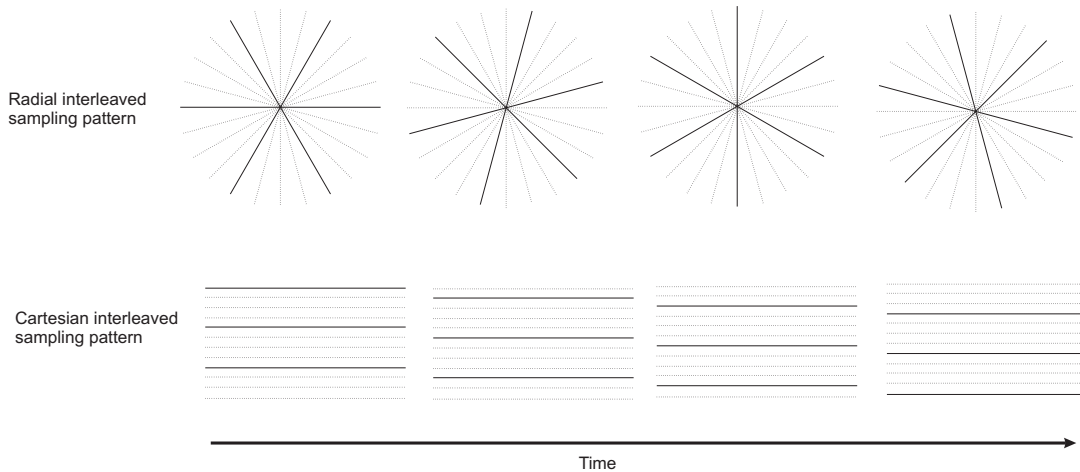


Figure 5.1.2.: Radial and Cartesian interleaved sampling scheme.

The PSF of radial sampling consists of a central peak surrounded by an artifact-free circular region and streaking artifacts outside this region. The diameter of the artifact free region is proportional to the number of radial views included in the reconstruction



(see Figure 5.1.3). In image domain, streaking patterns appear at a respective distance from the individual points. Because of the incoherence of the aliased components, the hypothesis is that temporal filtering effects are not significantly present in accelerated dynamic parallel MRI experiments using radial sampling patterns.

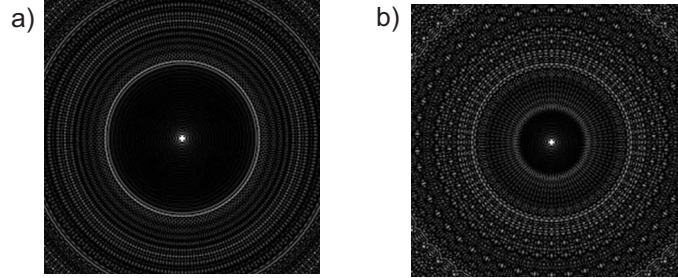


Figure 5.1.3.: Point spread function (PSF) of: a fully sampled radial trajectory (a) and a reduced number of projections (b).

### 5.1.3. kt-SENSE for non-Cartesian Data

The kt-SENSE reconstruction algorithm for undersampled Cartesian data was described in the last chapter and is given by equation 4.4.1. In general, for arbitrary subsampled trajectories, the kt-SENSE image reconstruction is performed by solving:

$$D(E\psi^{-1}E^H + \lambda(M^2)^{-1})\rho = DE^H\psi^{-1}\rho_{alias} \quad (5.1.4)$$

Hereby,  $E$  represents the linear combination of coil sensitivity functions and gradient encoding and  $D$  (also called preconditioning matrix) corresponds to density correction [67]. Solving this equation for  $\rho$  by calculating the inverse of the left hand term would require immense amounts memory and computation time due to the large sizes of the matrices and vectors involved. However, a solution can also be obtained using the iterative conjugate gradient method [68], which is used by the kt-SENSE algorithm and that reconstructs missing points for arbitrary trajectories [67] as described in Figure 5.1.4.

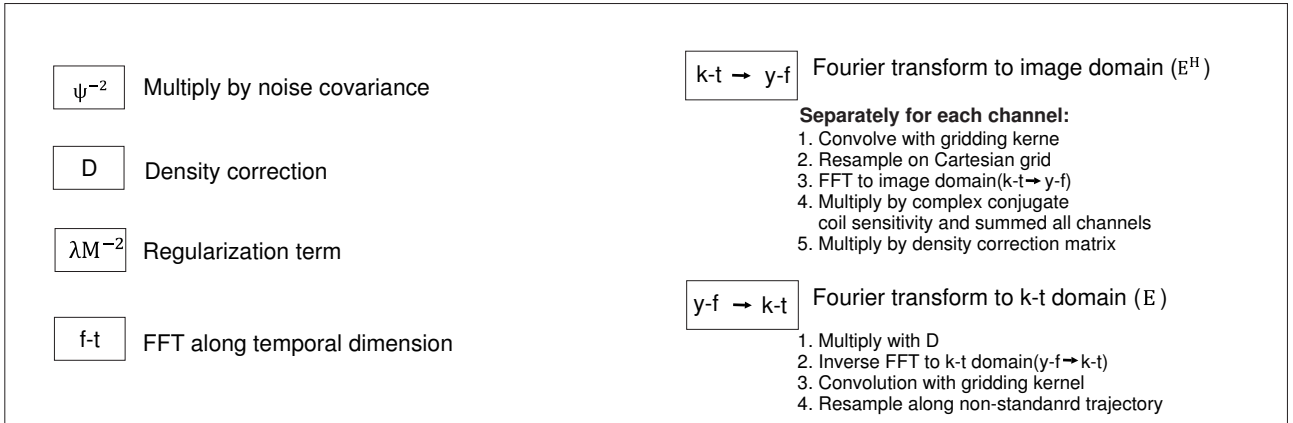
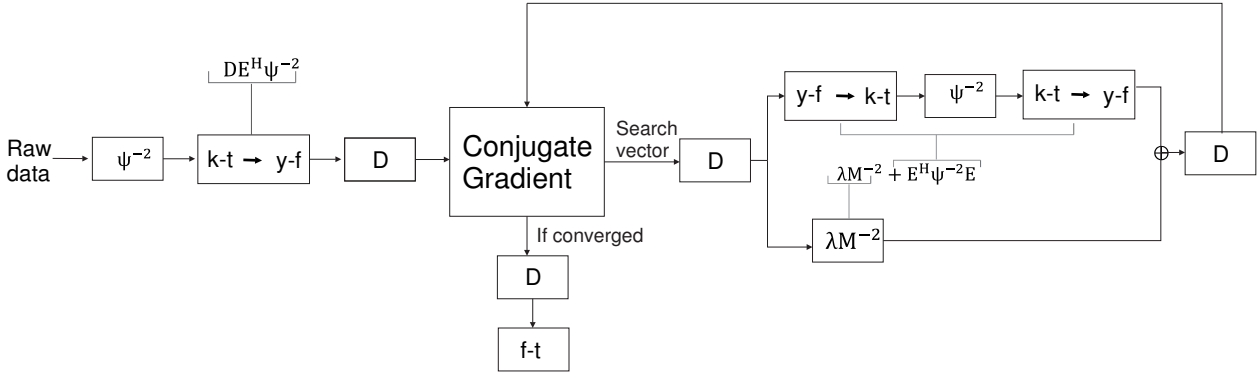


Figure 5.1.4.: kt-SENSE method for non-Cartesian trajectories using a CG algorithm. The first step is to form the right hand side term of equation 5.1.4. The multiplication with  $E^H$  corresponds to gridding the data from each channel onto the points of a Cartesian grid, followed by the Fourier transform (FFT). The resulting images are individually multiplied by complex conjugate coil sensitivity and linearly combined. For each iteration step, a search image vector is multiplied by the matrix  $(E\psi^{-1}E^H + \lambda(M^2)^{-1})$ . The conjugate gradient is used to iteratively update the search and solution vectors. This process continues until convergence. Scheme adapted from [67].

The basic idea of the preconditioning matrices is to reduce the number of iterations, but it is not necessary. Optionally, an intensity correction can also be added to this equation as preconditioning term (here omitted). For lower regularization parameters  $\lambda$ , Cartesian and non-Cartesian kt-SENSE reconstructions can be compared. For comparison of both reconstructed data, in this chapter just small values of  $\lambda$  are used.

## 5.2. Methods

### 5.2.1. Simulations

Simulations were performed using a synthetic dynamic data set designed to simulate cardiac motion, shown in Figure 5.2.1. A fully sampled radial (192 projections per frame)

and a fully sampled Cartesian data set with a base resolution of 192 were generated. Random noise was added to these images. Both data sets were accelerated by a factor of  $R = 4$  in an interleaved scheme. The undersampled data sets were reconstructed using kt-SENSE algorithms for Cartesian [15] and radial [69] trajectories with estimated coil sensitivities obtained by the temporal integration of the undersampled data,  $DC_{und,card}$  and  $DC_{und,rad}$  respectively. All the simulations and reconstructions were carried out using the MATLAB (Mathworks, Natick, MA, USA) programming environment.

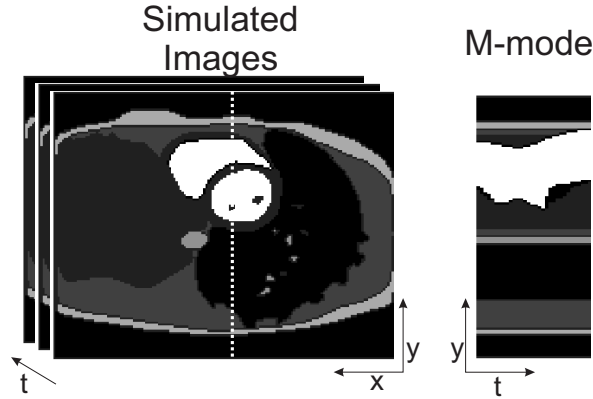


Figure 5.2.1.: The simulated data set with a matrix size of  $192 \times 192$  pixels and 32 time frames. The data set was multiplied by coil sensitivity maps obtained by Biot-Savart calculations. The M-mode along the indicated white line is displayed.

For comparison, reconstructions were performed with coil sensitivity maps obtained by the GRAPPA filtered temporal average as described in [60]. The spectra of the reference and the reconstructed data for both sampling schemes were compared. Their spectra were analyzed by detecting the presence of null components and the temporal blurring in the  $y - t$  representation of the reconstructed data.

### 5.2.2. In-vivo Measurements

In addition, retrospective gated cardiac CINE TrueFISP experiments were performed on a 1.5 T clinical scanner (Siemens Medical Solution, Erlangen, Germany). All experiments were conducted on healthy volunteers. Written informed consent was obtained before the imaging session.

The parameters of the fully sampled Cartesian CINE TrueFISP experiment were: TE = 1.4 ms, TR = 2.8 ms, flip angle =  $50^\circ$ , 32 phases per cardiac cycle and a matrix size of  $192 \times 192$ , Field of View (FOV) of  $350 \times 263$  mm<sup>2</sup>, temporal resolution of 50 ms per segment and 12 receiver channels. Fully sampled radial data were also simulated with 192 projections per frame. Both Cartesian and radial data were retrospectively undersampled using the interleaved  $R = 4$  scheme. The undersampled data sets were reconstructed with kt-SENSE for Cartesian and radial trajectories employing  $DC_{und,card}$  and  $DC_{und,rad}$ , respectively, to calculate the sensitivity maps. After reconstruction, the spectra of the reference and the undersampled data sets were compared.

Additionally, an accelerated Cartesian CINE data set with interleaved sampling scheme was acquired with: acceleration factor 4, TE = 1.4 ms, TR = 2.8 ms, flip angle = 50°, a matrix size of 192 x 168, FOV of 350 x 263 mm<sup>2</sup>, 16 phases per cycle and 12 receiver channels. This data set was reconstructed with kt-SENSE using coil sensitivity profiles calculated with the  $DC_{und, cart}$  and the filtered  $DC_{und, cart-filt}$ .

A radial CINE TrueFISP experiment was conducted with the following parameters: TE= 1.7 ms, TR=3.4 ms, 192 projections with 192 read out points, FOV of 350 x 263 mm<sup>2</sup>, 12 receiver channels. Subsequently, the data were undersampled by a factor of 4. The undersampled data were reconstructed with kt-SENSE for non-Cartesian trajectories using coil sensitivity maps calculated from  $DC_{und, rad}$ .

## 5.3. Results

### 5.3.1. Simulations

Figure 5.3.1 shows the comparison of both DC terms from simulated interleaved Cartesian and radial undersampled data. Errors in  $DC_{und, cart}$  coming from the aliased components are evident in the difference images and were highlighted with arrows.

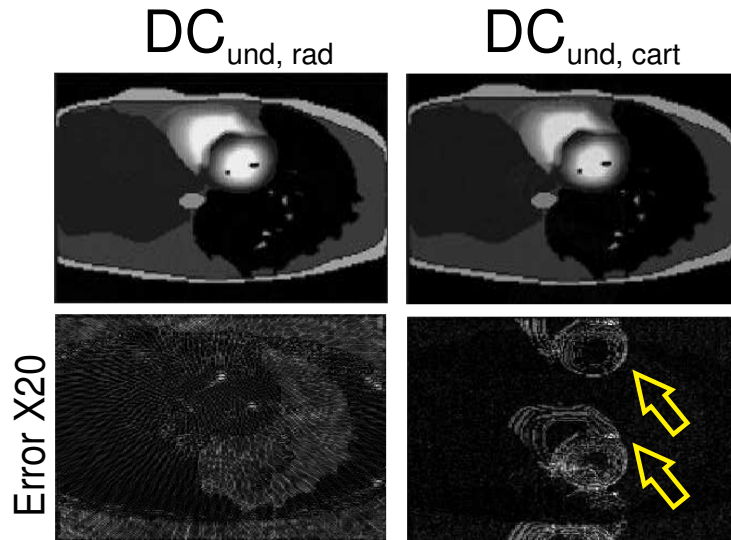


Figure 5.3.1.: DC images calculated by Cartesian ( $DC_{und, cart}$ ) and radial ( $DC_{und, rad}$ ) interleaved undersampled data. The difference images highlight the errors produced by the coherent aliasing in the Cartesian undersampled data.

In general, temporal average terms ( $DC$ ) represent the static signal of dynamic data. Accordingly,  $DC$  images usually appear blurred at dynamic regions. It has been demonstrated that the difference between  $DC_{true}$  term of the true object and  $DC_{und}$  terms from interleaved undersampled data reveals errors as shown in Figure 5.3.1. Aliasing artifacts in  $DC_{und, rad}$  have noise-like appearance while they are coherent in  $DC_{und, cart}$ . Furthermore, errors are present in auto-calibrating Cartesian and radial kt-SENSE re-

constructions as a consequence of inconsistencies in the coil sensitivity maps (see Figure 5.3.2).

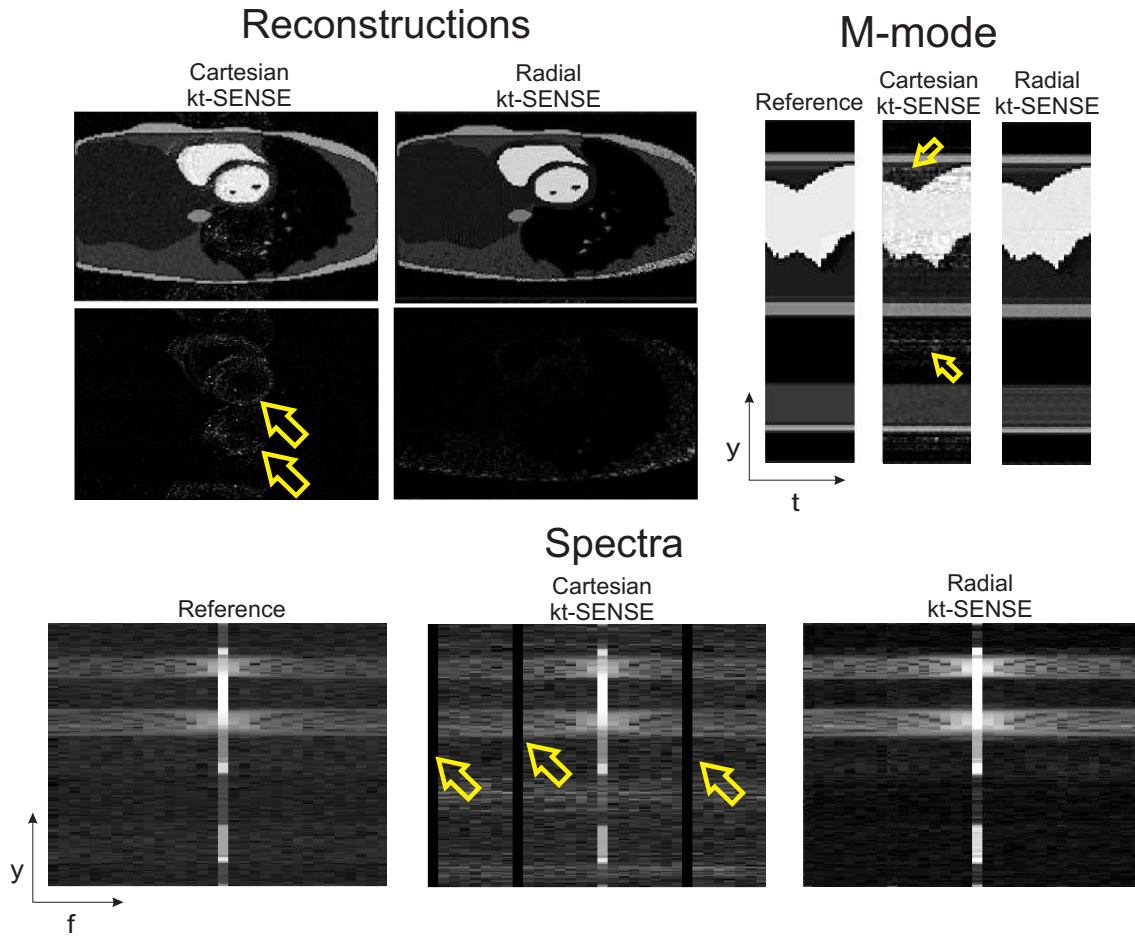


Figure 5.3.2.: Sample frame and deviations from the reference of auto-calibrating kt-SENSE reconstructions using Cartesian and radial data. Additionally the M-mode and the spectra of the data sets are displayed.

However, temporal filtering effects are only evident in Cartesian reconstructions. The artifacts in the reconstructed data are also visible in the M-mode graphics (pointed out by arrows). On the contrary, signal nulls and temporal filtering effects seem to be negligible in reconstructed radial data.

### 5.3.2. In-vivo Measurements

#### 5.3.2.1. Full Resolution Cartesian In-vivo data

The DC terms from retrospectively undersampled in-vivo data sets were calculated and employed in the reconstruction of the Cartesian and radial data. The errors in  $DC_{und, cart}$  with respect to the reference are not perceivable to the eye in this example and therefore not shown.

However, auto-calibrating kt-SENSE reconstructions reveal temporal filtering and signal nulls caused by the  $DC_{und, cart}$  used for the calculation of the coil sensitivities [60], as illustrated in Figure 5.3.3. In contrast, auto-calibrating kt-SENSE reconstructions of undersampled radial data lead to randomly distributed noise-like artifacts and signals at all temporal frequencies were mostly recovered [70].

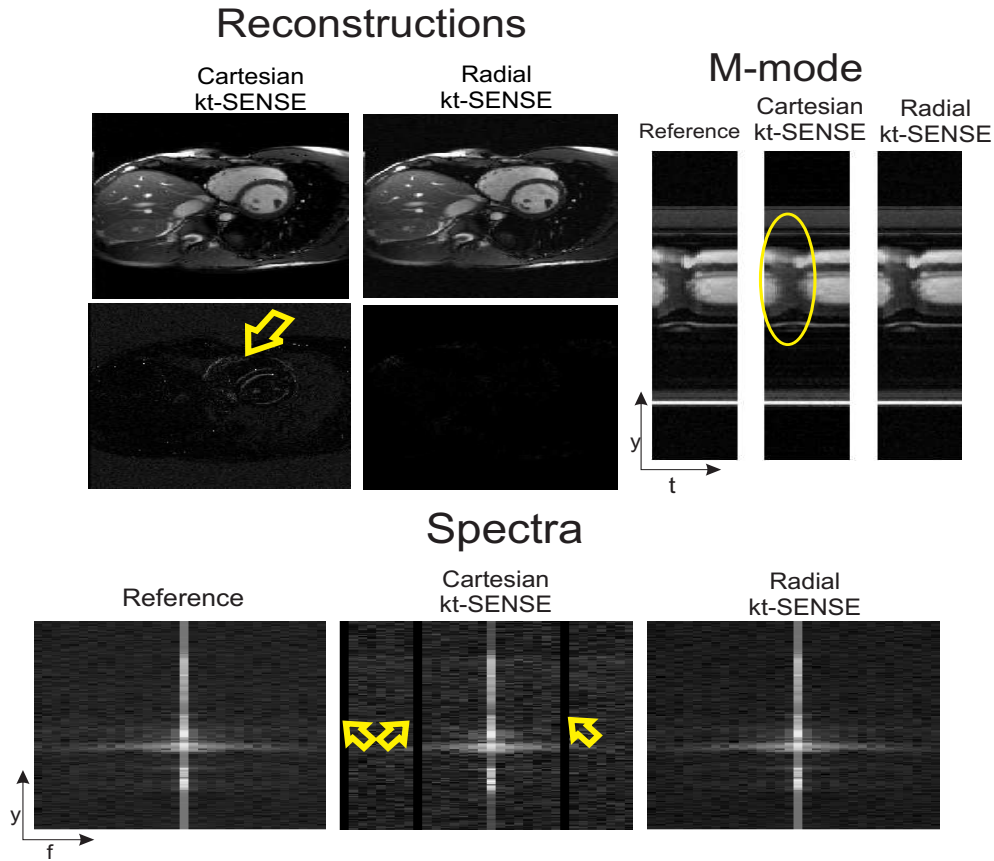


Figure 5.3.3.: Auto-calibrating kt-SENSE reconstructions for Cartesian and radial undersampled data ( $R = 4$ ) with coil sensitivity maps estimated by  $DC_{und, cart}$  and  $DC_{und, rad}$  respectively. The arrow in the difference image is pointing out temporal filtering caused by the use of  $DC_{und, cart}$  in the auto-calibrating algorithm. Aliased components in  $DC_{und, cart}$  images lead to the temporal blurring enclosed within the yellow oval at M-mode graphics. Furthermore, signal nulls in the spectrum of the auto-calibrating kt-SENSE for Cartesian data are marked with small arrows.

### 5.3.2.2. Effect of Spatial Filter

The accelerated Cartesian in-vivo data set was reconstructed utilizing the auto-calibrating kt-SENSE algorithm. Coil sensitivities for the auto-calibration were estimated with the temporal integration of the undersampled data set ( $DC_{und, cart}$ ) and the filtered temporal average employing GRAPPA weights ( $DC_{und, cart - filt}$ ). The difference between both terms is shown in Figure 5.3.4. In this example, artifacts at static regions in the image are

stronger than the errors of dynamic components.

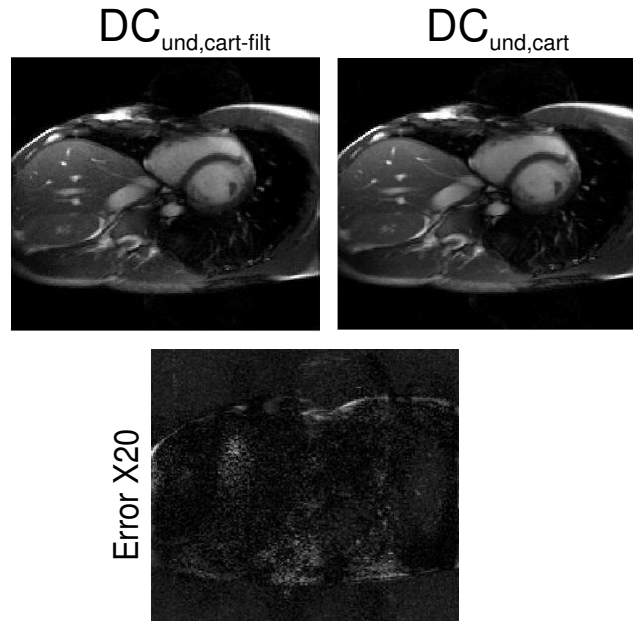


Figure 5.3.4.: DC terms obtained by the temporal integration of the temporal interleaved undersampled data with ( $DC_{und, cart-filt}$ ) and without ( $DC_{und, cart}$ ) spatial filter.

Although the aliased components artifacts cannot be detected in visual inspection in the unfiltered  $DC_{und, cart}$  terms, the blurring in the reconstructed images is evident in the M-mode image. Additionally, signal nulls indicate the presence of higher temporal filtering in the reconstructions using the unfiltered  $DC_{und, cart}$ . Figure 5.3.5 illustrates this phenomena.



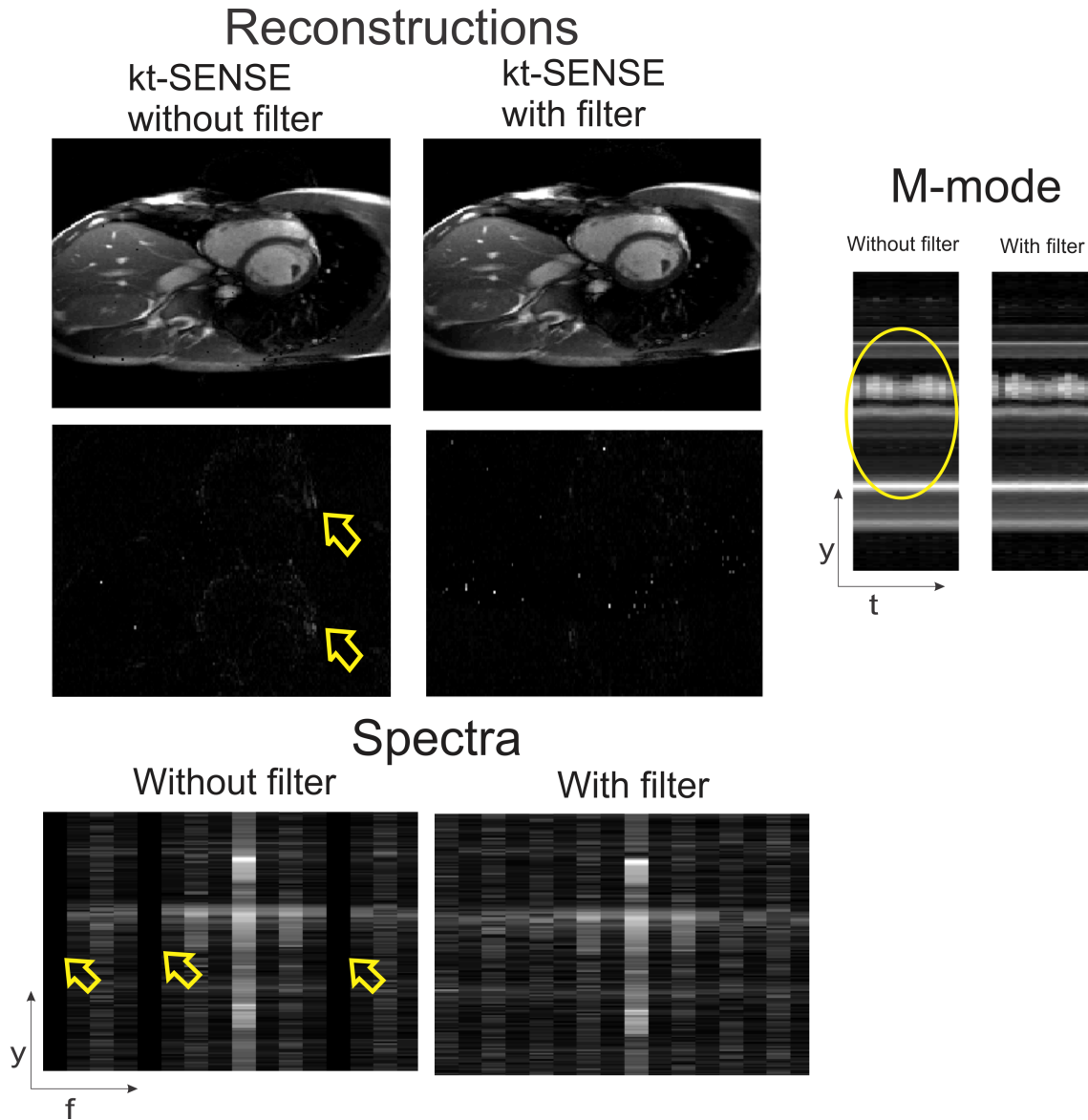


Figure 5.3.5.: One frame of auto-calibrating kt-SENSE reconstructions using a non-filtered and a filtered  $DC$  component. Blurring and signal nulls can be observed in the reconstructions using the non-filtered  $DC$  term.

Furthermore, the reconstructions employing unfiltered  $DC_{und,card}$  present strong artifacts due to aliased components, marked with the arrows in difference images.

### 5.3.2.3. Radial In-vivo data

A fully sampled radial in-vivo data set was retrospectively undersampled by a factor of 4 in a temporal interleaved fashion. Its  $DC$  image was compared to the  $DC$  of the full resolution data ( $DC_{true}$ ), as depicted in Figure 5.3.6. Apparently, the  $DC_{und,rad}$  does not present significant artifacts caused by the aliased components.



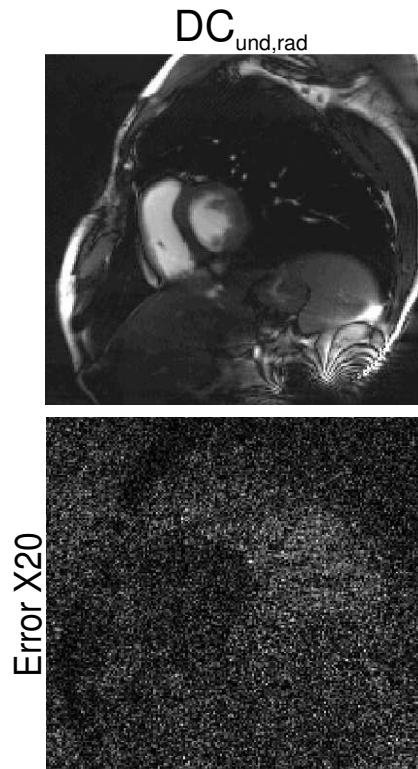


Figure 5.3.6.: DC's of the in-vivo fully radial acquired data and the temporal interleaved undersampled data set. The difference between both terms is also shown below the images.

Errors in the difference image have noise-like character. Consequently, the absence of signal nulls and the insignificant temporal filtering in the reconstructed radial images shown in Figure 5.3.7 stand out.

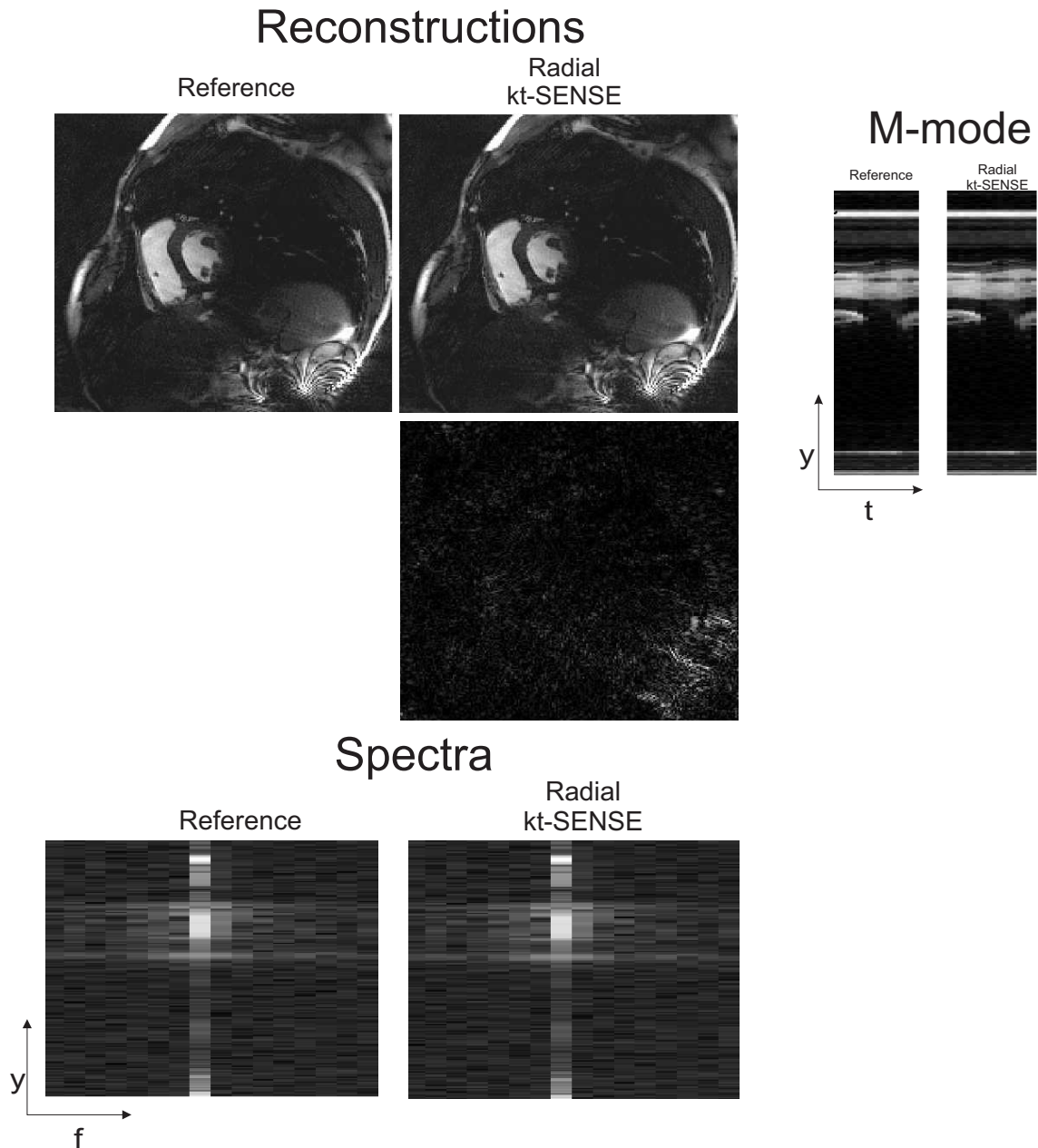


Figure 5.3.7.: A sample frame of auto-calibrating kt-SENSE reconstructions of radial data. Additionally the M-mode and the spectra of the reference and reconstructed data are provided.

In this example, there is no evidence of temporal filtering effects in either the spectra or the M-mode signal of the reconstructed data.

## 5.4. Discussion and Conclusion

In this chapter, it has been demonstrated that the temporal average of undersampled dynamic data is affected by aliasing artifacts. Consequently, coil sensitivity maps esti-

mated from these data exhibit errors. Using these coil sensitivities in auto-calibrating methods may cause signal cancellation in the reconstructed data. In Cartesian auto-calibrating kt-SENSE reconstructions due to an inaccurate inversion of the coil sensitivity matrix, signals at certain temporal frequencies may not be recovered. This lack of temporal frequency components may lead to temporal blurring in the reconstructed images.

In this work, auto-calibrating kt-SENSE reconstructions, where the required coil-sensitivity information is obtained from the temporal average of the undersampled data itself, were performed. The temporal average of undersampled simulated data exhibits aliasing artifacts, that are easily detected. It should be stated, however, that similar artifacts could not be observed in some in-vivo experiments. This can be explained by the sharpness of edges in simulated images, which were not present in in-vivo images where the transitions between the structures in the object are smoother. Nonetheless, signal nulls in reconstructed images are presented in both in-vivo and simulated experiments using  $DC_{und, cart}$  for the calculation of coil sensitivity maps.

In order to improve the SNR of reconstructed data, some reconstruction techniques based on the original kt-SENSE algorithm subtract the temporal average of the undersampled data. The subtraction of the temporal average calculated of the undersampled data leads to a loss of some temporal frequencies in reconstructed images, which can not be recovered as demonstrated in Blaimer et al. [60].

In all these cases, reconstructions with moderate acceleration factor show loss of signal at few temporal frequencies and therefore moderate temporal filtering. However, the main challenge may arise in the case of higher acceleration factors due to the lack of multiple temporal frequency signals. It could be a severe problem for quantification or segmentation of clinical cardiac images.

To reduce aliasing artifacts in the DC image, a spatial GRAPPA filter can be applied, as proposed in [60]. The main purpose of filtering  $DC_{und, cart}$  is to obtain a closer approximation of  $DC_{true}$  by partially removing the aliasing components from  $DC_{und, cart}$  images. This simple additional step allows the recovery of all temporal frequencies in kt-SENSE reconstructed images.

Another possibility to prevent temporal filtering effects is to use acquisition strategies with less severe aliasing artifacts. This has been shown here for radial sampling, where aliasing artifacts in the DC have incoherent characteristics. Consequently, no significant temporal filtering could be observed in auto-calibrating kt-SENSE reconstructions of radial data. The same behavior is expected for other non-Cartesian acquisition strategies (e.g. spiral, rosette, among others).

Here, simulated and in-vivo data were employed to demonstrate the incoherence of the aliasing artifacts in DC images of interleaved undersampled radial data. As it can be observed in Figures 5.3.1 and 5.3.6, the aliasing artifacts of the DC of undersampled radial data ( $DC_{und, rad}$ ) have noise-like appearance. This leads to a closer approximation of  $DC_{true}$  and therefore more accurate coil sensitivity maps. The use of  $DC_{und, rad}$  in the auto-calibrating process of kt-SENSE does not seem to introduce signal cancellation at

any temporal frequency.

It was proved that in order to reduce temporal filtering in the reconstructed data using auto-calibrating kt-SENSE, a radial acquisition strategy can be employed. Due to the incoherence of its aliasing artifacts superposition in the temporal average of the under-sampled data is negligible and consequently the estimation of coil sensitivity maps more accurate.



## Auto-calibrating kt-SENSE

To accelerate dynamic imaging, data are often only partially acquired. To obtain aliasing-free images with diagnostic value, different reconstruction methods have been developed that use a wide range of different mechanism. Typically, a temporal image series exhibits considerable spatial and temporal correlations between frames. This property is used by various reconstruction techniques in order to successfully recover the missing information.

In dynamic imaging, auto-calibrating reconstruction techniques, such as TSENSE [13], Auto-SENSE [57], TGRAPPA [14], require time-interleaved acquisition schemes [71]. These schemes have the advantage, that a full *FOV* reference image with full resolution can be obtained by temporal integration of the subsampled data. In some cases, the reference image is utilized to extract coil sensitivity information if the coil configuration experiences only insignificant changes during the acquisition.

Reconstruction methods such as kt-SENSE [15] exploit not only coil sensitivity variations but also spatio-temporal correlations in order to separate the aliased signals. A priori information about spatio-temporal correlations is obtained from a training data set, which consists of several central k-space lines acquired in a separate scan prior to or embedded in between the subsampled data acquisition as discussed in Chapter 4. A separated training data scan may lead to misregistration due to patient motion or may have different contrast, for example due to administration of contrast agent. An acquisition of training data embedded into the actual scan can for example be achieved by using a variable-density (VD) acquisition scheme [10]. Any of those cases leads to an increased total acquisition time. Furthermore, the quality of training data influences the resulting reconstructed images [72]. It has been demonstrated that training data of limited spatial resolution may cause undesired temporal filtering effects [72]. As described by Vitanis et. al. [73, 74], parallel imaging can be used to increase the spatial resolution of training data. However, the achievable acceleration is still restricted by the time required to obtain extra training lines.

In this work an auto-calibration approach for kt-SENSE is proposed [75]. Our approach is based on feedback regularization [17]. To obtain the training data necessary for kt-SENSE, a TSENSE [13] reconstruction is applied to subsampled data. The resulting

training data set has full spatial and temporal resolution. Notice that there is no need for acquisition of extra training lines in addition to the undersampled scan. In this auto-calibration method, the training data are obtained from the undersampled data set itself.

Images reconstructed with the proposed method are compared to conventional kt-SENSE reconstructions. Temporal filtering effects are quantified by Modulation Transfer Functions (MTFs) [64]. Additionally, noise characteristics are investigated by means of Monte-Carlo simulations. It can be shown, that the temporal fidelity of auto-calibrating kt-SENSE reconstructions is improved when compared to standard kt-SENSE reconstructions.

## 6.1. Theory

### 6.1.1. Auto-calibrating kt-SENSE

In auto-calibrating kt-SENSE, reference images with high spatio-temporal resolution are generated to be used as training data for kt-SENSE reconstructions. To avoid compromising acquisition time, these reference images are estimated directly from the sub-sampled data set itself.

Auto-calibrating kt-SENSE consists of three stages (see Figure 6.1.1):

1. Calculation of the coil sensitivities using the filtered temporal average of undersampled data.
2. Training data estimation using TSENSE.
3. Final reconstructions with conventional kt-SENSE.

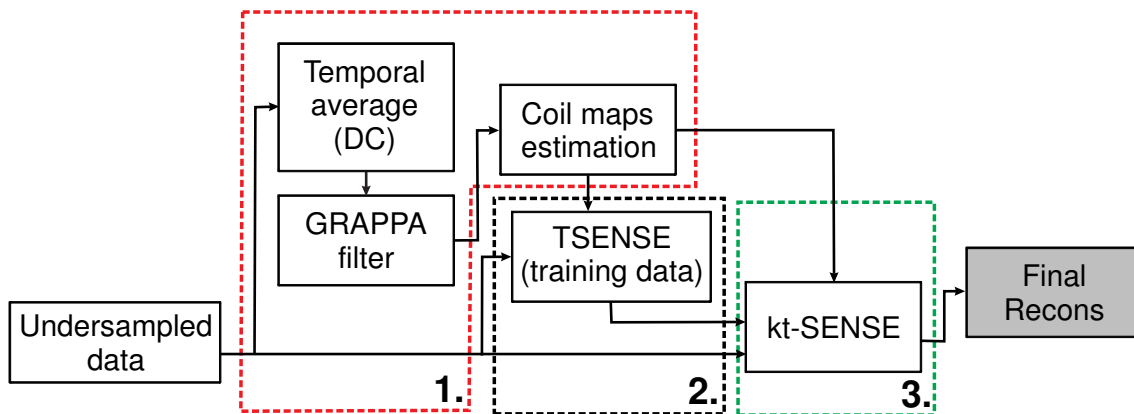


Figure 6.1.1.: Auto-calibrating kt-SENSE reconstruction process in three steps: 1. Coil maps are estimated. 2. TSENSE is used to generate the training data. 3. Conventional kt-SENSE is applied to get the final images.

#### 1. Calculation of the coil sensitivities using a rectified temporal average

A temporally interleaved sampling pattern allows the generation of a fully sampled im-

age by the integrating the subsampled data over the time. The resulting image is the temporal average known as direct current component (DC). The DC image contains the stationary information of the dynamic image series and it is located at zero temporal frequency. Stationary objects in the image contribute only to the DC term. The DC obtained from the subsampled data ( $DC_{und}$ ) and the DC obtained from fully sampled data ( $DC_{true}$ ) are different because non-stationary components lead to aliasing artifacts [60] as mentioned in the previous chapter. To estimate an aliasing-free DC image, a GRAPPA filter is applied to the  $DC_{und}$  signal [60]. Subsequently, coil sensitivity maps are extracted from the filtered image.

## 2. Training data estimation using TSENSE

The coil sensitivity maps from step 1 are used for TSENSE [13] reconstructions of the subsampled data set. The resulting images are used as training data for the kt-SENSE reconstruction. In contrast to training data used in conventional kt-SENSE, these images have full spatial and temporal resolution.

## 3. Final images with conventional kt-SENSE

The coil sensitivity maps calculated in step 1 and the training data from the step 2 are used to obtain the final kt-SENSE reconstructions, as described in Chapter 4.

# 6.2. Methods

## 6.2.1. Evaluation: Modulation Transfer Function (MTF) and Noise Amplification

The performance of conventional and auto-calibrating kt-SENSE are evaluated using the modulation transfer function (MTF) [64]. For dynamic MRI applications, the MTF describes the relation between the true signal  $M_{true}$  and the reconstructed signal  $M_{recon}$  at a given temporal frequency  $f$ :

$$MTF(f) = \frac{M_{recon}(f)}{M_{true}(f)}$$

It therefore is a quantitative measure for temporal filtering effects caused by the reconstruction algorithms. In general, the true object and the reconstructed image are related by:

$$\hat{\rho} = H\rho + \hat{\eta} \quad (6.2.1)$$

where  $\hat{\rho}$  is the reconstructed data expressed in  $(k_x, k_y, f)$  domain,  $\rho$  the truth data in same domain,  $H$  represents the combined data acquisition and reconstruction process and  $\hat{\eta}$  is noise present in the data. Now, consider a pixel of the reconstructed image:

$$\hat{\rho}_i = H_{ii}\rho_{ii} + \sum_{j \neq i} H_{ij}\rho_j + \hat{\eta}_i \quad (6.2.2)$$

where  $H_{ii}$  are the coefficients of the MTF and the off-diagonal terms  $H_{ij}$  represent resid-

ual aliasing. The relation  $H$  between the true signal ( $M_{true}$ ) and the reconstructed signal ( $M_{recon}$ ) is unknown in equation 6.2.1. In order to calculate the MTF of the reconstruction method, a perturbation approach is used as proposed in reference [64]. To that end, several perturbations ( $P_p$ ) are added to the true signal ( $\rho$ ), resulting in disturbed data  $\rho_p$ . The resulting disturbed signal or “new” true signal is then subsampled and reconstructed to yield the final signal ( $\hat{\rho}_p$ ). The reconstructed signal ( $\hat{\rho}_p$ ) are plotted versus the values of disturbed data ( $\rho_p$ ) at each temporal frequency. This process is repeated with different linearly increasing perturbations. As illustrated in Figure 6.2.1, the slope of the fit to these points ( $\rho_p, \hat{\rho}_p$ ) represents the MTF. A perfect reconstruction will have a slope of 1, meaning that no temporal filtering is present in the reconstructed data, i.e.  $M_{recon}(f) = M_{true}(f)$ . Slopes smaller than 1 correspond to temporal filtering, because the signal at this temporal frequency is suppressed by the reconstruction.

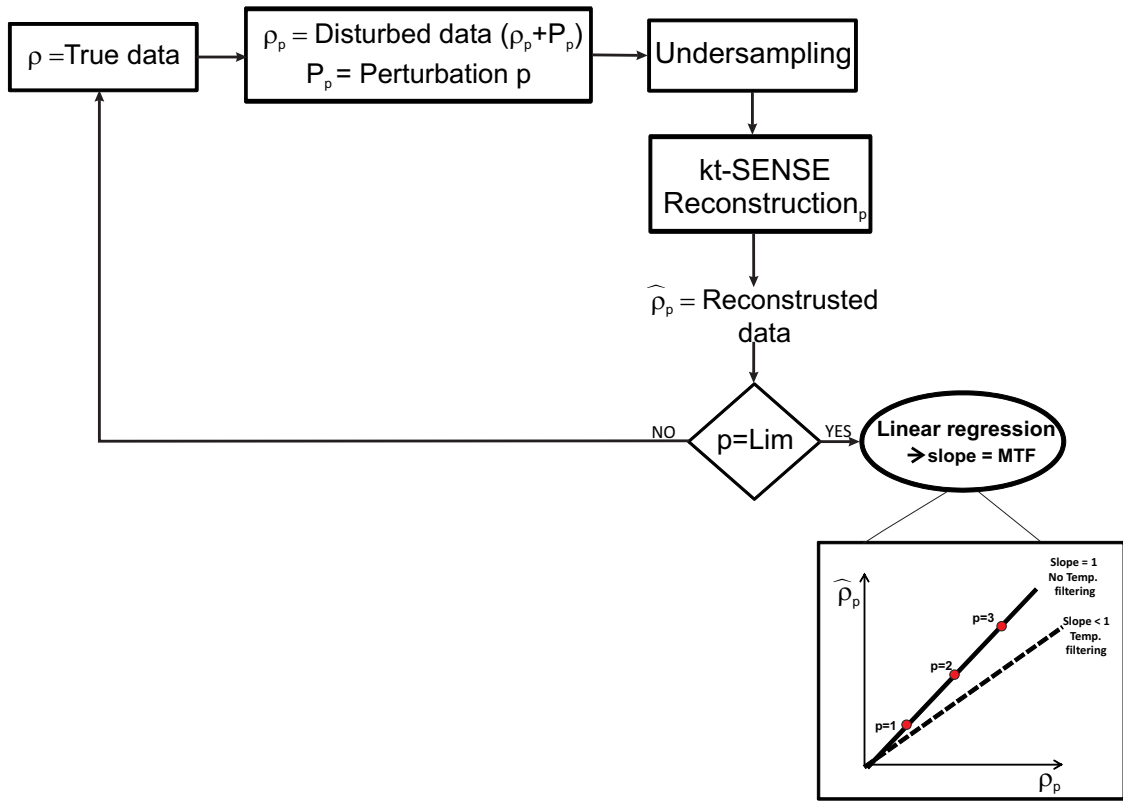


Figure 6.2.1.: This Figure illustrates the MTF calculation process based on the perturbation approach. The relation between reconstructed ( $\hat{\rho}_p$ ) and disturbed ( $\rho_p$ ) points at each temporal frequency is linear and the slope of the graphic represents the MTF at each temporal frequency point.

In addition to temporal filtering effects, the noise level introduced by both reconstruction methods was evaluated using Monte-Carlo simulations. To that end, the acquired data were replaced by complex Gaussian random numbers. The data set was subsampled and reconstructed using parameters from the actual reconstruction. This process was repeated n-fold for different noise data and its variance was calculated. The ratio



between the variances of these reconstructions  $\hat{\rho}_R$  and the reconstructions of the fully sampled data  $\hat{\rho}_1$  gives the noise amplification of the reconstructed data:

$$N(k_y, f) = \sqrt{\frac{\sum_{k_x} \text{var}\{\hat{\rho}_R(k_x, k_y, f)\}}{\sum_{k_x} \text{var}\{\hat{\rho}_1(k_x, k_y, f)\}}} \quad (6.2.3)$$

The 2-D MTF's were calculated for conventional and auto-calibrating kt-SENSE as described in reference [64]. Because the MTF's exhibit only small variations along this dimension, the  $k_y$ -direction was averaged before displaying the data. Additionally, the noise amplification of the reconstructions was compared.

## 6.2.2. Simulations

Image reconstructions of both simulated and in-vivo data were performed off-line using the MATLAB (Mathworks, Natick, MA, USA) programming environment.

The numerical model shown in Figure 6.2.2 was used to obtain simulated data. The simulated data with a matrix size of  $100 \times 100$  were multiplied by coil sensitivity maps obtained by Biot-Savart calculations. Complex Gaussian noise was added to each channel and the noisy simulated data were retrospectively subsampled by a factor of  $R = 5$  shifting the sampling pattern by one phase encoding line for subsequent frames. Reconstructions were performed using auto-calibrating and conventional kt-SENSE. Low resolution (21 central k-space lines) and full resolution images were chosen as training data sets for conventional kt-SENSE. For cardiac applications, the recommended amount of reference training data lines is at least 10 for sufficient reconstruction quality without compromising the temporal resolution of the acquired data [72]. The used number of 21 k-space central lines is relatively high for conventional kt-SENSE. However, the goal is to demonstrate that using training data with a resolution lower than the base resolution of the acquired data may introduce temporal filtering.

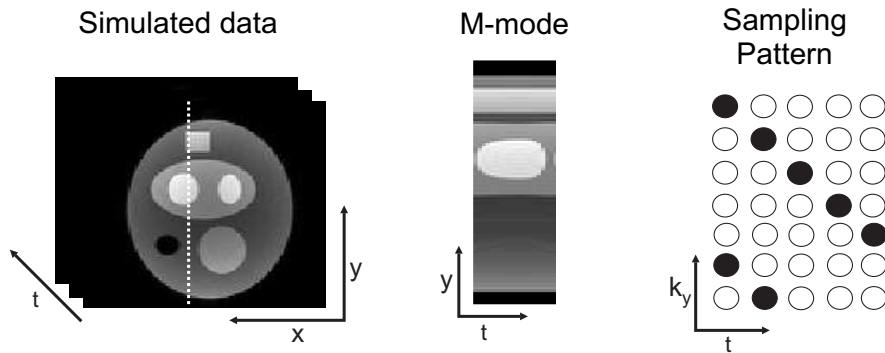


Figure 6.2.2.: Numerical model, provided by Malik S. (King's College London, United Kingdom), used for producing synthetic images. The temporal evolution of the points along the dashed line are shown in the middle. This representation is also known as M-mode. On the right hand side, the sampling pattern ( $R = 5$ ) is shown.

### 6.2.3. In-vivo Measurements

In-vivo data of healthy volunteers were acquired on a 1.5T whole body scanner (Siemens Medical Solutions, Erlangen, Germany). All subjects gave informed consent according to the institutional policy. The data were provided by Peter Kellman (National Institutes of Health, Bethesda US).

In order to demonstrate the feasibility of the auto-calibration approach for kt-SENSE, 32 time frames of in-vivo prospectively gated segmented cardiac CINE experiments were acquired with a 32 channel receiver array using a bSSFP sequence with parameters: TE = 1.4 ms, TR = 2.8 ms, flip angle = 50°, a matrix size of 192 x 150 and a Field of View (FOV) of 350 x 263 mm<sup>2</sup>. The data were retrospectively subsampled to an acceleration factor of 5 using the same sampling pattern that was previously used in the simulations. Both conventional and auto-calibrating kt-SENSE reconstructions were performed. Conventional kt-SENSE reconstructions were carried out using training data sets with low (21 central k-space lines) and full resolution.

Both, simulated and in-vivo data were reconstructed using conventional and auto-calibrating kt-SENSE with three values of the regularization parameter  $\lambda$  (see equation 4.4.1), in order to investigate the temporal filtering connected to different levels of regularization.

In addition, real time free-breathing data were acquired with a 8 channel receiver array using a bSSFP sequence with parameters: acceleration factor 4 with a Cartesian interleaved sampling scheme, TE = 1.3 ms, TR = 2.7 ms, flip angle = 50°, 32 time frames, a matrix size of 92 x 192 and FOV of 350 x 263 mm<sup>2</sup>. No additional training data was obtained. A second data set was acquired with a 32 channel receiver coil and 8-fold acceleration. Due to the lack of training data, only auto-calibrating kt-SENSE could be applied in order to reconstruct these data sets. For comparison, TSENSE reconstructions were applied in both cases.

All reconstructions were performed off-line using the MATLAB (Mathworks, Natick, MA, USA) programming environment.

## 6.3. Results

### 6.3.1. Simulations

The MTF's of auto-calibrating and conventional kt-SENSE reconstructions of synthetic data ( $R = 5$ ) with three different degrees of regularization are shown in Figure 6.3.1. Mild, medium and strong regularization degrees were combined with training data of low and full resolution as well as full resolution training data obtained via auto-calibration. Different degrees of temporal filtering in the reconstructed kt-SENSE images can be observed. The red curve in Figure 6.3.1 depicts the MTF of auto-calibrating kt-SENSE, the blue and discontinuous black curves represent the MTF of conventional kt-SENSE using training data with low and full resolution respectively.

## Modulation Transform Function (MTF)

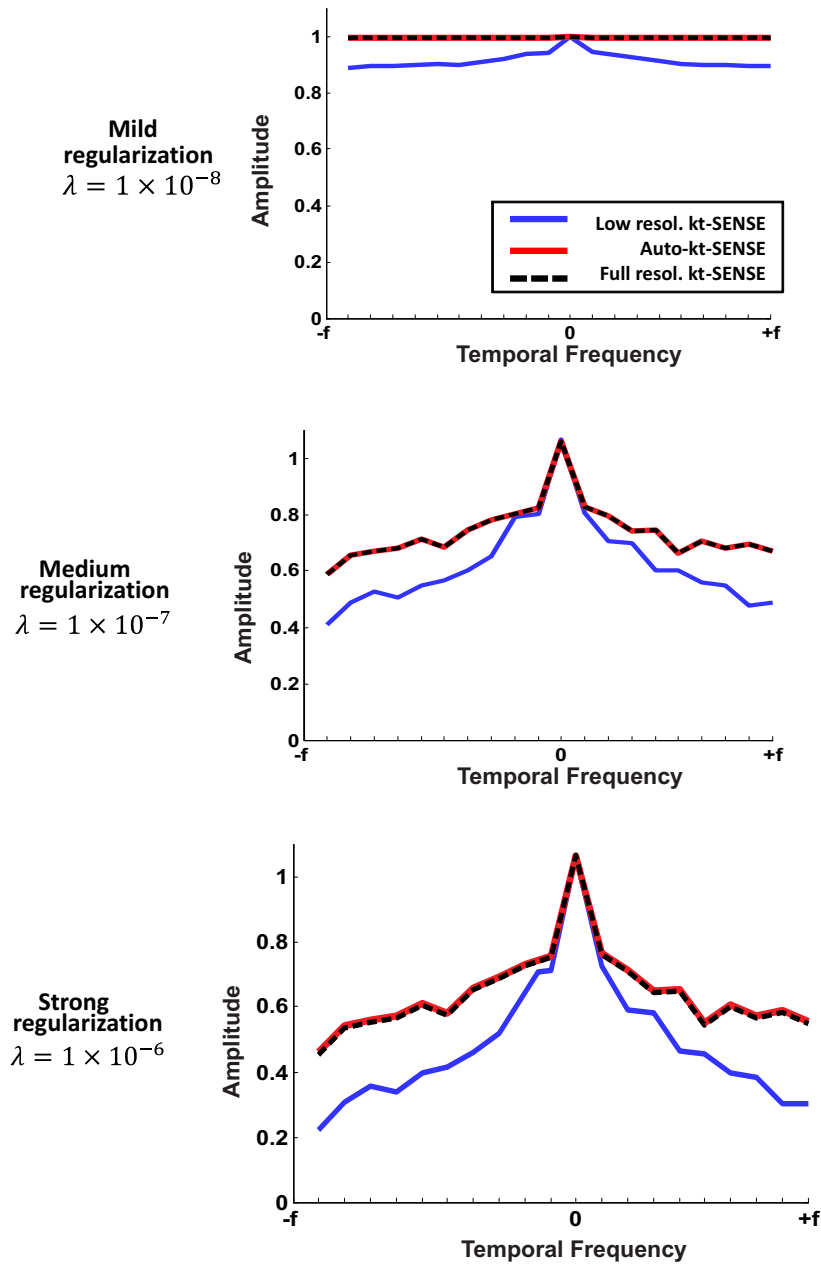


Figure 6.3.1.: MTF's of conventional kt-SENSE reconstructions of simulated data ( $R = 5$ ) using full resolution training data (dashed black line), low resolution training data (blue line) and MTF's of auto-calibrating kt-SENSE reconstructions (red line) with mild, medium and strong regularization values.

Confirming the hypothesis of this work, the MTF's of conventional kt-SENSE with low resolution training data show more attenuation at frequencies outside the DC term, implying higher filtering even for small values of the regularization parameter. Note

that the auto-calibrating kt-SENSE reconstructions show a similar behavior in terms of temporal filtering as conventional kt-SENSE with full resolution training data. A representative frame reconstructed with auto-calibrating and conventional kt-SENSE using a mild regularization are shown to illustrate the blurring effect corresponding to temporal filtering (see Figure 6.3.2a). The arrows in Figure 6.3.2a point to blurring produced by conventional kt-SENSE due to the low spatial resolution of the training data in regions of motion with high frequencies. Figure 6.3.2b shows the noise amplification for each reconstruction method.

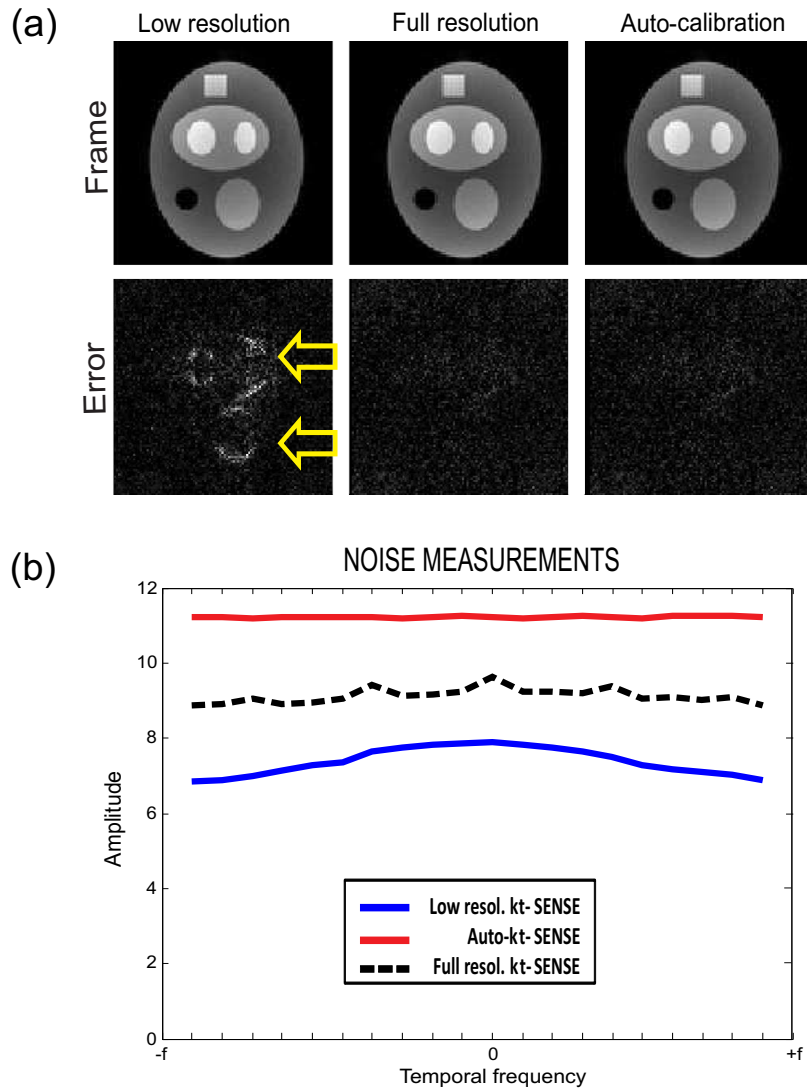


Figure 6.3.2.: Representative reconstructed frame and noise measurements choosing a mild regularization parameter. (a) Exemplary image of  $R = 5$  subsampled data with moderate noise level reconstructed with: conventional kt-SENSE employing low resolution (first column), full resolution training data (second column) and auto-calibrating kt-SENSE (third column). (b) Errors with respect to the reference data are depicted below. The respective noise measurements.

Compared to conventional kt-SENSE with full resolution training data, auto-calibrating kt-SENSE reconstructions have a reduced SNR. Noise amplification in the reconstructed images increases when adding higher noise levels to the simulated data, as demonstrated in Figure 6.3.3.

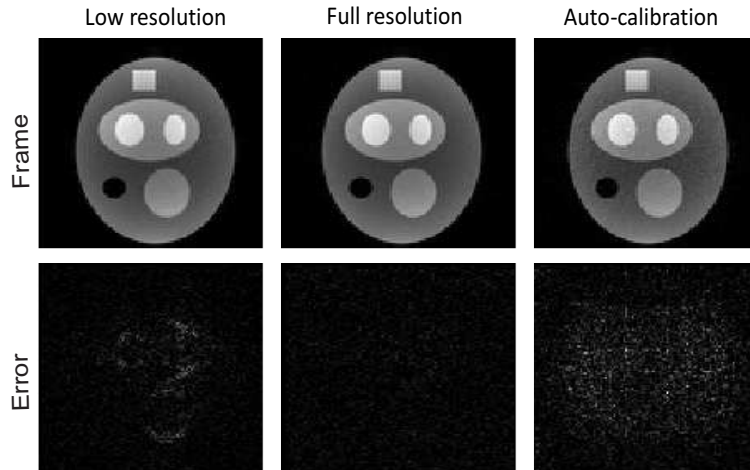


Figure 6.3.3.: Exemplary frame of reconstructions of accelerated data ( $R = 5$ ) with higher noise level. Shown are results from conventional kt-SENSE reconstructed data using low resolution (left column), full resolution training data (middle) and auto-calibrating kt-SENSE (right column). The error with respect to the reference are depicted below.

It has been demonstrated in [72] that the quality of training data in the kt-SENSE method influences the final reconstructions. This can also be observed in the auto-calibrating kt-SENSE reconstructions, where the SNR is affected by noise amplification in the training data caused by the TSENSE reconstruction.

### 6.3.2. In-vivo Measurements

#### Breath hold CINE Experiment

Accelerated in-vivo data were reconstructed with auto-calibrating and conventional kt-SENSE using different amount of regularization. In Figure 6.3.4, MTF's of auto-calibrating and conventional kt-SENSE reconstructions are depicted using mild, medium and strong regularization. Again, reconstructions employing conventional kt-SENSE with low resolution training data yield the highest temporal filtering (i.e. strongest attenuation of higher temporal frequencies). The MTF's of in-vivo data exhibit similar behavior as the MTF's of simulated data.

### Modulation Transform Function (MTF)

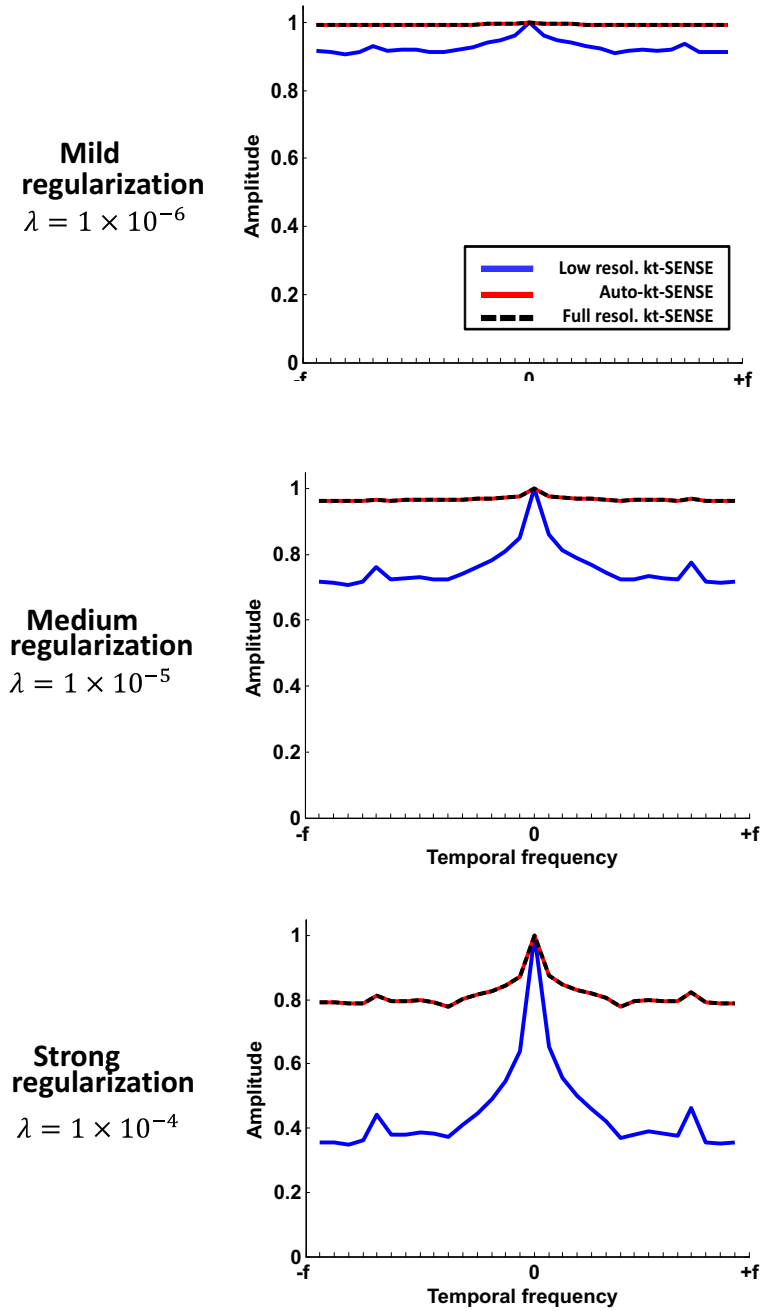


Figure 6.3.4.: Reconstructions of accelerated in-vivo data ( $R = 5$ ) using conventional kt-SENSE with full resolution (dashed black line), low resolution (blue line) training data and using auto-calibrating kt-SENSE (red line). In each case, three different lambda values were employed.

In Figure 6.3.5a, reconstructed images with auto-calibrating and conventional kt-SENSE using a mild regularization are displayed. In these reconstructions, the spatial blurring is more evident, which can also be observed in the M-mode plot (yellow oval). The

arrow points out the artifacts in the difference image produced by the use of low resolution training data in conventional kt-SENSE. The myocardium appears sharper in auto-calibrating kt-SENSE and full resolution conventional kt-SENSE reconstructions.

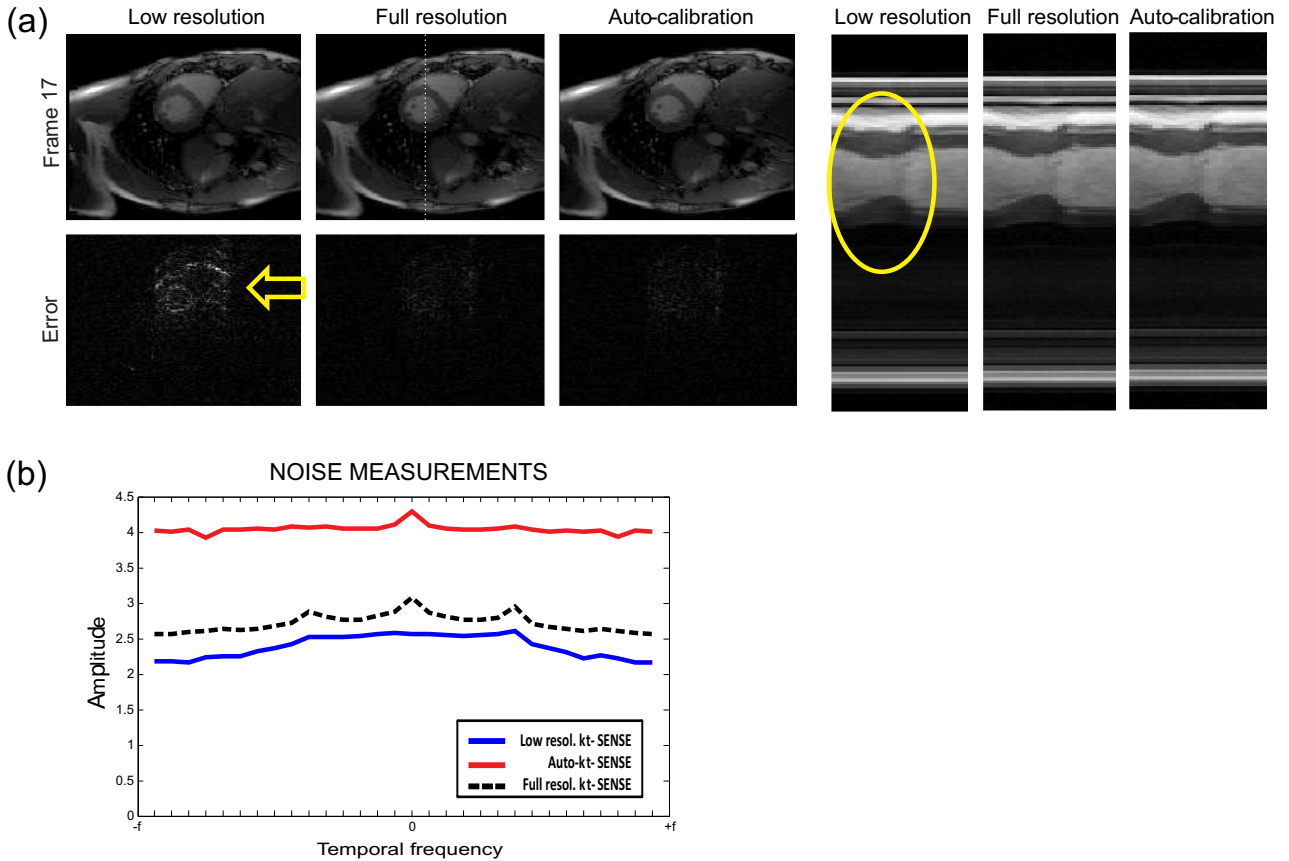


Figure 6.3.5.: (a) Representative reconstructed frame of undersampled data ( $R=5$ ) using mild regularization with conventional kt-SENSE employing low resolution (left column), full resolution training data (middle) and using auto-calibrating kt-SENSE (right column). (b) Errors with respect to the reference data are shown below each reconstruction. The M-mode plotted along the white line in image domain is also illustrated. Noise measurements for each reconstruction.

Noise measurements of both conventional and auto-calibrating kt-SENSE reconstructions were calculated and are illustrated in Figure 6.3.5b. Auto-calibrating kt-SENSE reconstruction algorithm exhibit a lower SNR in the final images when compared to conventional kt-SENSE, very similar to the behavior observed in the simulations.

### Free Breathing Experiments

In order to validate auto-calibrating kt-SENSE, in-vivo free breathing experiments are presented. Auto-calibrating kt-SENSE and TSENSE reconstructions of free-breathing accelerated ( $R = 4$  and  $R = 8$ ) data are shown in Figure 6.3.6 and 6.3.7 respectively. Auto-calibrating kt-SENSE reconstructions exhibit improvement SNR when compared

to TSENSE images. In contrast to kt-SENSE, a TSENSE reconstruction does not introduce temporal filtering. Comparing the M-mode of both TSENSE and auto-calibrating kt-SENSE reconstructions reveals the high temporal fidelity and the lack of visible temporal filtering using the auto-calibrating approach. Due to the lack of training data, no conventional kt-SENSE reconstruction could not be carried out.

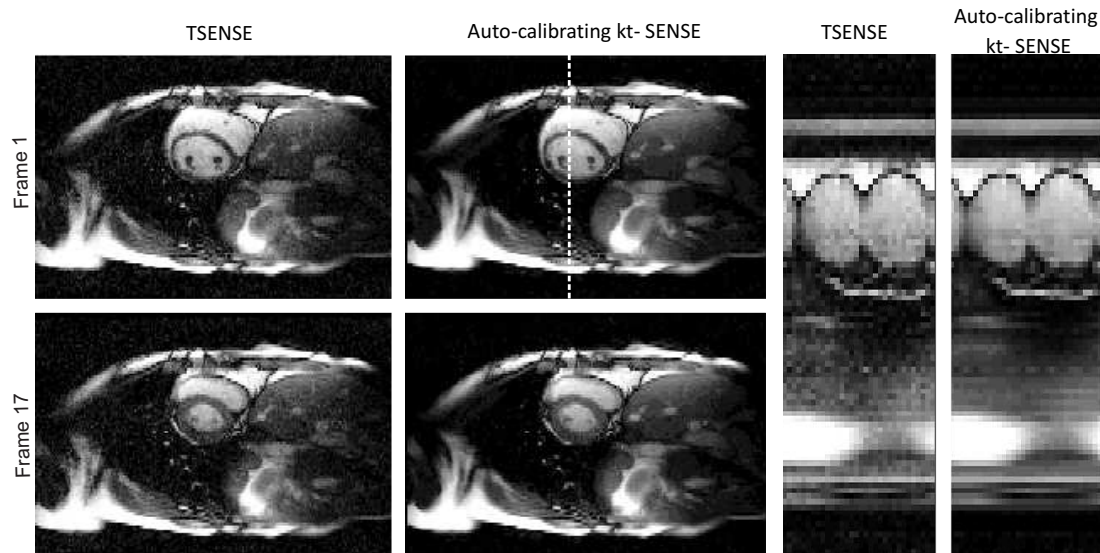


Figure 6.3.6.: In-vivo free-breathing experiments (acceleration factor  $R = 4$ ) without acquisition of training lines. Two frames from different stages of the cardiac cycle are presented, reconstructed with TSENSE and auto-calibrating kt-SENSE. Additionally, the M-mode is plotted along the white line.



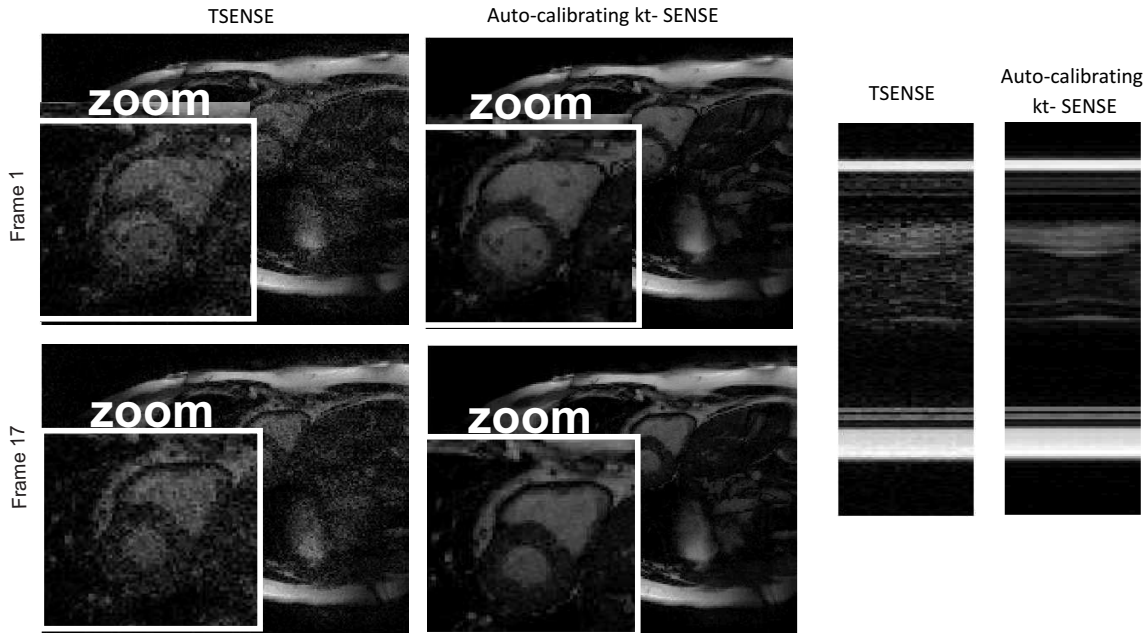


Figure 6.3.7.: In-vivo experiments (acceleration factor  $R = 8$ ) without acquisition of training data. Two exemplary frames from different stages of the cardiac cycle are shown, reconstructed with both TSENSE and auto-calibrating kt-SENSE. The M-mode is also displayed.

## 6.4. Discussion and Conclusions

For kt-SENSE reconstructions, the training data set plays an important role since it is used for the estimation of missing data. Motion artifacts or any other inconsistency between subsampled and training data lead to deviations of reconstructed data from the optimal solution. Besides consistency of the data, the spatial and temporal resolution of the training data influences the quality in kt-SENSE reconstructions. Using training data with a higher spatial resolution avoids strong temporal filtering effects.

Here, we presented an auto-calibration approach for kt-SENSE based on feedback regularization. The training data are obtained from the accelerated data itself by an additional TSENSE reconstruction prior to the final kt-SENSE reconstruction. The sensitivity maps required for a TSENSE reconstruction can be obtained by temporal integration of the undersampled data. To remove aliasing artifacts and to prevent possible temporal filtering effects, a GRAPPA filter is applied to the temporal average as discussed in the previous chapter. The auto-calibrating process produces training data with full spatial resolution and therefore minimizes the temporal filtering that affects the reconstructed images. Auto-calibrating kt-SENSE does not require a separate training data acquisition, which leads to a higher achievable temporal resolution and an overall reduced acquisition time.

An auto-calibration approach using a TGRAPPA instead of TSENSE to obtain the training data and coil sensitivity maps for the kt-SENSE was proposed in a previous work

[76]. However, reconstructions using TGRAPPA exhibit in lower SNR and affect the noise level of the final kt-SENSE images.

The spatial resolution of the training data used in kt-SENSE has an important impact on the quality of the reconstructed images. By employing MTF functions, the auto-calibrating approach was shown to have the same temporal accuracy as conventional kt-SENSE with a full resolution training data set. Compared to conventional kt-SENSE using low resolution training data (e.g. 21 or less training lines), the auto-calibration approach leads to reduced blurring within reconstructed images.

However, the noise level in auto-calibrating kt-SENSE is higher than in the conventional approach. This can be explained by the noise amplification ( $g$ -factor) in the TSENSE reconstructed images that are used as training data. The higher noise level in the training data is then transferred to the final reconstructed images. The higher noise level was not a problem in the cardiac cine experiments shown here, but might become problematic at very high acceleration factors. However, it should be noted that the effective acceleration factor is higher than in conventional kt-SENSE because no additional training data have to be acquired.

In general, auto-calibrating kt-SENSE provides reconstructions of high accuracy for dynamic imaging applications. Temporal filtering effects are minimized because a training data set with full spatial and temporal resolution is obtained from the subsampled data itself. Since the acquisition of the training data is not necessary in order to perform the reconstruction, the acquisition time will be further reduced. Additionally, the auto-calibrating method is less sensitive to object motion [13] and inconsistencies in data.



## Chapter 7.

# Optimizing MR Relaxometry using kt-PCA

The interest in quantitative MRI (qMRI) has increased over the last decade due to its ability to detect changes in tissue in a quantitative way. This allows for example, the early detection and diagnostic of brain alterations [77]. Specifically, changes of spin-lattice ( $T_1$ ), spin-spin ( $T_2$ ) relaxation times as well as spin density may be an indicator for the presence of lesions or diseases in the brain. Quantification of relaxation parameters (i.e. MR relaxometry) in clinical practice demands high accuracy and reproducibility since they are used for detecting and monitoring diverse diseases, for example multiple sclerosis [78] and Alzheimer's disease [79].

Conventionally, the estimation of MR parameters requires a series of images acquired with different contrasts. In combination with the pauses in between scans that are required for the full recovery of the magnetization, this leads to long acquisition times. In practice, the long scan times required for quantitative MR parameter mapping images restrict its clinical application. New acquisition techniques for MR relaxometry images have been developed in order to shorten acquisition times. Several recent advances in MR sequence design allow the mapping of either just one relaxation parameter [80, 81, 82] or several parameters mapping  $T_1$ ,  $T_2$  and spin density simultaneously in clinically acceptable time [83, 84, 85]. One example is the Inversion Recovery TrueFISP (IR TrueFISP) sequence [85], that allows the simultaneous extraction of  $T_1$ ,  $T_2$  and relative spin density from a single 2-D experiment in one slice. An advantage of this method is automatically registered and perfectly aligned parameter maps.

Additionally, parallel MRI techniques promise a shortened acquisition process as described in the last chapters. Methods such as TSENSE [13], TGRAPPA [14] and kt-SENSE [15] that are routinely used for the reconstruction of dynamic cardiac data, rely on manipulating the artifacts in the temporal frequency domain in order to obtain a maximal separation between the spectra. This mechanism often fails for the reconstruction of undersampled MR relaxometry studies since the images exhibit values at all temporal frequencies and the real and the aliased components cannot be separated.

The recent introduction of kt-PCA [16] for the reconstruction of cardiac images, where the data are expressed in different basis functions based on Principal Component Analysis (PCA), provides a new approach for separating the aliasing artifacts in a different domain. PCA is a mathematical tool that extracts the most important information (based on their relevance) from a data set. The data are converted into linearly uncorrelated variables called principal components (PC). The first and most important principal component has the largest corresponding eigenvalue. The eigenvalues of all succeeding components are lower and less relevant for the representation of the data. The number of principal components needed for an accurate representation of the data can be equal or less than the number of original variables. The smallest components mostly only carry noise or other artifacts inherent to the data. Since relaxometry images typically exhibit a temporal exponential behavior and hence can be described with only few parameters, kt-PCA seems to be good a candidate for reconstruction. Using a relatively low number of principal components may simplify the reconstruction and provide more accurate results.

So far, kt-PCA has been presented for reconstruction of dynamic cardiac data [16]. Here, we propose the application of kt-PCA for accelerated MR relaxometry images [86]. We expect relaxometry images to be highly sparse in the PC domain. The representation of these data with fewer parameters may constrain the reconstruction and lead to improved results. Furthermore, the high degree of redundancy in MR relaxometry data can be advantageous for kt-PCA in order to significantly reduced the required amount of training data. In the following work, parameter MR mapping is investigated exclusively in two dimensions. However, this principle can be easily extended to 3-D imaging.

## 7.1. Theory

### 7.1.1. MR Relaxometry

As described in Chapter 2, after excitation the magnetization vector ( $\vec{M}$ ) precesses around the external magnetic field and relaxes back to its thermal equilibrium along the longitudinal axis. The time constants  $T_1$  and  $T_2$  are connected to the recovery of the longitudinal magnetization and the decoherence of transversal magnetization respectively. Sequences such as FLASH [24] and TrueFISP [87] allow the quantification of  $T_1$  or  $T_1$  and  $T_2$  simultaneously. Here, IR-Snapshot FLASH [88] and IR TrueFISP[85] are utilized for measuring  $T_1$ ,  $T_2$  and spin density ( $M_0$ ) maps in a single acquisition.

#### 7.1.1.1. Segmented IR-Snapshot FLASH

IR-Snapshot FLASH [82] is used for fast acquisition of quantitative  $T_1$  and  $M_0$  maps. A  $rf$  pulse with a flip angle of  $180^\circ$  inverts the magnetization vector from its position  $+M_0$  to  $-M_0$  on the  $z$ -axis. Subsequently, the magnetization recovers towards its thermal equilibrium with the time constant  $T_1$ . During this recovery, IR Snapshot FLASH acquires a set of images at different time points using a train of excitation pulses with small flip angles. This leads to a modified value  $M_0^* < M_0$  for the steady state magnetization.

Because of the fast recovery of the longitudinal relaxation, the k-space of each image needs to be divided into segments in order to obtain the desired temporal resolution as depicted in Figure 7.1.1. After a single inversion, only part of the k-space of each image is acquired and so the experiment has to be repeated multiple times to obtain fully sampled data. Before a new segment is acquired, a delay of about 5-10 s is inserted for complete relaxation of the longitudinal magnetization. As the signal evolution is influenced by the FLASH pulses, a time constant  $T_1^* < T_1$  is obtained. Accordingly, relaxation of the magnetization vector for this sequence can be expressed as:

$$M(t) = M_0^* \cdot [1 - INV \cdot \exp(-\frac{t}{T_1^*})] \quad (7.1.1)$$

where INV and the effective relaxation time  $T_1^*$  are given by:

$$INV = 1 + \frac{M_0}{M_0^*} \quad (7.1.2)$$

$$\frac{1}{T_1^*} = \frac{1}{T_1} - \frac{1}{TR} \cdot \ln(\cos \alpha) \quad (7.1.3)$$

with a very small flip angle  $\alpha$ . The saturation value  $M_0^*$  can be calculated using:

$$M_0^* = M_0 \cdot \frac{1 - \exp(-\frac{TR}{T_1})}{1 - \exp(-\frac{TR}{T_1^*})} \quad (7.1.4)$$

For very short repetition times (TR) ( $TR \ll T_1^*$ ), this can be approximated using a Taylor series, leading to:

$$M_0^* = M_0 \cdot \frac{T_1^*}{T_1} \quad (7.1.5)$$

Finally, the parameters  $T_1$  and  $M_0$  can be obtained by fitting the data to the parameters INV,  $T_1^*$  and  $M_0^*$  of equation 7.1.1:

$$T_1 = T_1^*(INV - 1) \quad (7.1.6)$$

$$M_0 = M_0^* \left( \frac{T_1}{T_1^*} \right) \quad (7.1.7)$$

Here, knowledge of the flip angle is not necessary to successfully fit the data. However, flip angles values higher than  $10^\circ$  produce larger deviations in the results, according to equation 7.1.3.

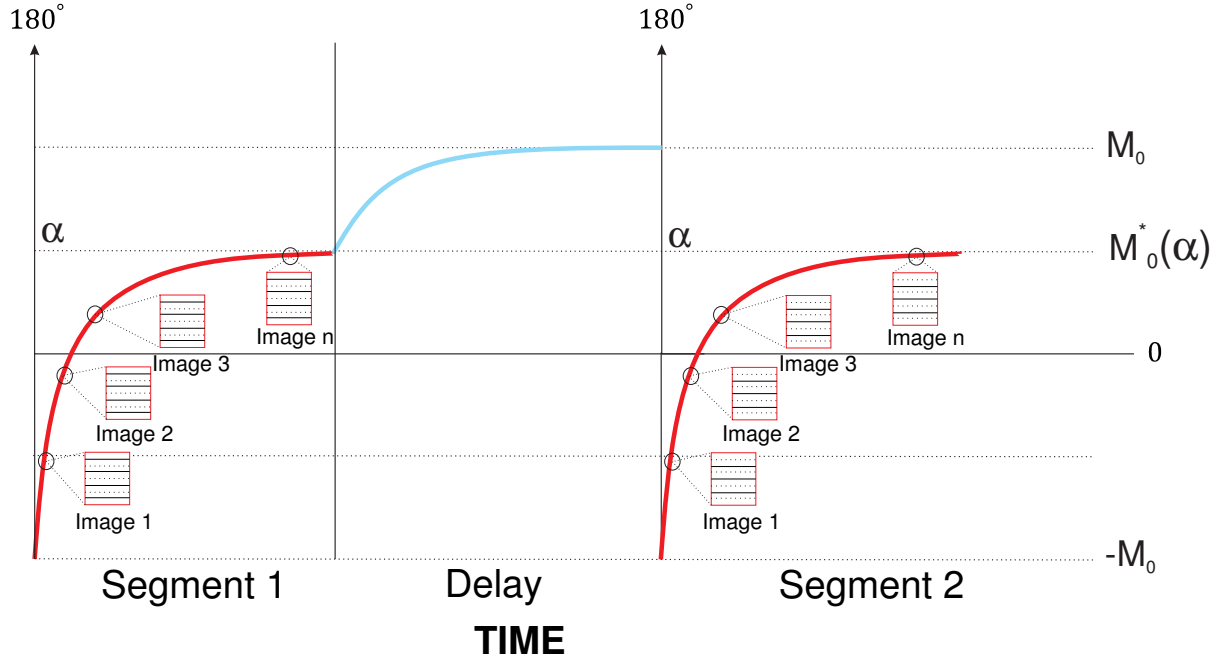


Figure 7.1.1.: The scheme shows the relaxation curves across two segments using a IR-Snapshot FLASH sequence. The time period between both segments represents the delay needed for a fully relaxation of the magnetization vector. Note: this signal evolution is also valid for the IR TrueFISP sequence.

### 7.1.1.2. Segmented IR TrueFISP

$T_1$ ,  $T_2$  and  $M_0$  parameters can be estimated simultaneously utilizing a IR TrueFISP sequence. Following a  $180^\circ$  inversion pulse, the standard TrueFISP sequence [89] is applied for the acquisition of images. Typically, a TrueFISP sequence consists of consecutive excitation pulses with flip angles alternating between  $\alpha$  and  $-\alpha$ . To avoid an intense signal fluctuation at the beginning of the sequence producing image artifacts, a preparation pulse with a flip angle of  $\frac{\alpha}{2}$  precedes the TrueFISP sequence. The IR-TrueFISP signal evolution is analogous to the IR-Snapshot FLASH in Figure 7.1.1.

It has been demonstrated that the parameters  $T_1$ ,  $T_2$  and  $M_0$  can be calculated from the apparent relaxation times ( $T_1^*$ ,  $M_0^*$  and  $INV$ ) obtained from a single IR TrueFISP signal evolution [85]. Analogous to IR-Snapshot FLASH, the signal evolution in IR TrueFISP imaging can be described in good approximation by a three parameter mono-exponential function:

$$M(t) = M_0^* \cdot [1 - INV \cdot \exp(-\frac{t}{T_1^*})] \quad (7.1.8)$$

The values of  $M_0$ ,  $INV$  and  $T_1^*$  can be estimated by a three parameter fit.  $T_1$  and  $T_2$  maps are related to  $INV$ ,  $T_1^*$  and  $M_0^*$  by:

$$INV = 1 + \frac{M_0}{M_0^*} = 1 + \frac{\sin \frac{\alpha}{2}}{\sin \alpha} \left[ \left( \frac{T_1}{T_2} + 1 \right) - \cos \alpha \left( \frac{T_1}{T_2} - 1 \right) \right] \quad (7.1.9)$$

From here,  $T_1$  and  $T_2$  can directly be calculated:

$$T_1 = T_1^* \cdot \cos\left(\frac{\alpha}{2}\right) \cdot (INV - 1) \quad (7.1.10)$$

$$T_2 = T_1^* \cdot \sin^2\left(\frac{\alpha}{2}\right) \cdot \left(1 - \frac{\cos\left(\frac{\alpha}{2}\right)}{INV - 1}\right)^{-1} \quad (7.1.11)$$

and finally the relative spin density ( $M_0$ ) can be expressed by:

$$M_0 = M_0^* \cdot \frac{(INV - 1)}{\sin\frac{\alpha}{2}} \quad (7.1.12)$$

In contrast to IR-FLASH, in this approach the flip angle  $\alpha$  has to be known.

### 7.1.2. Data Reconstruction with kt-PCA

Mathematically, a Principal Component Analysis (see appendix A) of a matrix is a simple basis transform. Hereby, a basis is chosen that exposes useful signal correlations and noise in the data. In dynamic MR applications, PCA can be used to reconstruct images of highly accelerated data. kt-PCA combines PCA and the kt-BLAST/SENSE reconstruction process in order to generalize these approaches [16].

The PCA decomposition of the true data  $\rho_{true}$  in  $y$ - $f$  domain is given by:

$$\rho_{true} = X_{pc}B. \quad (7.1.13)$$

Hereby,  $X_{pc}$  and  $B$  contain the principal components of the true data.  $X_{pc}$  represents a set of temporally invariant basis vectors ( $y$ - $pc$ ) and  $B$  spatially invariant temporal frequency profiles ( $f$ - $pc$ ).

Accordingly, the training data set can be decomposed into two matrices ( $\rho_{train} = X_{train}B$ ), see Figure 7.1.2. Each voxel of the data can be calculated explicitly by:

$$\rho_{train}(y, f_m) = \sum_{i=1}^{n_{pc}} X_{train}(y, i)B(i, f_m) \equiv x_{train}(y)b(f_m) \quad (7.1.14)$$

where the columns of  $X_{train}$  and rows of  $B$  contain the principal components of the training data derived by PCA and  $n_{pc}$  is the minimum number of principal components with which the data can accurately be represented. The rows of  $B$  contain the spatially invariant PC's basis functions to build every temporal frequency profile present in the training data. The columns of  $X_{train}$  are the temporal invariant weighting coefficients.

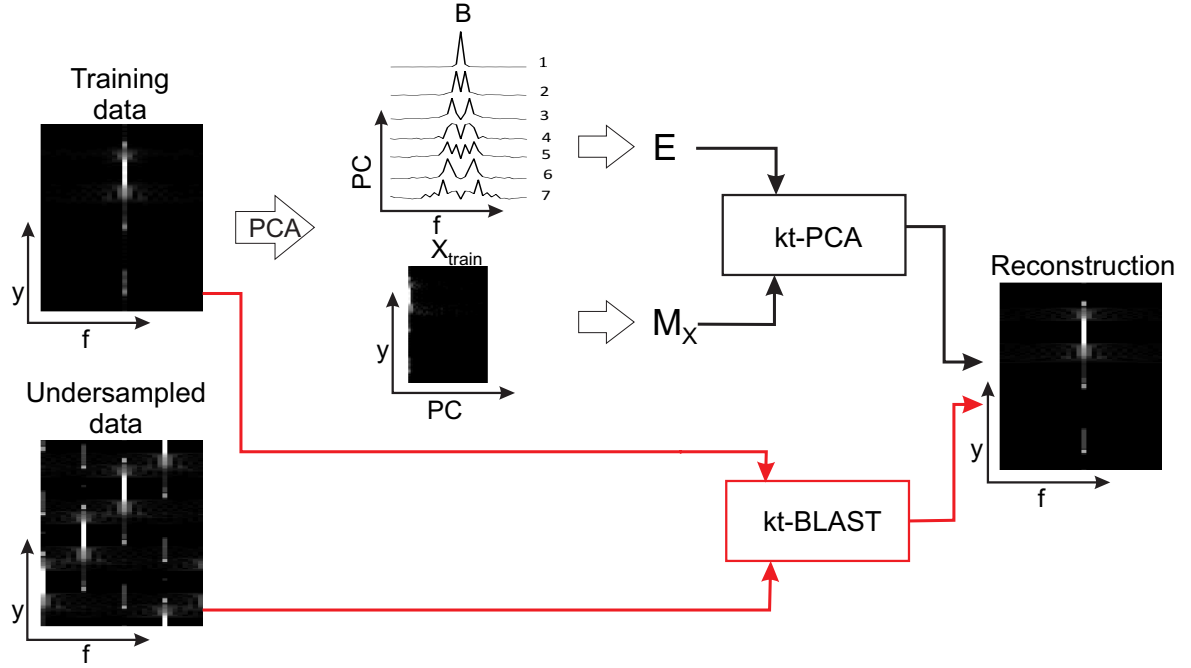


Figure 7.1.2.: Difference between the kt-BLAST and the kt-PCA reconstructions. In kt-PCA, the spatially invariant principal components  $B$  and the temporal invariant weighting coefficients  $X_{train}$  are extracted from the training data, which are used to construct the encoding matrix  $E$  and covariance matrix  $M_x$  respectively.

Now consider the undersampled data. Depending on the sampling pattern, the aliased voxels at a certain location  $(y, f_m)$  is the superposition of  $R$ -voxels from the true data:

$$\rho_{alias}(y, f_m) = \sum_{j=0}^{R-1} \rho_{true}(y_j, f_{m_j}) \quad (7.1.15)$$

Using PCA, an aliased voxel at position  $(y, f_m)$  can also be represented as:

$$\rho_{alias}(y, f_m) = \sum_{j=0}^{R-1} \sum_{i=1}^{n_{pc}} X_{pc}(y_j, i) B(i, f_{m_j}) = \mathbf{1}_y B_m \quad (7.1.16)$$

where  $\mathbf{1} = [1 \ 1 \ \dots \ 1]$ ,  $x_y$  is given by:

$$x_y = \begin{bmatrix} x^T(y_0) \\ x^T(y_1) \\ \vdots \\ x^T(y_{R-1}) \end{bmatrix}$$

and  $B_m$  by:

$$B_m = \begin{bmatrix} b^T(f_{m_0}) & 0 & 0 & 0 \\ 0 & b^T(f_{m_1}) & 0 & 0 \\ 0 & 0 & \ddots & 0 \\ 0 & 0 & 0 & b^T(f_{m_{R-1}}) \end{bmatrix}$$



$b(f_{m_j})$  and  $x(y_j)$  correspond to the row and the column of  $B$  and  $X_{pc}$  of the  $j$ 'th aliased voxel respectively. The subscript T indicates the matrix transpose. The temporal frequency profiles  $B_m$  are derived from the matrix of the training data  $B$ .

Since, the coefficient matrix  $X_{pc}$  is temporally invariant, there is an expression similar to equation 7.1.16 for each temporal frequency. Thus, the system of equations to be solved is given by:

$$\rho_{alias, y} = \begin{bmatrix} \rho_{alias}(y, f_1) \\ \rho_{alias}(y, f_2) \\ \vdots \\ \rho_{alias}(y, f_{n_f}) \end{bmatrix} = \begin{bmatrix} \mathbf{1}B_1 \\ \mathbf{1}B_2 \\ \vdots \\ \mathbf{1}B_{n_f} \end{bmatrix} x_y. \quad (7.1.17)$$

The signal encoding equation for all temporal frequencies at spatial position  $y$  can be expressed as:

$$\rho_{alias, y} = \begin{bmatrix} \mathbf{1}B_1 \\ \mathbf{1}B_2 \\ \vdots \\ \mathbf{1}B_{n_f} \end{bmatrix} x_y \equiv E \cdot x_y$$

Analogous to equation 4.4.1, the reconstruction of the data is given by:

$$x_y = M_X^2 E^H \text{pinv}(EM_X^2 E^H) \rho_{alias} \quad (7.1.18)$$

with  $M_X$  as the covariance of the matrix constructed with the rows of  $X_{train}$  ( $M_X^2 = \text{diag}(|x_{train, y}|^2)$ ). Solving equation 7.1.18 for all positions  $y$ , all columns of the matrix  $X_{pc}$  of the true object are determined and  $\rho_{true} = X_{pc}B$  is calculated.

For multi-coil data, the corresponding coefficients  $C$  of the sensitivity profiles are included in equation 7.1.15:

$$\rho_{alias}(y, f_m) = C \begin{bmatrix} \rho_{true}(y_1, f_{m_1}) \\ \rho_{true}(y_2, f_{m_2}) \\ \vdots \\ \rho_{true}(y_j, f_{m_j}) \end{bmatrix} = CB_m x_y$$

When fewer principal components are needed to accurately characterize the data, the reconstruction problem becomes more constrained. This corresponds to a reduced degree of freedom in the reconstruction and may lead to an improved removal of noise and artifacts. The number of principal components (PC's) used in the kt-PCA reconstructions will be reduced according to their significant eigenvalues.

Since the relaxation is characterized by only three parameters ( $M_0, M_0^*, T_1^*$ ), strong compressibility for high acceleration factors is expected.

## 7.2. Methods

The general goal of this thesis is to develop the optimization of acquisition strategies for dynamic data that allow reduced scan times without sacrificing image quality. In

this chapter, the reconstruction of undersampled MR relaxometry data employing kt-PCA is investigated. As PCA is a tool which extracts the most relevant information from data sets and allows their representation with fewer parameters, our hypothesis is that the redundancy of dynamic data in the new domain can be exploited. In order to demonstrate the feasibility of using a reduced amount of training data for reconstruction of relaxometry data with kt-PCA, simulated and in-vivo data are utilized.

### 7.2.1. Simulations

Synthetic MR relaxometry data were generated using IR-Snapshot FLASH and IR TrueFISP sequences from the object illustrated in Figure 7.2.1b. The brain model with matrix size of  $192 \times 192$  pixels and slice thickness of 1 mm was taken from BIC (Mc-Connell Brain Imaging Center) data [90, 91]. Standard IR-Snapshot FLASH and IR TrueFISP data were simulated in MATLAB based on the Bloch equations [92]. To simulate dynamic cardiac data, a numerical model provided by Malik S. (King’s College London, United Kingdom) with matrix size of  $192 \times 192$  pixels was used (see Figure 7.2.1).

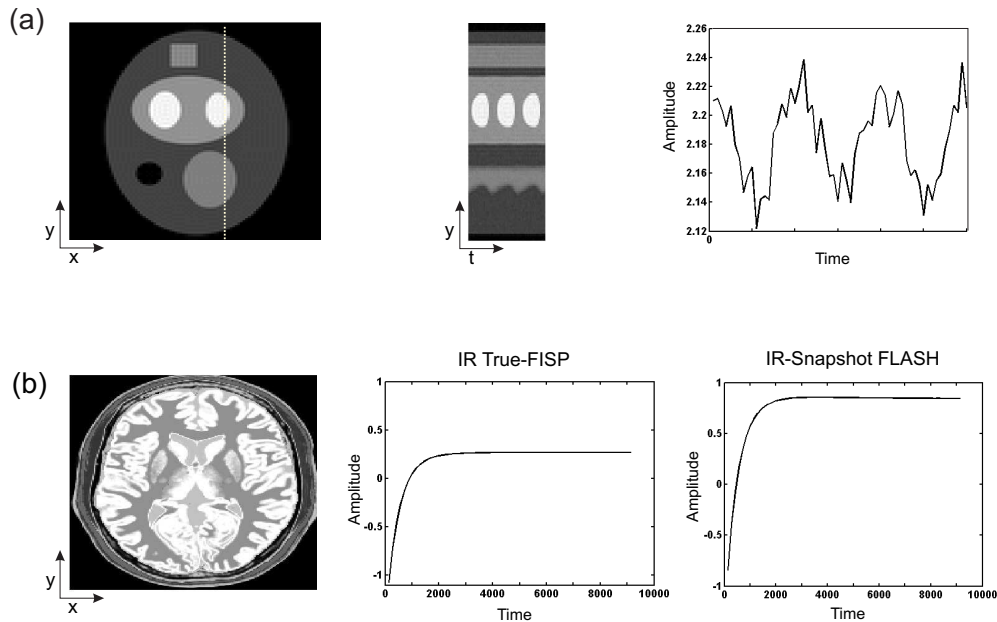


Figure 7.2.1.: (a) Simulated cardiac data. M-mode representation and the temporal evolution of a single pixel of simulated dynamic cardiac data. (b) Brain model and the relaxation curves of one specific image pixel for simulated IR-Snapshot FLASH and IR TrueFISP experiments.

For both dynamic data sets, 64 time frames for a single homogenous receiver coil were generated. Figure 7.2.1 shows different representations of the dynamic data along the temporal axis. M-mode ( $y-f$ ) representation as well as the temporal evolution of the amplitude of one pixel are illustrated in Figure 7.2.1a. Figure 7.2.1b depicts the relaxation curves of one pixel generated by simulated IR-Snapshot FLASH and IR TrueFISP brain measurements. Additionally, fully sampled simulated data sets are shown in on the

left hand side of Figure 7.2.2 in different domains. The corresponding undersampled images exhibiting aliasing artifacts are shown to the right.

The simulated data were subsampled in a Cartesian interleaved way with different acceleration factors as depicted in Figure 7.2.3 and then reconstructed using kt-PCA.  $M_0$ ,  $T_1$  and  $T_2$  maps were estimated pixel by pixel after obtaining the parameters  $T_1^*$ ,  $M_0^*$  and  $INV$  from the reconstructed data.

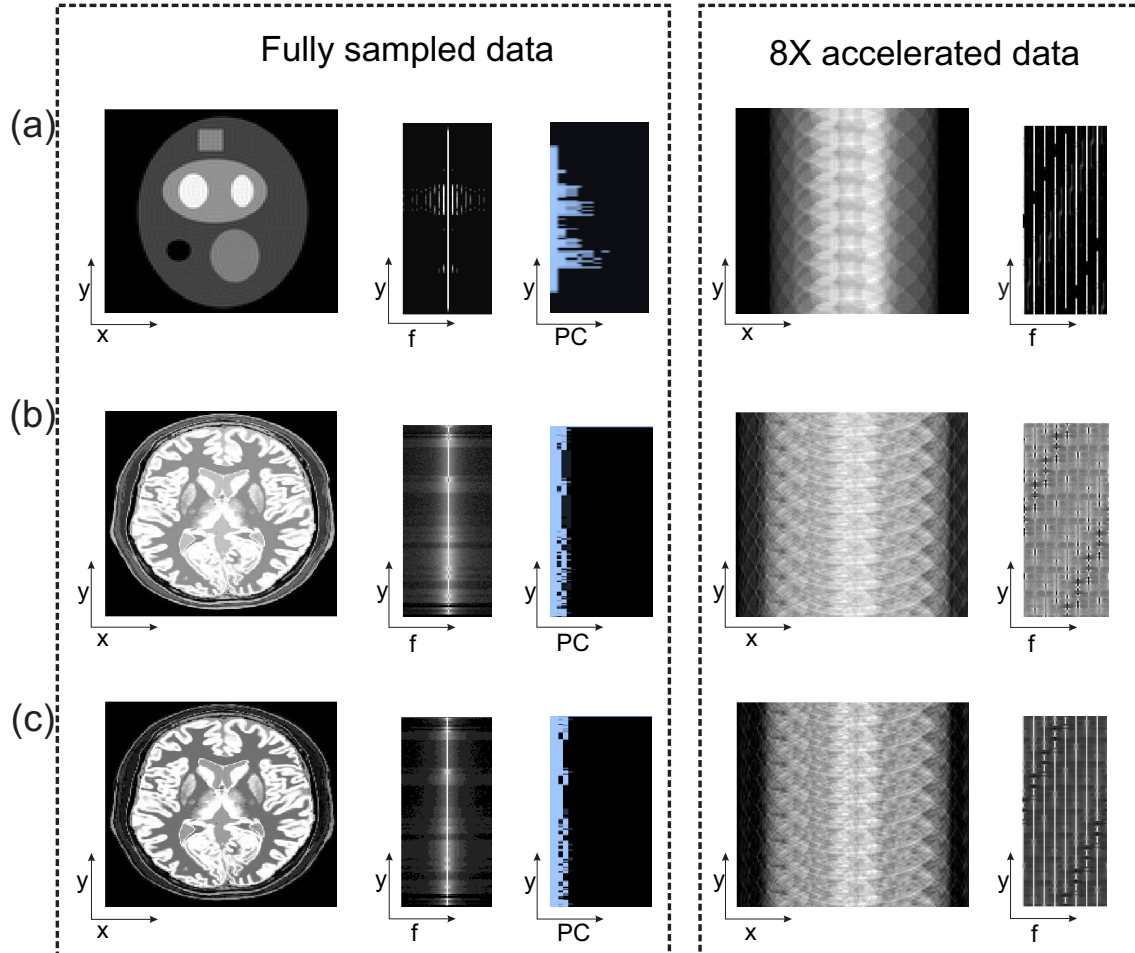


Figure 7.2.2.: The three simulated dynamic data sets used in this work. (a) Simulated dynamic cardiac data, their corresponding spectrum and the temporal invariant coefficients  $X_{pc}$  (on the right). (b) Simulated brain measurements using IR TrueFISP, their corresponding spectrum and the temporal invariant coefficients  $X_{pc}$  (on the right). (c) Simulated brain measurements using IR-Snapshot FLASH, their corresponding spectrum and the temporal invariant coefficients  $X_{pc}$  (on the right). In the box on the right hand side, the corresponding undersampled data sets and their  $y$ - $f$  representation are shown.

Various parameters affect the reconstruction quality and were investigated in more detail:

- The degree of undersampling: the simulated data were subsampled in a Cartesian interleaved way by factors of 2, 4, 6, 8 and 16.
- The resolution of training data: kt-PCA reconstructions of  $R = 8$  accelerated data were performed using training data of varying resolution (1 to 192 lines) and compared to fully sampled reference data.
- The number of principal components: as illustrated in Figure 7.2.3, kt-PCA reconstructions of  $R = 8$  accelerated data were performed using one central k-space line of training data and varying numbers of principal components.

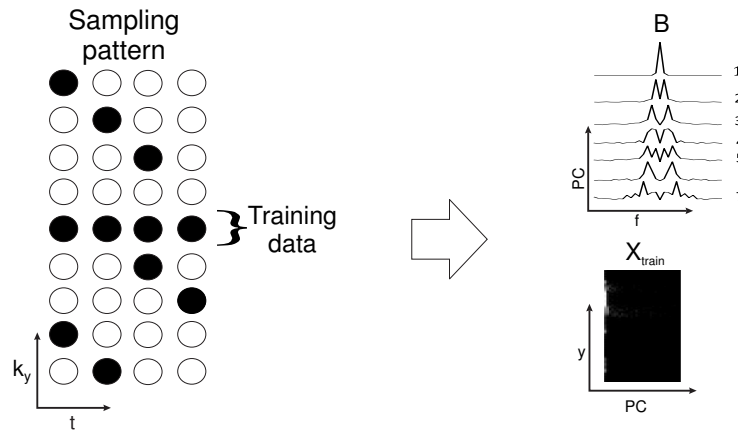


Figure 7.2.3.: Sampling pattern used for the simulated and in-vivo data. One central fully sampled k-space line is used as training data, from which the spatially invariant  $B$  matrix and the temporal invariant  $X_{train}$  are extracted.

## 7.2.2. In-vivo Measurements

All in-vivo experiments were performed on a 1.5T whole body scanner (Siemens Medical Solutions, Erlangen, Germany) using a 12-channel head array for signal reception.

Healthy volunteers were examined after informed written consents. Data were acquired using IR-Snapshot FLASH (with parameters: TR = 4.8 ms, TE = 2.4 ms, matrix size of  $208 \times 256$ , FOV =  $241 \times 296$  mm<sup>2</sup>, slice thickness = 10 mm, flip angle = 8°, number of contrast = 64) and IR TrueFISP (with parameters: TR = 5 ms, TE = 2.5 ms, matrix size of  $208 \times 256$ , FOV =  $241 \times 296$  mm<sup>2</sup>, slice thickness = 10 mm, flip angle = 50°, number of sampled points along the relaxation curve = 64, 45 and 33). Eight k-space segments were acquired to provide a fully encoded reference. Acquisition times per segment were 4.3 s for 33 temporal frames, 5.8 s for 45 temporal frames and 8.3 s for 64 temporal frames. Between the acquisition of each individual k-space segment, a 10 s time delay was inserted to allow full relaxation of the magnetization to its thermal equilibrium. Thus the overall scan time per slice for fully sampled images was between 1:54 min for series with 33 temporal frames and 2:24 min for series with 64 temporal frames.

The data were retrospectively subsampled in a Cartesian interleaved way by factors 2, 4, 8 and 16. Reconstructions were performed using kt-PCA. For evaluation, in-vivo data

were reconstructed using just the central k-space line for training data and compared to the reference data. Additionally, reconstructions with a varying number of principal components (1, 2, 3, 4, 5, 6 and 10) and a varying amount of training data (1 to 45 k-space lines) were performed. Furthermore, using IR TrueFISP measurements, the influence of a varying number of contrasts was investigated.

$M_0$ ,  $T_1$  and  $T_2$  maps were estimated pixel by pixel fitting the data to the parameters  $T_1^*$ ,  $M_0^*$  and  $INV$  for both IR-Snapshot FLASH and IR TrueFISP acquisitions and for both reference and kt-PCA reconstructed data.

## 7.3. Results

### 7.3.1. Simulations

As shown in Figure 7.2.2, the simulated brain images (in their  $y$ - $f$  representation) exhibit signal across all the frequencies because the relaxation effects occur in every single pixel of the image. This is not the case for simulated dynamic cardiac images (see Figure 7.2.2c). In dynamic cardiac images, temporal changes occur just at some voxels within the whole image and many voxels remain relatively static. Using PCA analysis, MR relaxometry data can experience a strong compression because just a few principal components contain the whole information ( $y$ - $pc$ ) and suffice for representing the original data set ( see Figure 7.2.2a and b).

#### Influence of Acceleration Factor

It is known that kt-PCA achieves good quality reconstructions of highly accelerated dynamic data [93]. Here, we used numerical simulations to demonstrate what degree of subsampling of relaxometry data is tolerated by the kt-PCA algorithm without leading to artifacts in reconstructed images. Using 3 PC's, reconstructions from various data sets accelerated by factors of 2, 4, 8 and 16 are compared to the reference data (Figure 7.3.1a). The difference between the reconstruction errors (Root Mean Square Error, RMSE) of  $R = 4$  and  $R = 8$  undersampled data sets is relatively small. However, reconstruction errors of  $R = 16$  undersampled data increase dramatically.

Additionally, the relaxation curves of a pixel of reconstructed  $R = 8$  (red) and reference (blue) data sets are depicted in Figure 7.3.1b. Here, the SNR of the first six frames of the reconstructions is relatively poor, causing the deviation from the reference.

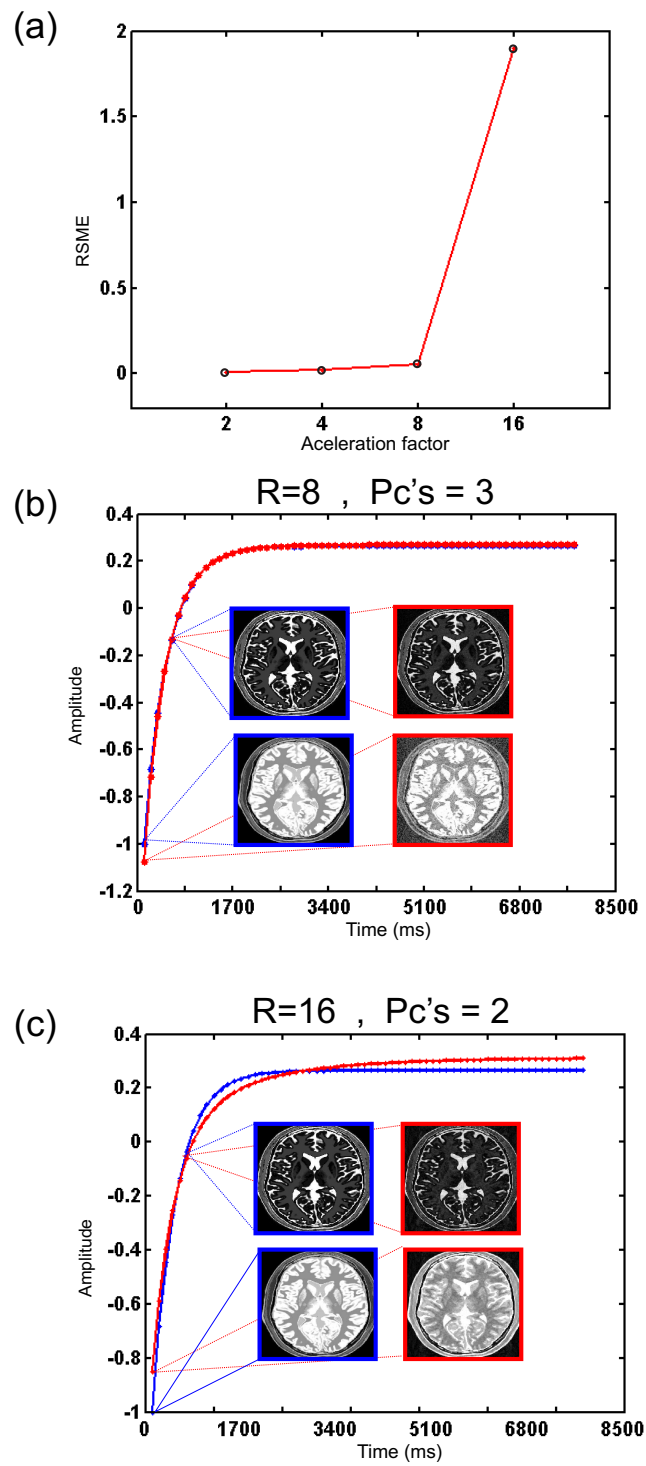


Figure 7.3.1.: IR True FISP simulation results. (a) The relative root mean square errors of reconstructions of  $R = 2, 4, 8$  and  $16$  accelerated data using  $3$  PC's. (b) Relaxation curves of one pixel from the reconstruction of  $R = 8$  accelerated data using  $3$  PC's (red) and from the reference data (blue). (c) Relaxation curves of one pixel from the reconstruction of  $R = 16$  accelerated data using  $2$  PC's (red) and reference data (blue).

Also shown are example images at two time points along the relaxation curve (reference and reconstructed frames of accelerated data  $R = 8$  using 3 PC's and  $R = 16$  using 2 PC's).

### **Influence of Training Data**

The linearly independent temporal profiles in  $f$ - $pc$  domain ( $B$ ) and temporally invariant basis functions in  $y$ - $pc$  domain ( $X_{train}$ ) are extracted from the training data set in the kt-PCA algorithm. To determine the optimal number of training lines, it is important to know if these basis functions undergo changes when varying the amount of training lines. In Figure 7.3.2, the three most significant PC's obtained from 1, 2 and 20 training lines are depicted. Apparently, the amount of training lines does not affect the information carried by the three most significant PC's. The negligible difference between the RMSE of reconstructions with 20, 2 and 1 training lines using the first three PC's, suggested that accurate reconstructions can be obtained regardless of the amount of training data.

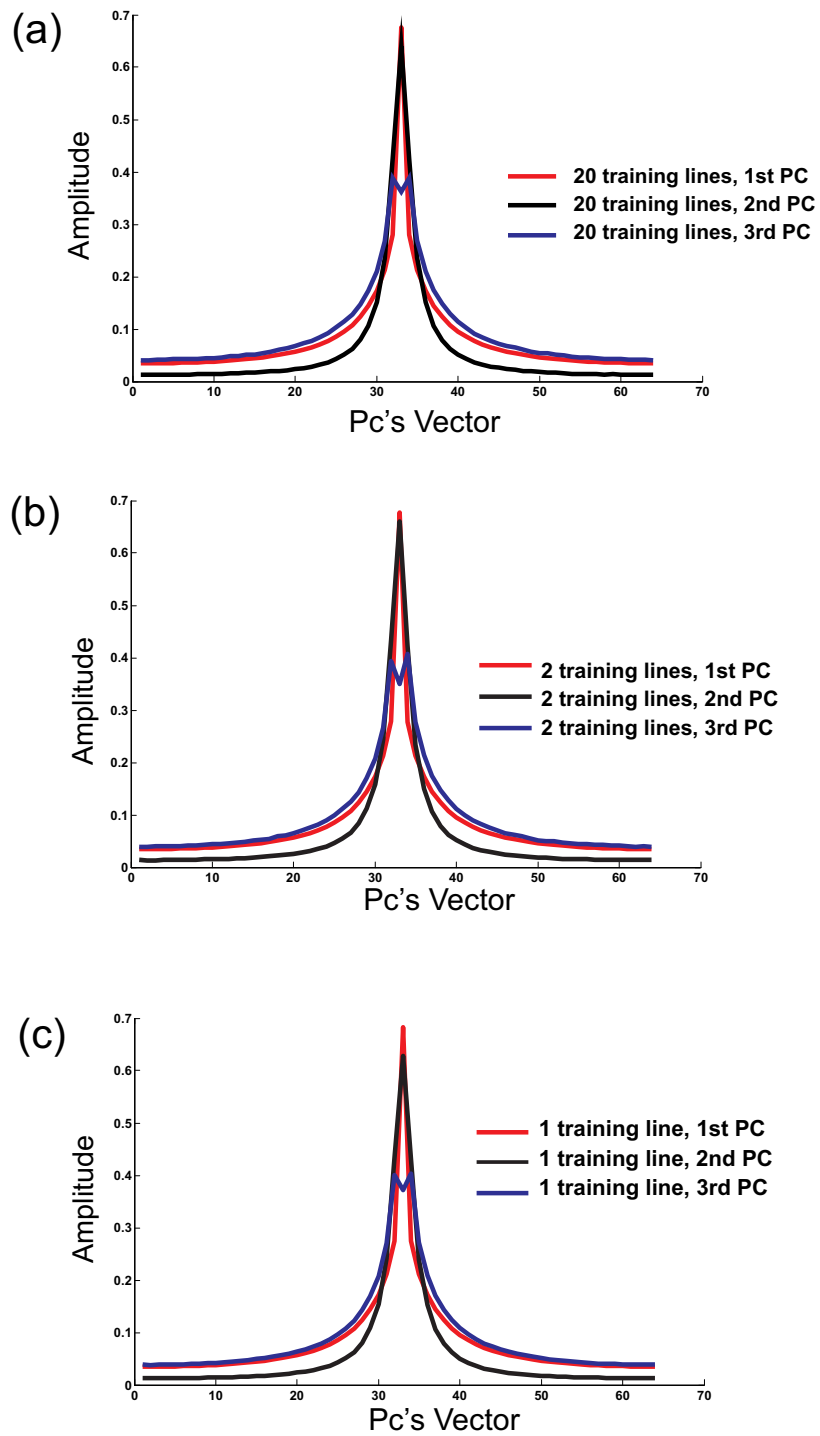


Figure 7.3.2.: The first three principal components (PC's) of: (a) 20 training lines, (b) 2 and (c) 1 training line.

### Influence of the Number of Principal Components

As described in appendix A, the eigenvalues extracted from the original data are a mea-



sure of the amount of information required for characterization. Large magnitudes of eigenvalues indicate high relevance for accurately representing the original data. For IR-Snapshot FLASH and IR TrueFISP measurements, the magnitude of the eigenvalues decays rapidly compared to the eigenvalues of dynamic data as indicated in Figure 7.3.3. Relaxometry data can be accurately represented by only their 3-4 first PC's, because the magnitude of the remaining eigenvalues tends to zero. In contrast, 7-8 PC's are required to accurately characterize dynamic cardiac data. Errors of reconstructed MR relaxometry and dynamic cardiac data sets obtained by using in between 1 and 8 PC's are also depicted. Ideally, for noiseless data the error approaches zero with the complete basis (PC's = 64). Here, we chose the optimal number of principal components that minimize the error in the reconstruction.

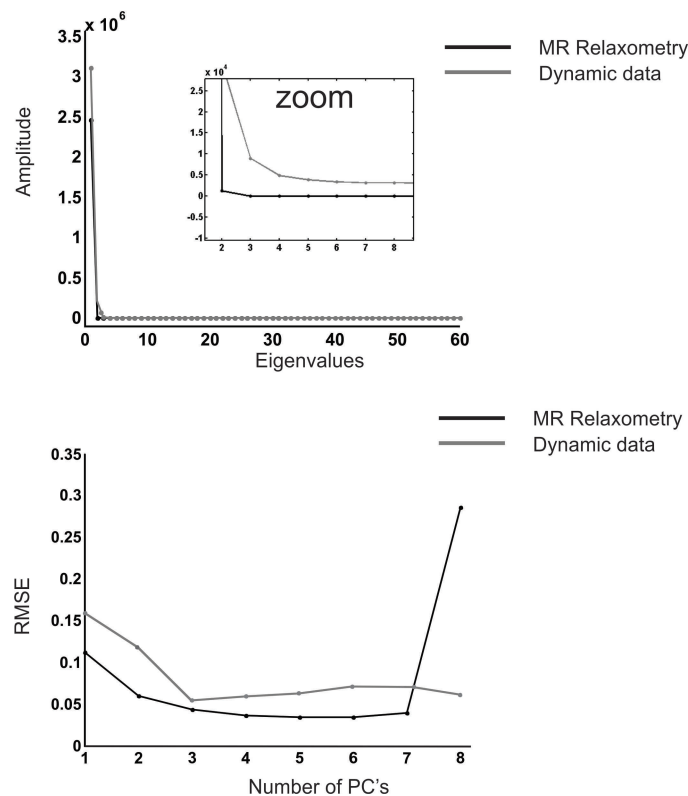


Figure 7.3.3.: The graphic on top illustrates the magnitude of the eigenvalues of both relaxometry and dynamic data. The errors introduced by reconstructions of  $R = 8$  accelerated data varying the number of PC's are shown on the bottom.

Additionally  $M_0$ ,  $T_1$  and  $T_2$  maps were estimated from kt-PCA reconstructions of  $R = 8$  accelerated IR TrueFISP measurements, using just 3 PC's and one line of training data (Figure 7.3.4).

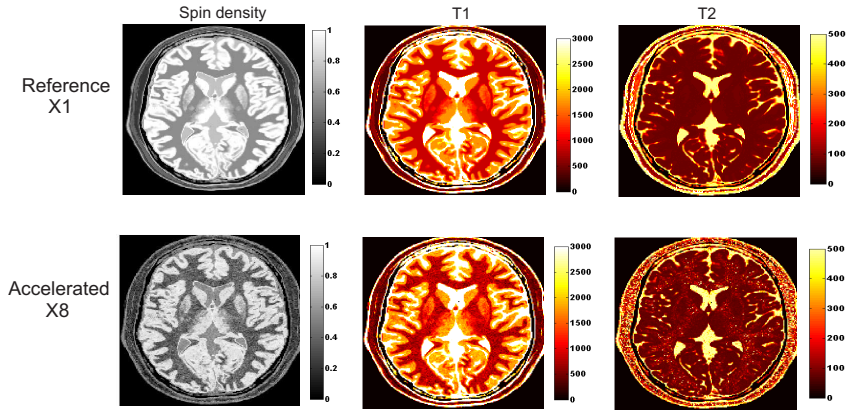


Figure 7.3.4.:  $M_0$ ,  $T_1$  and  $T_2$  for simulated IR TrueFISP measurements. Maps of the fully sampled data are shown on the top. kt-PCA reconstructions from  $R = 8$  accelerated IR TrueFISP measurements using just 3 PC's and one line of training data are shown on the bottom.

It can be observed that the spin density map estimated from the reconstructed data exhibits a higher deviation from the reference data set in contrast to  $T_1$  and  $T_2$  maps. Especially the  $T_1$  map is very similar to the reference.

### 7.3.2. In-vivo Experiments

#### Influence of Acceleration Factor

Figure 7.3.5a shows the reconstruction error of IR-Snapshot FLASH and IR TrueFISP data sets using different acceleration factors (from 2 to 16). Only a small increase of the deviation can be observed up to an acceleration factor of 8, with a considerable increase for an acceleration factor of 16.

The influence of the number of temporal frames on the reconstruction is shown in Figure 7.3.5b. Using the same temporal resolution, acquisition of one segment takes in between 4.3 s for 33 temporal frames and 8.3 s for 64 temporal frames. A slight decrease of the RMSE of reconstructed data using a higher number of temporal frames can be observed. However, the number of frames per temporal series is limited by the acquisition time.

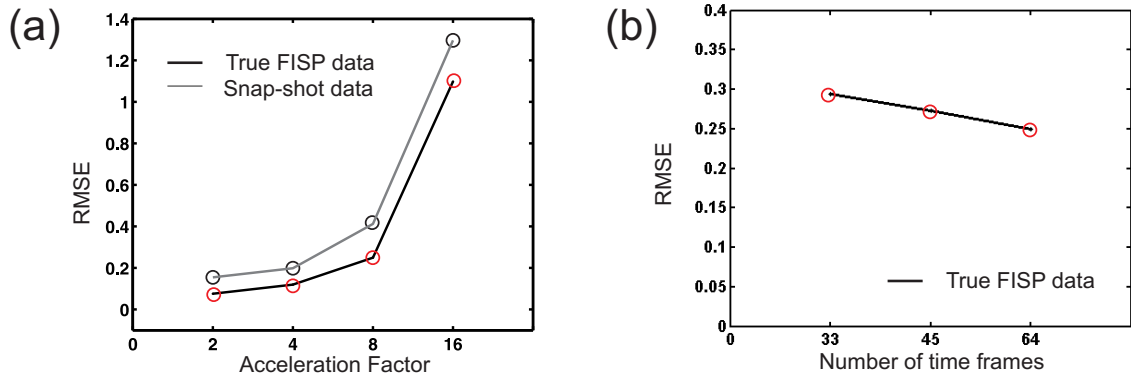


Figure 7.3.5.: Reconstruction errors for IR TrueFISP and IR-Snapshot FLASH measurements of accelerated data with factors 2, 4, 8 and 16 using one training line and 3 PC's (a) and varying the number of frames per temporal series (b).

Figure 7.3.6 shows the first four time frames of reconstructions from  $R = 2, 4$  and 8 accelerated IR TrueFISP measurements. The SNR degradation in the reconstructed data is more evident at higher acceleration factors. However, the perturbation in the relaxation curve is minimal.

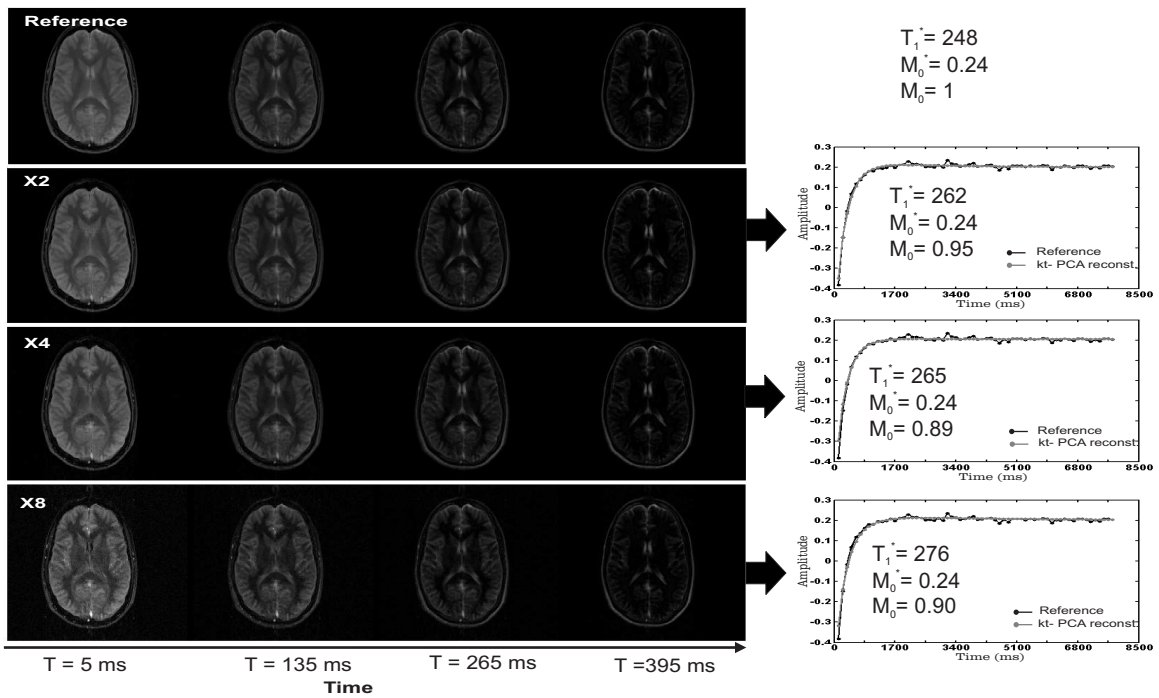


Figure 7.3.6.: Reference and reconstructed frames for acceleration factors of 2, 4 and 8. The relaxation curves in one particular pixel shown to the right.

### Influence of Training Data

In experimental data as well as in simulations, the number of training lines in kt-PCA has no significant influence on the reconstructed data. In Figure 7.3.7, the reconstruction errors for IR TrueFISP and IR-Snapshot FLASH measurements are plotted varying the amount of training data lines.

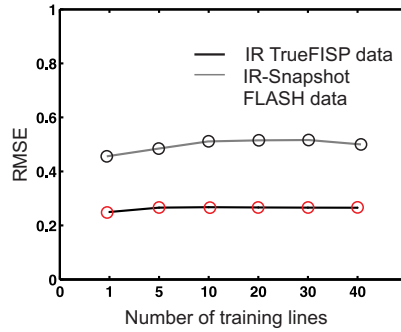


Figure 7.3.7.: Relative reconstruction errors for IR-Snapshot FLASH and IR TrueFISP accelerated data with  $R = 8$  using 3 PC's and varying the amount of training data lines.

The small increase between reconstruction errors using one and several lines of training data can be explained by the contribution of additional noisy data that deteriorates the SNR of reconstructions.

### Influence of the Number of Principal Components

The simulations showed that the number of PC's used for reconstruction is crucial for optimal results. Figure 7.3.8 shows errors of reconstructions from  $R = 8$  undersampled IR-Snapshot FLASH and IR-TrueFISP data varying the number of PC's. A number of 2 PC's seem to be optimal for the IR-Snapshot FLASH experiments and 3 PC's for the IR TrueFISP data.

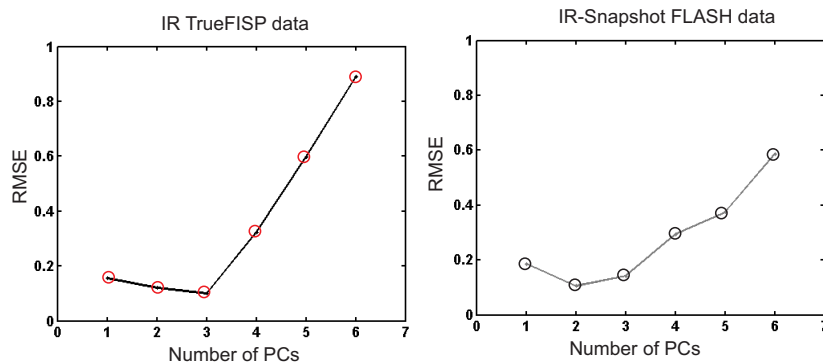


Figure 7.3.8.: Relative reconstruction errors for IR-Snapshot FLASH (right) and IR TrueFISP (left)  $R = 8$  accelerated data using one training line and varying the amount of PC's.

## Parameter Mapping

Figure 7.3.9 depicts the relaxation of one particular pixel in IR TrueFISP and IR-Snapshot FLASH reconstructions (red curves) and reference data (blue curves) along the time axis. In both cases, the reconstructions of  $R = 8$  accelerated data closely follow the temporal evolution of the reference data. Rapid fluctuations along the relaxation curve present in the reference data are removed due to the elimination of irrelevant PC's during reconstruction.

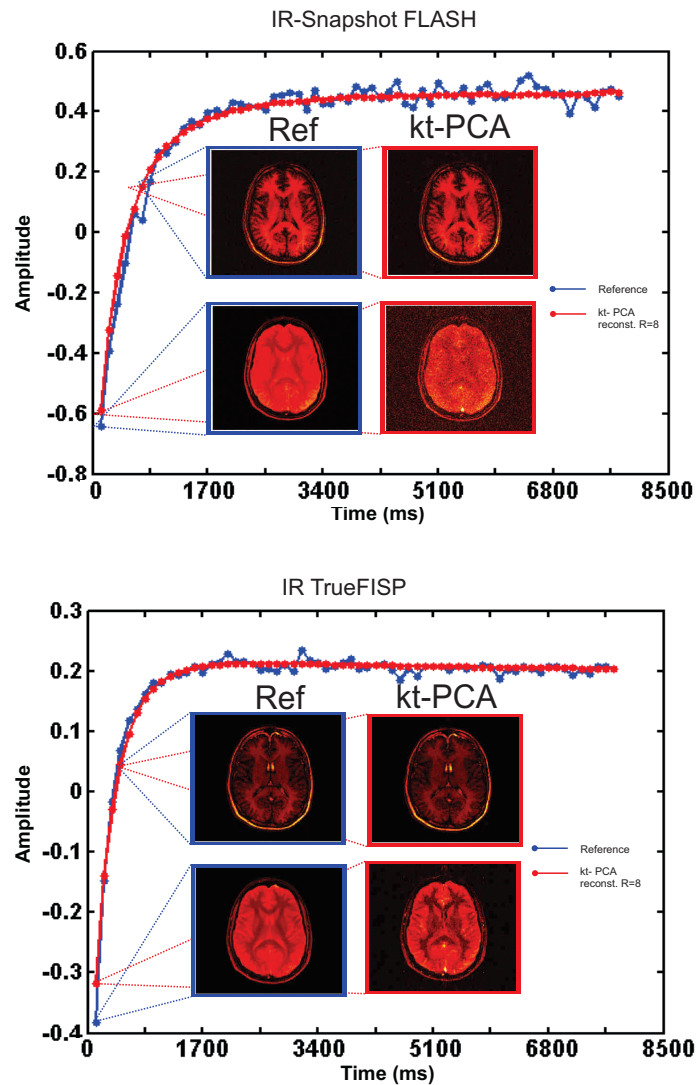


Figure 7.3.9.: Relaxation curves of reference (blue) and reconstructed data, from  $R = 8$  accelerated IR-Snapshot FLASH and IR TrueFISP sets (red) using 1 training line and 2 and 3 PC's respectively.

In general, IR TrueFISP reconstructions have higher SNR than IR-Snapshot FLASH reconstructed data. In both cases, the first six temporal frames exhibit larger deviation from the reference. More specifically, as shown in Figure 7.3.9, the first frame of IR

TrueFISP reconstructions has the largest error. This does not affect the estimation of  $M_0^*$  and  $T_1^*$  parameters in the fitting process. However, big errors in the first temporal frame for IR TrueFISP series lead to wrong estimation of  $INV$  parameter, which is directly related to the spin density ( $M_0$ ) map.

The spin density maps ( $M_0$ ) calculated from IR-Snapshot FLASH reconstructed data are very noisy and the structures of the brain are difficult to distinguish, as depicted Figure 7.3.10. The average of all the pixel values in  $T_1$  and  $M_0$  maps was underestimated by 15% and 9%, respectively.

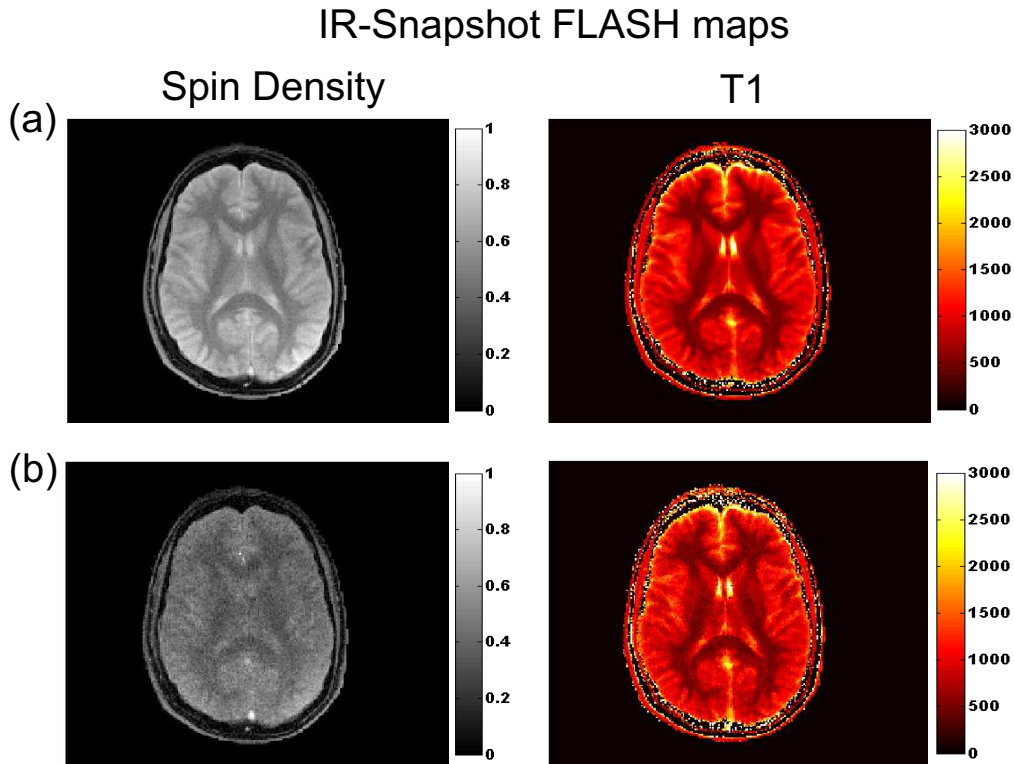


Figure 7.3.10.: Spin density ( $M_0$ ) and  $T_1$  maps of IR-Snapshot FLASH data sets: (a) reference and (b) kt-PCA reconstruction of accelerated data by a factor of 8 using 2 PC's and one line of training data.

Maps obtained from the reconstructions of undersampled IR TrueFISP data sets with 64 and 33 temporal frames are shown in Figure 7.3.11 a and b respectively. Maps estimated from reconstructed data sets with 33 temporal frames present significant errors due to the low SNR. For the data set with 64 temporal frames, the average of all the pixel values in  $M_0$ ,  $T_1$  and  $T_2$  maps was underestimated by 9%, overestimated by 5% and underestimated by 6%, respectively.

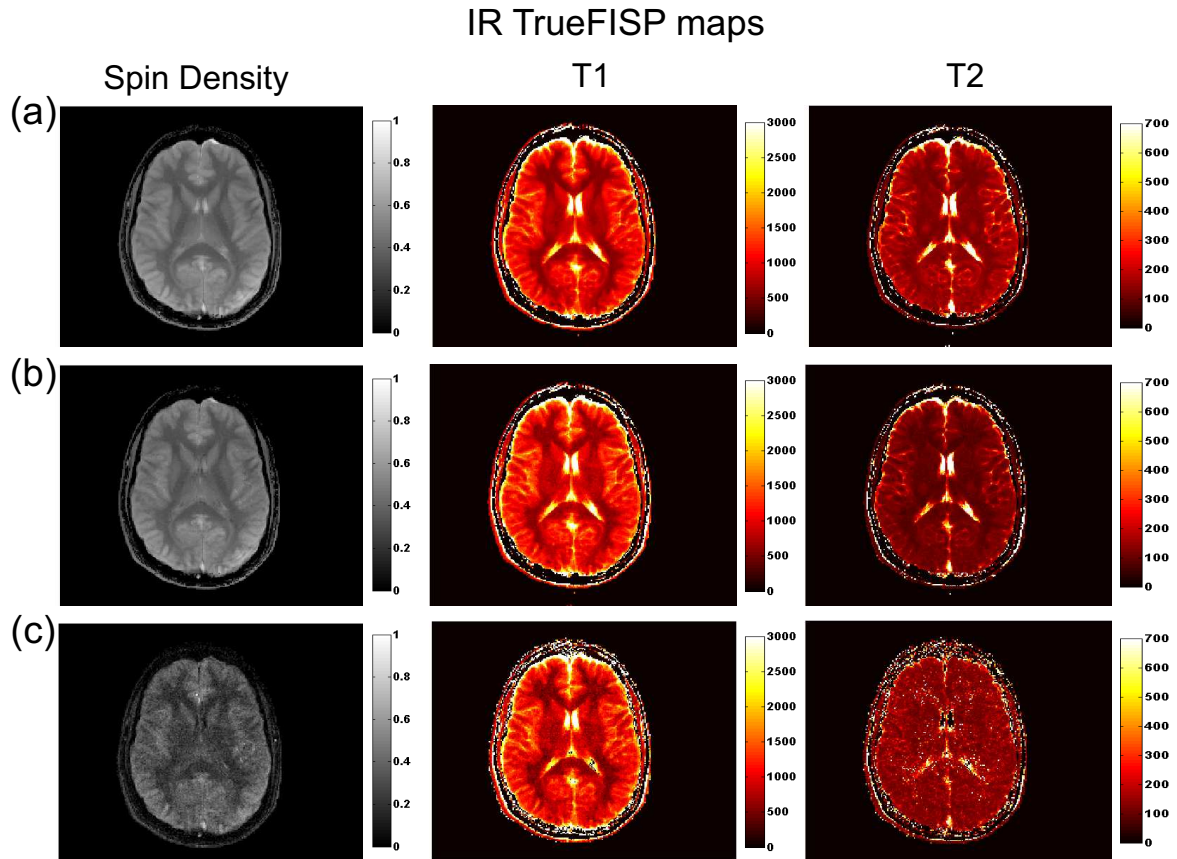


Figure 7.3.11.: Spin density ( $M_0$ ),  $T_1$  and  $T_2$  maps estimated from IR TrueFISP: (a) reference data, (b) 64 time frames and (c) 33 time frames of  $R = 8$  accelerated data using 3 PC's and one line of training data.

## 7.4. Discussion and Conclusions

This work opens the possibility to obtain accurate MR parameter maps from highly accelerated acquisitions. The amount of training data needed for the kt-PCA approach could be reduced to a single k-space line, which leads to a further decrease of acquisition time. For fully sampled IR-Snapshot FLASH and IR TrueFISP experiments (spatial resolution = 1.16 mm/pixel), the acquisition time was approximately 2 min. However, for accelerated acquisitions, the scan time can be significantly reduced, for example to only 8 s for an 8-fold acceleration. Further optimization for the acquisition of relaxometry images is possible using a modified IR TrueFISP that avoids the delay between segments and allows higher resolution as described in F. Petzschner's thesis [94].

It has been demonstrated that the number of PC's chosen for the kt-PCA reconstruction process is crucial to obtain accurate results. A lower number of principal components constrains the reconstruction and produces good separation of the overlapped signals. Since the mono-exponential signal course of relaxometry data can be described by few parameters, the PCA decomposition was shown to be advantageous for the reconstruc-



tion. Results of in-vivo experiments and simulations confirmed that the number of PC's necessary to accurately describe MR relaxometry data is lower than the number of PC's required to represent dynamic cardiac data. In the presented examples, 2 or 3 PC's were sufficient to produce optimal reconstructions. In contrast, 10 PC's are needed for the accurate representation of cardiac imaging.

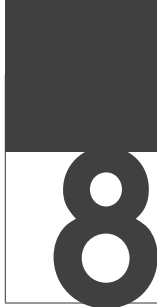
Thanks to the high redundancy of MR relaxometry data, the required amount of training data could be reduced up to only one central k-space line, as shown for both simulated and in vivo data. The parameter maps extracted from kt-PCA reconstructions show no significant deviations from the respective references. The acquisition of just one central line instead of several extra central lines, that are typically required by the kt-PCA algorithm, could be promising to improve the scan efficiency.

Good results were obtained with the kt-PCA algorithm for acceleration factors up to  $R = 8$ . In the case of higher acceleration factors, we constrained the reconstruction problem by reducing the number of principal components (PC's) in order to eliminate the residual aliasing artifacts. However, the lack of information leads to a miscalculation of the reconstructed data and therefore temporal filtering.

The main difference between IR TrueFISP and IR-Snapshot FLASH reconstructions lies in the higher SNR achieved by larger flip angles ( $50^\circ$ ) employed in the IR TrueFISP sequence. In general, the SNR of reconstructed MR relaxometry data remains constant regardless of the amount of training data lines. However, the small increment between the error of reconstructed IR-Snapshot FLASH data using one training line and more training may be the result of noise amplification, as other than the central k-space line exhibit more noise. The noise amplification takes place during the inversion of the covariance matrix  $M_X^2$  in equation 7.1.18 and decreases with the number of acquired time points.

In this chapter, it was shown that the kt-PCA approach may allow a highly efficient reconstruction of MR relaxometry. Acquisition time can be significantly reduced not only because of acceleration of the actual data but also due to the reduction of the required amount of training data. The kt-PCA method is able to provide reconstructions of MR relaxometry data with the quality required to estimate accurate MR parameter maps using just one training line.





Chapter 8.

## Summary and Outlook

Since the introduction of the parallel Magnetic Resonance Imaging (pMRI), the primary goal of many research projects has been and still is a reduction of acquisition time without sacrificing image quality. The complexity of both acquisition and reconstruction is especially high when only a limited temporal window is available to obtain data, e.g. for objects with high dynamics. Partial acquisition of the data reduces scan times and allows to capture even rapid motions. The challenge for dynamic pMRI techniques in particular is to accurately reconstruct artifact-free images from accelerated measurements without compromising temporal fidelity. Dedicated reconstruction techniques such as SENSE [7] and kt-SENSE [15] require reference or training data for estimating missing data. The training data usually have to be acquired in an additional measurement, which increases the overall scan time. In order to reduce or totally eliminate this extra acquisition for dynamic data, several different strategies were proposed in this work.

Several auto-calibrating methods have been proposed for the reconstruction of dynamic data, that generate the reference data (e.g. spatial information) required from the undersampled data itself. However, these approaches have some drawbacks, which has been demonstrated in this work for the example of kt-SENSE. The temporal average of Cartesian interleaved undersampled data yields a fully sampled image, that can be used for the estimation of the coil sensitivity maps required by kt-SENSE. However, this temporal average may contain contributions from aliased components and deviates from the true temporal average. Using coil sensitivity maps that were estimated from the undersampled data may therefore lead to signal nulls in the reconstructed spectra. This corresponds to temporal filtering, as demonstrated in Chapter 5. To obtain accurate reconstructions using an auto-calibrating approach, it is necessary to significantly reduce the aliased components present in the temporal average of the accelerated data. For Cartesian acquisitions, this can be achieved by applying a GRAPPA filter to the temporal average, which prevents signal nulls in the reconstructed data [60]. A different possibility demonstrated in this work is to use radial sampling, that inherently has less severe aliasing artifacts and allows a more accurate estimation of the temporal average [70]. This also significantly reduces the undesired temporal filtering effect. Similar

findings are expected for all trajectories with highly incoherent aliasing artifacts in the presence of undersampling.

In conventional kt-SENSE, the extra spatio-temporal information required for reconstruction is obtained via an additional training data scan. To reduce measurement time, usually a lower resolution is chosen for this extra acquisition. However, the quality of the training data directly influences the spatial and temporal resolution of the reconstructed data. Lower resolution training data may lead to temporal filtering effects in the reconstructions.

In Chapter 6 of this thesis, an auto-calibration approach for kt-SENSE is proposed that eliminates the need for extra acquisitions and at the same time provides calibration data of full resolution [75]. The proposed auto-calibrating kt-SENSE is based on the feedback regularization [13]. In this method, training data are obtained by performing a TSENSE reconstruction on the undersampled data as a first pass. The full spatial resolution of the training data set results in reduced temporal filtering and therefore lower temporal blurring in the kt-SENSE reconstructions. Comparing the results of auto-calibrating kt-SENSE and conventional kt-SENSE with training data of full spatial and temporal resolution reveals only negligible differences in terms of temporal fidelity. However, the cost of the auto-calibrating approach is the reduction of SNR in the reconstructions due to noise propagation from the TSENSE reconstructions to the final kt-SENSE images. Nevertheless, as demonstrated in experiments with standard protocol parameters the proposed method shows a high level of robustness.

A different method used in dynamic MRI applications is kt-PCA [16], that was first proposed for the reconstruction of MR cardiac data. In Chapter 7 of this thesis, kt-PCA was employed for the generation of spatially resolved  $M_0$ ,  $T_1$  and  $T_2$  maps from a single accelerated IR-TrueFISP or IR-Snapshot FLASH measurement. In contrast to cardiac dynamic data, MR relaxometry experiments exhibit signal at all temporal frequencies, which makes their reconstruction more challenging. However, since relaxometry measurements can be represented by only few parameters, the use of few principal components (PC) in the kt-PCA algorithm can significantly simplify the reconstruction. While 7-10 PC's are necessary to accurately describe dynamic cardiac data, it was demonstrated that 2-3 PC's characterize relaxometry measurements. Results confirmed that accurate reconstructions from undersampled relaxometry images can be obtained using the kt-PCA method. Furthermore, it was found that due to high redundancy in relaxometry data, PCA can efficiently extract the required information from just a single line of training data. Only small errors can be observed for simulated and in-vivo IR experiments. In conclusion, kt-PCA allows accurate reconstructions of MR parameter maps using a significantly reduced amount of training data, which leads to shorter acquisition times.

In general, in both kt-SENSE and kt-PCA a temporal filter is applied to the undersampled data during reconstruction. Hereby, the particular design of the temporal filter is extracted from the training data. For both techniques, a successful suppression of aliasing artifacts is highly dependent on the quality of the training data. As demonstrated,

auto-calibrating kt-SENSE can be employed to reconstruct dynamic cardiac images up to an acceleration factor of 5 with high temporal fidelity. In this approach, training data are obtained from the undersampled data themselves, which removes the need for extra acquisitions. kt-PCA on the other hand allows the estimation of accurate spatially resolved parameter maps from undersampled inversion recovery data up to an acceleration factor of  $R = 8$ . Hereby, a single central line is sufficient as training data, which accelerates the acquisition process.

In conclusion, in this work, we were able to significantly reduce or totally eliminate the acquisition of training data for two different dynamic MRI reconstruction methods without compromising reconstruction quality. We were able to demonstrate for in-vivo experiments and simulations that the proposed approaches are able to both improve the temporal fidelity of reconstructed data and reduce acquisition times at the same time.

## Outlook

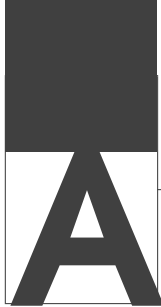
In this work, dynamic MRI applications were investigated exclusively in two-dimensional experiments. A much more complex scenario is 3-D dynamic MRI. Due to the additional phase encoding direction, the acquisition time increases for 3-D MRI. However, 3-D imaging has some substantial advantages. For example, it allows the coverage of whole organs in the human body, avoiding misregistration and may provide more accurate diagnoses. Additionally, due to its inherently high SNR and therefore the possibility to accelerate in an additional dimension with pMRI, higher acceleration factors can be achieved with parallel imaging without severely compromising image quality. Therefore, an extension of the proposed semi and auto-calibrating methods to 3-D imaging is highly desirable as it may reduce scan times significantly. Based on the consistency and temporal fidelity of reconstructed 2-D data, a successful application of the proposed methods to 3-D imaging seems likely.

In general, dynamic MRI struggles with long acquisition times and motion artifacts, especially if patients have difficulties to either stay immobile or to hold their breath. The application of auto-calibrating kt-SENSE or kt-PCA could lead to acceleration in the acquisition process and also to reduce motion artifacts due to the robustness of the approaches. kt-PCA could be especially promising in applications with a simple temporal dynamics, such as relaxometry, contrast enhanced perfusion or angiography studies.

Auto-calibrating kt-SENSE uses TSENSE for the reconstruction of training data. Noise amplification in the training data also transfers to the final reconstructed images diminishing their SNR. A future area of research could be the improvement of SNR in the reconstructed training data set. This may for example be achieved by introducing additional constraints in the TSENSE algorithm.

In this thesis, it was demonstrated that auto-calibrating kt-SENSE is able to obtain accurate reconstructions with high temporal fidelity without increasing the acquisition

time. Despite its advantages, the application of this technique is limited by its insufficient SNR and moderate degree of acceleration factor of the data. Therefore, its clinical adoption requires further works. For relaxometry studies, where the relaxation signal occurs at every single pixel of the image and therefore their reconstruction may be challenging, kt-PCA has been proven to be a suitable method. In this particular application, only one central k-space line of training data was sufficient, which is expected to be true for other applications with a simple temporal dynamics. This could be useful for many cases, especially where higher spatial or temporal resolution is needed.



## Principal Component Analysis (PCA)

Principal Component Analysis (PCA) [95] is a useful tool for data analysis. A PCA transformation finds a set of basis vectors that is best suited for describing a particular data set. Even data of high dimensionality can often be described with high accuracy by only a few basis vectors after PCA. Therefore, PCA is widely used for reducing the number of dimensions [96] and the extraction of characteristic information from data.

PCA searches for the linear combination of the original data that provides the maximal variance [97]. Consider a data set  $X$  arranged in a matrix of size  $n \times m$ , where  $n$  and  $m$  represent the number of observations and the dimensions of the data respectively. The matrix  $X$  can be expressed by a new representation  $Y$ , which is another matrix of size  $n \times m$ , using a linear transformation  $P$ :

$$PX = Y \tag{A.0.1}$$

The rows of  $P$  are the new basis vectors, which are given by the principal components (PC) extracted from  $X$ . In order to find the optimal transform  $P$ , it is necessary to examine the characteristics of the desired matrix  $Y$ .

For the new coordinate system of the data ( $Y$ ), the first axis corresponds to the largest variation in the data points, the second axis corresponds to the next largest variation in the data and so on. If PCA is for example performed on a data set with noise, the first components mainly represent the dynamics present in the data and correspondingly have a high SNR, while the later components indicate almost exclusively contain noise. Figure A.0.1 illustrates this phenomenon for the example of linear data in 2-D that exhibit some level of scattering in the orthogonal direction. The new axes determined by PCA are parallel to the direction of the principal components of the data. The first principal component has the largest possible variance and each succeeding component has a lower variance under the constraint that it be orthogonal to the preceding components.

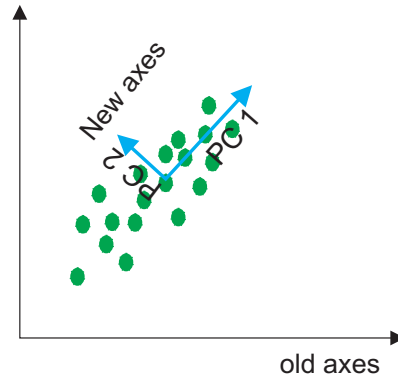


Figure A.0.1.: Change of axis during PCA. The data cloud is scattered along a line. The blue axes depict the new reference frame based on the principal components of the data.

The level of redundancy present in a particular data set indicates how much information (in average) is measured multiple times. This is the central idea behind dimensional reduction. Figure A.0.2 shows three data sets obtained from measurements of two variables  $r_1$  and  $r_2$  with different degrees of redundancy. While the left hand graph depicts two variables with no apparent relationship or correlation, the data in the right hand graph exhibit a high level of correlation. In the latter case, it would be more efficient to describe the data with a single variable.

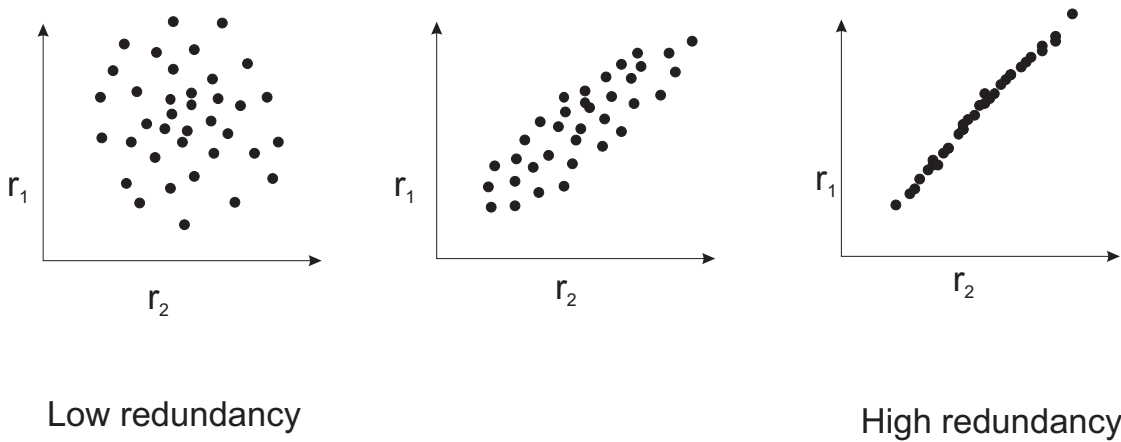


Figure A.0.2.: Three levels of redundancy.

Numerically, linear independence between the data can be identified using covariance. By definition, the covariance matrix  $C_X$  of matrix  $X$  is given by:

$$C_X \equiv \frac{1}{n} X X^T \tag{A.0.2}$$

$C_X$  is a square symmetric matrix of size  $m \times m$ . The diagonal elements of  $C_X$  are the variance of particular measurement types and its off-diagonal terms indicate the covariance between variables. Large values in the diagonal and off-diagonal term correspond

to important structure and high redundancy in the data respectively.

As already mentioned, the goal of PCA is to find new basis to represent the original data, in which their first components have the direction of the largest variances and have lowest redundancy between them. In other words, the desired matrix Y should have a diagonal covariance matrix  $C_Y$  which indicates a decorrelation of the data. Additionally, each dimension in Y should be ordered according to its variance.

Mathematically, the orthonormal basis P are used to transform X into the matrix Y such that the covariance matrix  $C_Y$  will be a diagonal matrix. Thus, the relationship between the covariance  $C_Y$  and P is given by:

$$\begin{aligned} C_Y &= \frac{1}{n}YY^T \\ &= \frac{1}{n}(PX)(PX)^T \\ &= \frac{1}{n}PXX^TP^T = \frac{1}{n}PC_XP^T \end{aligned} \quad (\text{A.0.3})$$

According to linear algebra,  $C_X$  is a symmetric matrix and can be diagonalized by an orthogonal matrix of its eigenvectors (for details please see reference [97]):

$$C_X = EDE^T \quad (\text{A.0.4})$$

Hereby D is a diagonal matrix containing the eigenvalues of the data and E is a matrix of eigenvectors of  $C_X$  arranged in columns<sup>1</sup>.

Therefore, the transformation matrix P is selected such that each row is an eigenvector of  $C_X$ . In that case P will be equal to  $E^T$  and  $P^T = P^{-1}$ . Rewriting equation A.0.3 leads to:

$$\begin{aligned} C_Y &= \frac{1}{n}PC_XP^T \\ &= P(EDE^T)P^T \\ &= P(P^TDP)P^T \\ &= (PP^{-1})D(PP^{-1}) \\ &\Rightarrow C_Y = D \end{aligned} \quad (\text{A.0.5})$$

This particular choice of P diagonalizes the covariance matrix  $C_Y$  and the transformed data set Y exhibits the desired characteristics.

### A.0.1. PCA using Singular Value Decomposition (SVD)

A PCA can also be performed using singular value decomposition (SVD). The SVD method is a more general approach finding the new basis [97].

<sup>1</sup>The matrix  $C_X$  may have  $r \leq m$  orthonormal eigenvectors where r is the rank of the matrix. When the rank of  $C_Y$  is less than  $m$ , the  $r - m$  additional vectors do not affect the final solution because the variances associated with these directions are zero.

The decomposition of matrix  $X$  using SVD is given by:

$$X = U\Sigma V^T$$

Hereby,  $\Sigma$  is a diagonal matrix containing the singular values of  $X$ ,  $U$  and  $V$  are the left and right eigenvectors of matrix  $X$ . Now rewriting the last equation, we have:

$$X = U\Sigma V^T$$

$$U^T X = \Sigma V^T$$

Defining  $Y \equiv \Sigma V^T$ , it is clear that the orthogonal basis  $U^T$  correspond to  $P$  which transforms the matrix  $X$  into  $Y$ . The eigenvectors with the largest eigenvalues contain the bulk of information necessary to characterized the original data.

In order to reduce the dimensionality of a data set, the components in matrix  $U$  associated with the smallest eigenvalues can be set to zero. This leads to a matrix  $\tilde{U}$  containing only the dynamics of interest. To conclude, the transformed data in terms of the SVD decomposition of the matrix  $X$  can therefore be written as:

$$Y = \tilde{U}^T X = \tilde{U}^T U \Sigma V^T$$

where the term  $\tilde{U}^T U$  is a simple  $n \times m$  matrix which has ones on the diagonal and zeros everywhere else.



# Bibliography

- [1] Barry MH. Magnetic Resonance Imaging Needs Assessment. Department of Health of Scotia; 2004.
- [2] Rofsky NM, Lee VS, Laub G, Pollack MA, Krinsky GA, Thomasson D, et al. Abdominal MR imaging with a volumetric interpolated breath-hold examination. *Radiology*. 1999;212(3):876–84.
- [3] Wilson SJ, Brereton IM, Hockings P, Roffmann W, Doddrell DM. Respiratory triggered imaging with an optical displacement sensor. *Magnetic Resonance in Medicine*. 1993;11(7):1027–32.
- [4] Ehman EL, Felmlee JP. Flow artifact reduction in MRI: a review of the roles of gradient moment nulling and spatial presaturation. *Magnetic Resonance in Medicine*. 1990;14(2):293–307.
- [5] Sodickson DK, Manning WJ. Simultaneous acquisition of spatial harmonics (SMASH): ultra-fast imaging with RF coil arrays. *Magnetic Resonance in Medicine*. 1997;38(4):591–603.
- [6] Jakob PM, Griswold MA, Edelman RR, Sodickson DK. AUTO-SMASH: a self-calibrating technique for SMASH imaging. *SiMultaneous Acquisition of Spatial Harmonics*. *MAGMA*. 1998;7(1):42–54.
- [7] Pruessmann KP, Weiger M, Scheidegger MB, Boesiger P. SENSE: sensitivity encoding for fast MRI. *Magnetic Resonance in Medicine*. 1999;42(5):952–962.
- [8] Kyriakos WE, Panych LP, Kacher DF, Westin CF, Bao SM, Mulkern RV, et al. Sensitivity profiles from an array of coils for encoding and reconstruction in parallel (SPACE RIP). *Magnetic Resonance in Medicine*. 2000;44(2):301–308.
- [9] Griswold MA, Jakob PM, Nittka M, Goldfarb JW, Haase A. Partially parallel imaging with localized sensitivities (PILS). *Magnetic Resonance in Medicine*. 2000;44(4):602–609.
- [10] Heidemann RM, Griswold MA, Haase A, Jakob PM. VD-AUTO-SMASH imaging. *Magnetic Resonance in Medicine*. 2001;45(6):1066–1074.
- [11] Griswold MA, Jakob PM, Heidemann RM, Nittka M, Jellus V, Wang J, et al. Generalized autocalibrating partially parallel acquisitions (GRAPPA). *Magnetic Resonance in Medicine*. 2002;47(6):1202–1210.
- [12] Madore B, Glover GH, Pelc NJ. Unaliasing by fourier-encoding the overlaps using the temporal dimension (UNFOLD), applied to cardiac imaging and fMRI. *Magnetic Resonance in Medicine*. 1999;42(5):813–828.

- 
- [13] Kellman P, Epstein FH, McVeigh ER. Adaptive sensitivity encoding incorporating temporal filtering (TSENSE). *Magnetic Resonance in Medicine*. 2001;45(5):846–852.
- [14] Breuer FA, Kellman P, Griswold MA, Jakob PM. Dynamic autocalibrated parallel imaging using temporal GRAPPA (TGRAPPA). *Magnetic Resonance in Medicine*. 2005;53(4):981–985.
- [15] Tsao J, Boesiger P, Pruessmann KP. k-t BLAST and k-t SENSE: dynamic MRI with high frame rate exploiting spatiotemporal correlations. *Magnetic Resonance in Medicine*. 2003;50(5):1031–1042.
- [16] Pedersen H, Kozerke S, Ringgaard S, Nehrke K, Kim WY. k-t PCA: temporally constrained k-t BLAST reconstruction using principal component analysis. *Magnetic Resonance in Medicine*. 2009;62:706–716.
- [17] Tsao J, Pruessmann K, Boesiger P. Feedback Regularization for SENSE reconstruction. *Proceedings International Society Magnetic Resonance in Medicine*. 2002;10:739.
- [18] Levitt MH. *Spin Dynamics: Basics of Nuclear Magnetic Resonance*. Sons JW, editor. Wiley; 2002.
- [19] Higgins D. <http://www.revisemri.com>; 2007.
- [20] Larmor J. A Dynamical Theory of the Electric and Luminiferous Medium. Part III. Relations with Material Media. *Philosophical Transactions of the Royal Society A: Mathematical, Physical and Engineering Sciences*. 1897;190:205.
- [21] Haacke EM, Brown RW, Thompson MR, R V. *Magnetic Resonance Imaging, Physical Principles and Sequence Design*. John Wiley and Sons; 1999.
- [22] Bernstein MA, King KF, Zhou XJ. *Handbook of MRI Pulse Sequences*. Bernstein MA, editor. Elsevier; 2004.
- [23] Edelstein WA, Hutchison JM, Johnson G, Redpath T. Spin warp NMR imaging and applications to human whole-body imaging. *Physics Medicine Biology*. 1980;25(4):751–756.
- [24] Haase A, Frahm J, Matthaei D, Hanicke W, Merboldt KD. Flash imaging- rapid NMR imaging using low flip angle pulses. *Journal Magnetic Resonance*. 1986;67(2):258–266.
- [25] Luterbur PD. Image formation by induced local interactions: Examples employing nuclear magnetic resonance. *Nature*. 1973;242:190–191.
- [26] Dutt A, Rokhlin V. Fast Fourier transforms for nonequispaced data. *SIAM J Sci Comput*. 1993;14:1368–1383.
- [27] Uecker M, Zhang S, Voit D, Karaus A, Merboldt KD, Frahm J. Real-time MRI at a resolution of 20 ms. *NMR in Biomedicine*. 2010;23:986–994.
- [28] Mansfield P. Multi-planar image-formation using NMR spin echoes. *Journal of Physics C-Solid State Physics*. 1977;10(3):L55–L58.
- [29] Hennig J, Nauerth A, Friedburg H. RARE imaging: a fast imaging method for clinical MR. *Magnetic Resonance in Medicine*. 1986;3(6):823–833.

- 
- [30] Hyde JS, Jesmanowicz A, Froncisz W, Kneeland JC, Grist TM. Parallel image acquisition from noninteracting local coils. *Journal Magnetic Resonance*. 1986;70:512–517.
- [31] Roemer PB, Edelstein WA, Hayes CE, Souza SP, Mueller OM. The NMR phased array. *Magnetic Resonance in Medicine*. 1990;16:192–225.
- [32] Carlson JW. An algorithm for NMR imaging reconstruction based on multiple RF receiver coils. *Journal Magnetic Resonance*. 1987;74:376–380.
- [33] Hutchinson MU, Raff U. Fast MRI data acquisition using multiple detectors. *Magnetic Resonance in Medicine*. 1988;6:87–91.
- [34] Hardy CJ, Giaquinto RO, Piel JE, Rohling KW, Marinelli L, Fiveland EW, et al. 128-channel body MRI with a flexible high-density receiver-coil array. *Magnetic Resonance Imaging*. 2008;28(5):1219–1225.
- [35] Potthast A, Kalnischkies B, Kwapil G, Wald LL, Heumann T, Helmecke S, et al. A MRI system with 128 seamlessly integrated receive channels. *Proceedings of the 15th Annual Meeting of ISMRM*. 2007;p. 246.
- [36] Kelton J, Magin RM, Wright SM. An algorithm for rapid image acquisition using multiple receiver coils. *Proceedings of the 8th Meeting at International Society Magnetic Resonance in Medicine*. 1989;Abstract 1172.
- [37] Ra JB, Rim CY. Fast imaging using subencoding data sets from multiple detectors. *Magnetic Resonance in Medicine*. 1993;30(1):142–145.
- [38] Blaimer M, Breuer F, Mueller M, Heidemann RM, Griswold MA, Jakob PM. SMASH, SENSE, PILS, GRAPPA: how to choose the optimal method. *Top Magnetic Resonance Imaging*. 2004;15(4):223–236.
- [39] Breuer FA, Kannengiesser SAR, Blaimer M, Seiberlich N, Jakob PM, Griswold MA. General formulation for quantitative G-factor calculation in GRAPPA reconstructions. *Magnetic Resonance in Medicine*. 2009;62(3):739–746.
- [40] Seiberlich N, Breuer FA, Ehse P, Moriguchi H, Blaimer M, Jakob PM, et al. Using the GRAPPA operator and the generalized sampling theorem to reconstruct under-sampled non-Cartesian data. *Magnetic Resonance in Medicine*. 2009;61(3):705–715.
- [41] Seiberlich N, Ehse P, Duerk J, Gilkeson R, Griswold M. Improved radial GRAPPA calibration for real-time free-breathing cardiac imaging. *Magnetic Resonance in Medicine*. 2011;65(2):492–505.
- [42] Seiberlich N, Wright KL, Ehse P, Griswold MA. Through-time 3D radial GRAPPA for whole heart cardiac imaging. *Journal of Cardiovascular Magnetic Resonance*. 2012;14(1):P279.
- [43] Lawson CL, Hanson RJ. Solving least squares problems. Cliff E, editor. Prentice-Hall; 1977.
- [44] Larkman DJ, Batchelor PG, Atkinson D, Rueckert D, Hajnal JV. Beyond the g-factor limit in sensitivity encoding using joint histogram entropy. *Magnetic Resonance in Medicine*. 2006;55:153–160.

- 
- [45] Phillips DL. A technique for the numerical solution of certain integral equations of the first kind. *Assoc Comput Mach.* 1962;9:84–97.
- [46] Tikhonov AN. Solution of incorrectly formulated problems and the regularization method. *Dokl Akad Nauk SSSR.* 1963;151:501–504.
- [47] Hansen PC. Analysis of discrete ill-posed problems by means of the L-curve. *SIAM Review.* 1992;34:561–580.
- [48] Hansen PC. A Matlab Package for Analysis and Solution of Discrete Ill-Posed Problems. *Numerical Algorithms.* 2007;46:187–194.
- [49] Morozov VA. *Methods for Solving Incorrectly Posed Problems.* Springer Verlag; 1984.
- [50] Hansen PC, O’Leary DP. The use of the L-curve in the regularization of discrete ill-posed problems. *SIAM J Sci Comput.* 1993;14:1487–1503.
- [51] Vogel CR. Optimal choice of a truncation level for the truncated SVD solution of linear first kind integral equations when data are noisy. *SIAM J Sci Comput.* 1986;23:109–117.
- [52] Thunberg P, Zetterberg P. Noise distribution in SENSE- and GRAPPA-reconstructed images: a computer simulation study. *Magnetic Resonance Imaging.* 2007;25:1089–1094.
- [53] Atkinson DJ, Edelman RR. Cineangiography of the heart in a single breath hold with a segmented turboflash sequence. *Radiology.* 1991;17(52):357–360.
- [54] Huang F, Akao J, Vijayakumar S, Duensing GR, Limkeman M. k-t GRAPPA: a k-space implementation for dynamic MRI with high reduction factor. *Magnetic Resonance in Medicine.* 2005;54:1172–1182.
- [55] Jung B, Ullmann P, Honal M, Bauer S, Hennig J, Markl M. Parallel MRI with extended and averaged GRAPPA kernels (PEAK-GRAPPA): Optimized spatiotemporal dynamic imaging. *Magnetic Resonance in Medicine.* 2008;28:1226–1232.
- [56] Xiang Q, Henkelman RM. K-Space Description for MR Imaging of Dynamic Objects. *Magnetic Resonance Imaging.* 2005;29:422–428.
- [57] Koestler H, Sandstede J, Lipke C, Landschutz W, Beer M, Hahn D. Auto-SENSE perfusion imaging of the whole human heart. *Magnetic Resonance in Medicine.* 2003;18:702–708.
- [58] Kozerke S, Plein S. High-resolution MR perfusion imaging with k-t BLAST and k-t SENSE. *Medicamundi.* 2008;52:64–67.
- [59] Madore B. Using UNFOLD to Remove Artifacts in Parallel Imaging and in Partial-Fourier Imaging. *Magnetic Resonance in Medicine.* 2002;48:493–501.
- [60] Blaimer M, Ponce IP, Breuer FA, Jakob PM, Griswold MA, Kellman P. Temporal Filtering Effects in Dynamic Parallel MRI. *Magnetic Resonance in Medicine.* 2011;67:1–7.
- [61] Malik SJ, Schmitz S, O’Regan D, Larkman DJ, Hajnal JV. x-f Choice: Reconstruction of Undersampled Dynamic MRI by Data-Driven Alias Rejection Applied to

- ContrastEnhanced Angiography. *Magnetic Resonance in Medicine*. 2006;56:811–823.
- [62] Hansen MS, Atkinson D, Sorensen TS. Cartesian SENSE and k-t SENSE Reconstruction Using Commodity Graphics Hardware. *Magnetic Resonance in Medicine*. 2008;59:463–469.
- [63] Xu D, King KF, Liang ZP. Improving k-t SENSE by Adaptive Regularization. *Magnetic Resonance in Medicine*. 2007;57:918–930.
- [64] Tzu-Cheng C, Chung HW, Hoge WS, Madore B. A 2D MTF Approach to Evaluate and Guide Dynamic Imaging Developments. *Magnetic Resonance in Medicine*. 2010;63:407–418.
- [65] Scheffler K, Hennig J. Reduced circular Field-of-View Imaging. *Magnetic Resonance in Medicine*. 1998;40:474–480.
- [66] Rasche V, De Boer R, Holz D, Proksa R. Continuous Radial Data Acquisition for Dynamic MRI. *Magnetic Resonance in Medicine*. 1995;34:754–761.
- [67] Hansen MS, Baltus C, Tsao J, Kozerke S, Pruessmann KP, Eggers H. k-t BLAST Reconstruction From Non-Cartesian k-t Space Sampling. *Magnetic Resonance in Medicine*. 2006;55:85–91.
- [68] Axelsson O. Iterative solution methods. Cambridge University Press. 1996;p. 654.
- [69] Pruessmann K, Weiger M, Bornert P, Boesiger P. Advances in sensitivity encoding with arbitrary k-space trajectories. *Magnetic Resonance in Medicine*. 2001;46(4):638–651.
- [70] Ponce Garcia IP, Blaimer M, Breuer F, Jakob P, Griswold M, Kellman P. Temporal Filtering Effects in Dynamic Parallel MRI: Comparing Radial and Cartesian Sampling. Proc of the 19th Annual Meeting of ISMRM. 2011;p. 4405.
- [71] Kozerke S, Tsao J, Razavi R, Boesiger P. Accelerating cardiac cine 3D imaging using k-t BLAST. *Magnetic Resonance in Medicine*. 2004;52:19–26.
- [72] Hansen MS, Kozerke S, Pruessmann KP, Boesiger P, Pedersen EM, Tsao J. On the Influence of training Data Quality in k-t BLAST Reconstruction. *Magnetic Resonance in Medicine*. 2004;52:1175–1183.
- [73] Vitanis V, Boesiger P, Kozerke S. Highly accelerated k-t SENSE with improved temporal fidelity. Proc Euro Soc Magn Reson Med and Bio (ESMRMB) 14th. 2006;p. 142.
- [74] Vitanis V, Manka R, Boesiger P, Kozerke S. Accelerated Cardiac Perfusion Imaging Using k-t SENSE with SENSE Training. *Magnetic Resonance in Medicine*. 2009;62:955–965.
- [75] Ponce Garcia I, Blaimer M, Breuer F, Griswold M, Jakob P, Kellman P. Auto-calibration approach for k-t SENSE. *Magnetic Resonance in Medicine*. DOI: 101002/mrm24738;.
- [76] Ponce Garcia I, Blaimer M, Breuer F, Jakob P, Griswold M, Kellman P. Auto-calibration method for k-t-SENSE: Using TGRAPPA to calculate the training data. *Magnetic Resonance in Medicine*. 2009;p. 2828.

- [77] Tofts P. Quantitative MRI of the brain: measuring change caused by disease. Chichester, editor. Wiley; 2003.
- [78] Zipp F. A new window in multiple sclerosis pathology: non-conventional quantitative magnetic resonance imaging outcomes. *Neurol Sci.* 2009;1:24–29.
- [79] Odrobina EE, Lam TY, Pun T, Midha R, Stanisz GJ. MR properties of excised neural tissue following experimentally induced demyelination. *NMR Biomed.* 2005;18:277–284.
- [80] Deoni SCL. High-resolution T1 mapping of the brain at 3T with driven equilibrium single pulse observation of T1 with high-speed incorporation of RF field inhomogeneities (DESPOT1-HIFI). *Magnetic Resonance in Medicine.* 2007;26:1106–1111.
- [81] Zhu DC, Penn RD. Full brain T1 mapping through inversion-recovery fast spin echo imaging with time-efficient slice ordering. *Magnetic Resonance in Medicine.* 2005;54:725–731.
- [82] Deichmann R. Fast high-resolution T1 mapping of the human brain. *Magnetic Resonance in Medicine.* 2005;54:20–27.
- [83] Gulani V, Schmitt P, Griswold MA, Webb AG, Jakob PM. Towards a single-sequence neurologic magnetic resonance imaging examination: multiple-contrast images from an IR TrueFISP experiment. *Invest Radiol.* 2004;39:767–774.
- [84] Deoni SCL, Rutt BK, Peters TM. High-resolution T1 and T2 mapping of the brain in a clinically acceptable time with DESPOT1 and DESPOT2. *Magnetic Resonance in Medicine.* 2005;53:237–241.
- [85] Schmitt P, Griswold MA, Jakob PM, Kotas M, Gulani V, Flentje M, et al. Inversion recovery TrueFISP: quantification of T1, T2 and spin density. *Magnetic Resonance in Medicine.* 2004;51:661–667.
- [86] Petzschner FH, Ponce Garcia IP, Blaimer M, Jakob PM, Breuer FA. Fast MR Parameter Mapping Using k-t Principal Component Analysis. *Magnetic Resonance in Medicine.* 2011;66:706–716.
- [87] Deimling M, Heid O. Magnetization prepared true fisp imaging. *Proceedings International Society Magnetic Resonance in Medicine.* 1994;p. 495.
- [88] Deichmann R, Hahn D, Haase A. Quantification of T1 by SNAPSHOT FLASH NMR imaging. *Magnetic Resonance in Medicine.* 1992;96:608–612.
- [89] Oppelt A, Graumann R, Barfuss H, Fischer H, Hartl W, Schajor W. FISP a new fast MRI sequence. *Electromedica.* 1986;54:15–18.
- [90] Collins DL, Zijdenbos A, Kollokian V, Sled J, Kabani N, Holmes C, et al. Design and Construction of a Realistic Digital Brain Phantom. *IEEE Transactions on Medical Imaging.* 1998;17:463–468.
- [91] Collins D. <http://www.bic.mni.mcgill.ca/brainweb/>; 2009.
- [92] Hargreaves B. <http://www-mrsrl.stanford.edu/brian/bloch/>; 2002.
- [93] Pedersen H, Kelle S, Ringgaard S, Schnackenburg B, Nagel E, Nehrke K, et al. Quantification of Myocardial Perfusion Using Free-Breathing MRI and Prospective Slice Tracking. *Magnetic Resonance in Medicine.* 2009;61:734–738.

- [94] Petzschner F. Schnelle T1, T2 und Spindichte Quantifizierung in der MRT mit der Principle Component Analyse. Universitaet Wuerzburg; 2009.
- [95] Pearson K. On Lines and Planes of Closest Fit to Systems of Points in Space. Philosophical Magazine 2. 1901;11:559–572.
- [96] Jolliffe I. Principal Component Analysis. Springer Verlag; 1986.
- [97] Shlens J. A Tutorial on Principal Component Analysis. [www.sn1.salk.edu/shlens/](http://www.sn1.salk.edu/shlens/); 2005.





# List of Publications

## Papers

**Ponce IP**, Blaimer M, Breuer FA, Griswold MA, Jakob PM, Kellman P.

*Auto-calibration approach for k-t SENSE.*

Magnetic Resonance in Medicine. 2013; doi:10.1002/mrm.24738.

Petzschner FH, **Ponce IP**, Blaimer M, Jakob PM, Breuer FA.

*Fast MR Parameter Mapping Using k-t Principal Component Analysis.*

Magnetic Resonance in Medicine. 2011;66:706-716.

Blaimer M, **Ponce IP**, Breuer FA, Jakob PM, Griswold MA, Kellman P.

*Temporal Filtering Effects in Dynamic Parallel MRI.*

Magnetic Resonance in Medicine. 2011;67:1-7.

## Proceedings

**Ponce PI**, Blaimer M, Breuer FA, Jakob PM, Griswold MA, and Kellman P.

*Auto-calibration method for k-t SENSE: Using TGRAPPA to calculate the training data.*

Proceedings of the 17th Annual Meeting of ISMRM. 2009; p. 2828.

**Ponce PI**, Lopez MA, Blaimer M, Breuer FA, Jakob PM, Griswold MA, and Kellman P.

*Auto-Calibrated k-t SENSE for Coil Limited Reconstructions on a 7 Tesla Small Animal Scanner.*

Proceedings of the DSISMRM. 2009.

Petzschner FH, **Ponce IP**, Blaimer M, Jakob PM, Breuer FA.

*Fast T1, T2 & spin density mapping using k-t PCA.*

Proceedings of the 26th Annual Meeting of ESMRMB. 2009.

**Ponce PI**, Blaimer M, Breuer FA, Jakob PM, Griswold MA, and Kellman P.

*On Temporal Filtering Effects caused by the subtraction of temporal average in Dynamic Parallel MRI.*

Proceedings of the 18th Annual Meeting of ISMRM. 2010; p. C29.

Petzschner FH, **Ponce IP**, Blaimer M, Jakob PM, Breuer FA.  
*Fast MR Parameter Mapping using k-t PCA.*  
Proceedings of the 18th Annual Meeting of ISMRM. 2010; 544.

**Ponce PI**, Blaimer M, Breuer FA, Jakob PM, Griswold MA, and Kellman P.  
*Temporal Filtering Effects in Dynamic Parallel MRI: Comparing Radial and Cartesian Sampling.*  
Proceedings of the 19th Annual Meeting of ISMRM. 2011; p. 4405.

**Ponce PI**, Blaimer M, Breuer FA, Jakob PM, Griswold MA, and Kellman P.  
*Comparing k-t SENSE and Auto-Calibrating k-t SENSE Transfer Functions.*  
Proceedings of the 20th Annual Meeting of ISMRM. 2012; p. 4250.



# Acknowledgment

I would like to express my gratitude to ...

... Prof. Dr. Peter M. Jakob who gave me the opportunity to be a part of Experimentelle Physik 5 (EP5) and for all his help and support.

... Dr. Martin Blaimer and Dr. Felix Breuer who have been my mentors and guides during all the years of research. They have proposed pioneering ideas and were, with great patience, always willing to help.

Special thanks go to Peter Kellman for the contribution of valuable ideas and feedback.

I would like also to thank...

... DAAD-CONACyt for the support and making this experience in Germany possible.

... all of EP5 and especially the GK-Team for the good atmosphere and scientific discussions.

... Sabine Voll (chica hermana) who took care of me like her own sister and had the right answers to make the life happier.

... Yuxiang Ye and Marta Michalska for your understanding and sharing this journey with me.

.... my office (Thomas Benkert and Martinote + Melisita) and my ex-office (Simon Thiphan, Ebi Munz, Volker Sturm, Anna Vilter and Martinote) for providing an entertaining (and at times noisy) environment to keep me alive.

... a mi familia que me ha apoyado y enseñado a sonreír y levantarme en los peores momentos. A Coni y a Matías que admiro por su paciencia y perseverancia. A Mayis y Donald que son parte de este documento y también de mi vida.

... my husband Daniel Neumann for his support in good and difficult times.



# Abstract

In Magnetic Resonance Imaging (MRI), acquisition of dynamic data may be highly complex due to rapid changes occurred in the object to be imaged. For clinical diagnostic, dynamic MR images require both high spatial and temporal resolution. The speed in the acquisition is a crucial factor to capture optimally dynamics of the objects to obtain accurate diagnosis. Technological advances in the last decades have allowed in certain degree acceleration in the MRI process. With the application of faster hardware, rapid sequences, increasing number of coil receiver, acquisition strategies among others, the reduction of scan times has been possible. In the 90's, partially parallel MRI (pMRI) has been introduced to shorten scan times reducing the amount of acquired data. These approaches use multi-receiver coil arrays to acquire independently and simultaneously the data.

Reduction in the amount of acquired data results in images with aliasing artifacts. Many strategies have been implemented to obtain artifact-free images utilizing spatial information provided by the receiver coils and/or information about the dynamics of the data. Dedicated methods as such Sensitivity Encoding (SENSE) and Generalized Autocalibrating Partially Parallel Acquisition (GRAPPA) were the basis of a series of algorithms in pMRI. Both, the SENSE and the GRAPPA algorithms are part of clinical routines in MR devices.

Nevertheless, pMRI methods require extra spatial or temporal information in order to optimally reconstruct the data. This information is typically obtained by an extra scan or embedded in the accelerated acquisition applying a variable density acquisition scheme. Nowadays, imaging reconstruction techniques face the challenge of producing images with higher spatial and temporal resolution without compromising the acquisition time. In this work, we were able to reduce or totally eliminate the acquisition of the training data for kt-SENSE and kt-PCA algorithms obtaining accurate reconstructions with high temporal fidelity.

For dynamic data acquired in an interleaved fashion, the temporal average of accelerated data can generate an artifact-free image used to estimate the coil sensitivity maps avoiding the need of extra acquisitions. However, this temporal average contains errors from aliased components, which may lead to signal nulls along the spectra of reconstructions when methods like kt-SENSE are applied. The use of a GRAPPA filter applied to

the temporal average reduces these errors and subsequently may reduce the null components in the reconstructed data. In this thesis the effect of using temporal averages from radial data was investigated. Non-periodic artifacts performed by undersampling radial data allow a more accurate estimation of the true temporal average and thereby avoiding undesirable temporal filtering in the reconstructed images.

kt-SENSE exploits not only spatial coil sensitivity variations but also makes use of spatio-temporal correlations in order to separate the aliased signals. Spatio-temporal correlations in kt-SENSE are learnt using a training data set, which consists of several central k-space lines acquired in a separate scan. The scan of these extra lines result in longer acquisition times even for low resolution images. It was demonstrated that limited spatial resolution of training data set may lead to temporal filtering effects (or temporal blurring) in the reconstructed data.

In this thesis, the auto-calibration for kt-SENSE was proposed and its feasibility was tested in order to completely eliminate the acquisition of training data. The application of a prior TSENSE reconstruction produces the training data set for the kt-SENSE algorithm. These training data have full spatial resolution. Furthermore, it was demonstrated that the proposed auto-calibrating method reduces significantly temporal filtering in the reconstructed images compared to conventional kt-SENSE reconstructions employing low resolution training images. However, the performance of auto-calibrating kt-SENSE is affected by the Signal-to-Noise Ratio (SNR) of the first pass reconstructions that propagates to the final reconstructions.

Another dedicated method used in dynamic MRI applications is kt-PCA, that was first proposed for the reconstruction of MR cardiac data. In this thesis, kt-PCA was employed for the generation of spatially resolved  $M_0$ ,  $T_1$  and  $T_2$  maps from a single accelerated IR-TrueFISP or IR-Snapshot FLASH measurement. In contrast to cardiac dynamic data, MR relaxometry experiments exhibit signal at all temporal frequencies, which makes their reconstruction more challenging. However, since relaxometry measurements can be represented by only few parameters, the use of few principal components (PC) in the kt-PCA algorithm can significantly simplify the reconstruction. Furthermore, it was found that due to high redundancy in relaxometry data, PCA can efficiently extract the required information from just a single line of training data.

It has been demonstrated in this thesis that auto-calibrating kt-SENSE is able to obtain high temporal fidelity dynamic cardiac reconstructions from moderate accelerated data avoiding the extra acquisition of training data. Additionally, kt-PCA has been proved to be a suitable method for the reconstruction of highly accelerated MR relaxometry data. Furthermore, a single central training line is necessary to obtain accurate reconstructions. Both reconstruction methods are promising for the optimization of training data acquisition and seem to be feasible for several clinical applications.





# Zusammenfassung

Dynamische Bildgebung mithilfe der Magnetresonanztomographie stellt eine besondere Herausforderung dar. Für klinische Anwendungen benötigt man Bilder mit hoher räumlicher und bei schnellen Bewegungen auch zeitlicher Auflösung. Aus diesem Grund ist die Geschwindigkeit der Datenakquisition ein entscheidender Faktor, um genaue Diagnosen zu erhalten. Technologische Fortschritte in den letzten Jahrzehnten, in speziellen Entwicklungen von Hardware, Sequenzen und Akquisitionsschemata, konnten MRT-Experimente erheblich beschleunigen.

Einen weiteren wichtigen Beitrag lieferte die parallele Bildgebung (pMRT), die in den 90er Jahren eingeführt wurde und durch die Entwicklung von Spulenarrays für den Empfang des MR-Signals ermöglicht wurde. In paralleler Bildgebung wird nur ein Teil der eigentlich benötigten Daten aufgenommen. Diese Unterabtastung des k-Raum führt zu Bildern mit Aliasing-Artefakten. Verschiedenste Algorithmen wurden entwickelt, um mittels der zusätzlichen räumlichen Informationen der Spulenarrays anschließend artefaktfreie Bilder zu rekonstruieren. Heute spielen im Speziellen Sensitivity Encoding (SENSE) und Generalized Autocalibrating Partially Parallel Acquisition (GRAPPA) eine große Rolle im klinischen Alltag und bilden eine Grundlage für eine Vielzahl anderer Algorithmen.

Ein Großteil aller pMRT Methoden erfordern für optimale Ergebnisse zusätzliche räumliche oder zeitliche Informationen zur Kalibrierung. Diese Kalibrations- oder Trainingsdaten werden in der Regel durch einen zusätzlichen Scan erzeugt oder in die beschleunigte Messung eingebettet aufgenommen. In beiden Fällen ist eine unerwünschte Verlängerung der Messzeit die Folge.

Heute stehen Bildrekonstruktionsverfahren deshalb vor der Herausforderung, Bilder mit höherer räumlicher und zeitlicher Auflösung zu ermöglichen ohne jedoch die Aufnahmezeit zu verlängern. In dieser Arbeit konnten wir kt-SENSE und kt-PCA Rekonstruktionen dynamischer MRT Daten mit hoher zeitlicher Genauigkeit erzielen bei gleichzeitiger Reduktion bzw. sogar Beseitigung der benötigten Menge an Trainingsdaten.

Um die in beiden Methoden benötigten Spulensensitivitäten zu berechnen, kann bei bestimmten Abtastschemata mit dem Mittelwert der dynamischen Daten ein weitgehend Artefakt-freies Bild erzeugt werden. Dieser zeitliche Mittelwert enthält jedoch kleine Fehler, die durch die Anwendung von Methoden wie kt-SENSE zu Signalauslöschungen im Spektrum der rekonstruierten Daten führen können. Es konnte gezeigt werden, dass die Anwendung eines GRAPPA Filter auf den zeitlichen Mittelwert die Fehler in den Spulensensitivitäten reduziert und die Rekonstruktion von Daten aller Frequenzen ermöglicht. Eine weitere aufgezeigte Möglichkeit ist die Verwendung einer radialen

Akquisition, die dank der inkohärenten Aliasing-Artefakte ebenfalls zu einer erheblich genaueren Abschätzung des zeitlichen Mittelwerts führt. Dies verhindert zeitliche Ungenauigkeiten in den rekonstruierten Bildern.

Zusätzliche zu Spulensensitivitäten verwenden Rekonstruktionsmethoden wie kt-SENSE Vorkenntnisse über räumlich-zeitliche Korrelationen, um Artefakte zu entfernen. Informationen darüber werden gewöhnlich aus voll aufgenommenen Trainingsdaten mit geringer Auflösung extrahiert. Die separate Akquisition dieser Trainingsdaten verursacht eine unerwünschte Verlängerung der Messzeit. In dieser Arbeit wurde gezeigt, dass die niedrige Auflösung der Trainingsdaten zu zeitlichen Filterungseffekten in den rekonstruierten Daten führen kann. Um dies zu verhindern und um die zusätzliche Aufnahme von Trainingsdaten zu vermeiden, wurde eine Autokalibrierung für kt-SENSE vorgeschlagen und untersucht. Hierbei werden die benötigten Trainingsdaten in einem ersten Schritt durch eine TSENSE Rekonstruktion aus den unterabgetasteten Daten selbst erzeugt. Dank der vollen Auflösung dieser Trainingsdaten kann das Auftreten eines zeitlichen Filters verhindert werden. Die Leistung der Auto-kalibration wird lediglich durch einen Einfluss des SNRs der TSENSE Trainingsdaten auf die finalen Rekonstruktionen beeinträchtigt.

Ein weiteres Verfahren für die dynamische MRT ist kt-PCA, das zunächst für die Rekonstruktion von MR-Herzdaten vorgeschlagen wurde. In dieser Arbeit wurde kt-PCA für die neurologische MR Relaxometrie verwendet. Hierbei konnten aus beschleunigten IR-TrueFISP und IR-Snapshot-FLASH Messungen genaue  $M_0$ ,  $T_1$  und  $T_2$  Karten gewonnen werden. Im Gegensatz zur Herzbildgebung weisen MR Relaxometrie Datensätze Signal auf alles zeitlichen Frequenzen auf, was ihre Rekonstruktion mit konventionellen Methoden erschwert. Andererseits können die zeitlichen Signalverläufe mit einigen wenigen Parametern dargestellt werden und die Rekonstruktion mittels kt-PCA vereinfacht sich erheblich aufgrund der geringen Anzahl benötigter Hauptkomponenten (PC). Weiter wurde gezeigt, dass aufgrund der hohen Redundanz ein Trainingsdatensatz bestehend aus einer einzigen Zeile ausreicht, um alle relevanten Informationen zu erhalten.

In dieser Thesis wurde demonstriert, dass mit dem Ansatz einer auto-kalibrierten kt-SENSE Rekonstruktion Bilder mit hoher zeitlicher Genauigkeit aus beschleunigten Datensätzen des Herzens gewonnen werden können. Dies vermeidet die gewöhnlich benötigte zusätzliche Aufnahme von Trainingsdaten. Weiterhin hat sich kt-PCA als geeignetes Verfahren zur Rekonstruktion hochbeschleunigter MR Relaxometrie Datensätze erwiesen. In diesem Fall war ein Trainingsdatensatz bestehend aus einer einzelnen Zeile ausreichend für Ergebnisse mit hoher Genauigkeit. Beide Methoden stellen eine Optimierung der Datenakquisition dar und sind vielversprechend für die klinische Anwendung.